Doctoral theses at NTNU, 2023:382

Florian Flatscher

Lithium dendrites in solid-state batteries - Where they come from and how to mitigate them

Doctoral thesis

NTNU
Norwegian University of Science and Technology
Thesis for the Degree of
Philosophiae Doctor
Faculty of Natural Sciences
Department of Materials Science and Engineering

NTNU
Norwegian University of
Science and Technology

Florian Flatscher

Lithium dendrites in solid-state batteries - Where they come from and how to mitigate them

Thesis for the Degree of Philosophiae Doctor

Trondheim, November 2023

Norwegian University of Science and Technology
Faculty of Natural Sciences
Department of Materials Science and Engineering

NTNU
Norwegian University of
Science and Technology

NTNU
Norwegian University of Science and Technology

Thesis for the Degree of Philosophiae Doctor

Faculty of Natural Sciences
Department of Materials Science and Engineering

ISBN 978-82-326-7464-0 (printed ver.)
ISBN 978-82-326-7463-3 (electronic ver.)
ISSN 1503-8181 (printed ver.)
ISSN 2703-8084 (online ver.)

Doctoral theses at NTNU, 2023:382

Printed by NTNU Grafisk senter

Preface

This dissertation has been submitted to the Norwegian University of Science and Technology (NTNU) in partial fulfillment of the requirements for the academic title Philosophiae Doctor (Ph.D.). The work is mainly based on three manuscripts, where one has been published and two are written/submitted manuscripts.

The doctoral studies were started at the Institute for Chemical Technology of Materials in the TU Graz from August 2020 to March 2021 and then continued and completed at the Functional Materials and Materials Chemistry Research Group (FACET), at the department of Materials Science and Engineering, NTNU, Trondheim, Norway. The supervision of the work was led by Professor Daniel Rettenwander from August 2020 to August 2023. The co-supervisor was Professor Ann-Mari Svensson from August 2021 to August 2023.

The project has been funded by the Christian Doppler Laboratory for Solid State Batteries.

Florian Flatscher
Trondheim, August 2023

Acknowledgments

After three years this thesis concludes what has once started in Austria and somehow found its path to Norway. Along this way I have found support and assistance and for that I would like to express my gratitude.

First and foremost I would like to thank my main supervisor Daniel Rettenwander for allowing me to tread this path, to work on solid state batteries with a wide variety of approaches. For the constant feedback, even at sometimes unexpected times and for giving me the opportunity to broaden my horizon. I would also like to thank my co-supervisor Ann-Mari for the help and feedback throughout this work.

My gratitude also goes to my colleagues for the fruitful discussion both on an off topic, which let the days pass with ease. Special thanks to my office mates Philipp and Maria for our often quite multilingual exchanges. I would also like to thank the technical staff, be it Lukas in Graz or Pei Na and Johannes in Trondheim for the swift assistance even if the problems were sometimes a tad exotic.

Last but certainly not least I would like to thank my friends and family for their support along this path and for brightening my mood whenever we talked.

The author's contribution

The following scientific works are included in this dissertation

I: V. Reisecker*, **F.Flatscher***, L. Porz, C. Fincher, J.Todt, I. Hanghofer, V. Hennige, M. Linares-Moreau, P. Falcaro , S. Ganschow, S. Wenner, Y.-M. Chiang, J. Keckes, J. Fleig and D. Rettenwander. Effect of pulse-current-based protocols on the lithium dendrite formation and evolution in all-solid-state batteries. *Nature Communications* **14** (1), 2432 (2023).

***equal contributions** Contributions: D.R., V.R., and F.F. performed the experimental work. S.G. synthesized the single crystals, Y-M. C. and C.F. performed finite element calculations. F.F. and J.T performed the CS Nano XRD measurements with help from J.K.. J.T. and J.K. analyzed the CS Nano XRD data M.L.M performed the AFM measurements with assistance from F.F and the AFM data analysis with help from P.F. D.R. supervised the work. D.R., J.F., V.R., and F.F. wrote the first draft of the manuscript with discussion and feedback from I.H and V.H. All authors contributed to the final draft.

II:

F. Flatscher, J. Todt, M. Burghammer, H.S. Soreide, L. Porz, Y. Li, S. Wenner, V. Bobal, S. Ganschow, B. Sartory, R. Brunner, C. Hatzoglou, J. Keckes, D. Rettenwander. Deflecting dendrites by introducing compressive stress in Li7La3Zr2O12 using ion implantation. *submitted*, 2023.

Contributions: F.F. and L.P performed the experimental work, S.G. synthesized the single crystals. V.B. performed the ion implantation. S.W. performed the FIB cuts, SPED measurements, and APT needle preparation. H.S.S performed the APT analysis under supervision of Y.L. with the help of C.H.. C.H performed the SRIM simulation and APT data treatment and interpretation. B.S. and R.B. performed the nanoindentation. J.T. performed the CS nano XRD measurement with help from M.B., J.K, L.P. and D.R.. D.R. supervised the work. F.F, L.P, and D.R. wrote the first draft of the manuscript. All authors contributed to the final draft.

III:

C. Yldirim*, **F. Flatscher***, S. Ganschow, L. Porz, J. Todt, J. Keckes and D. Rettenwander. Origin of dendrite branching in solid-state batteries. *Paper manuscript, to be submitted*, 2023.
***equal contributions**

Contributions: D.R conceived and designed the project with help from J.K. and L.P., F.F. performed the experimental work with help from L.P., S.G. synthesized the single crystals. C.Y. performed the DFXM measurements and data analysis. F.F., C.Y., and D.R. wrote the first draft with discussion and feedback from J.T. and J.K. All authors contributed to the final draft.

Summary

Transportation is a major contributor to global CO_2 emissions and electrifying fossil fuel based vehicles could lead to a significant reduction of those emissions. As safety is paramount for vehicles, the use of lithium metal as an anode material has been avoided, due to flammability of the electrolytes and the propensity of lithium dendrite formation. Instead graphite is used as an anode, though its capacity is 10 times lower than the one of lithium metal. Through the use of non-flammable solid electrolytes the safety issue can be remedied making the lithium metal anode viable again, but the issue of dendrite growth remains. Which is why this work focuses on investigating dendrite growth in solid electrolytes and on developing possible mitigation strategies.

In the first paper of this work the influence of a pulse charging protocol compared to a direct current charging protocol on dendrite growth in Ta doped-LLZO (LLZTO) solid electrolytes was investigated. Hot pressed polycrystalline and Czochralski grown single crystalline LLZTO were shaped to cuboids and subjected to extensive surface polishing to minimize surface defects. The surface roughness was determined via Atomic Force Microscopy (AFM). After heat treatment, to remove contamination layers, the samples were coated with a Li/Sn (30wt% Sn) alloy and cycled with increasing current density to an assumed capacity of 200 µAh/cm^2 until failure, reaching the critical current density (CCD),

where dendrites grow, with direct current charging, as well as pulse charging. For the pulse charging 1 MHz pulses with a 1:1 pulse pause ratio were used. For single crystalline LLZTO there was no improvement through the usage of pulse charging, whereas polycrystalline LLZTO showed a threefold increase in the effective CCD, which takes the longer charging duration into account. Furthermore, the growth speed decreases for polycrystalline LLZTO when pulse charging is used. Since previous, purely mechanical, mechanisms do not explain the change occuring only for polycrystalline LLZTO, as confirmed by stress relaxation simulations for this condition, showing no change between direct and pulse charging, the mechanism was extended to take the local Li activity into account. Cross sectional nano XRD measurements show a diffusion-based stress decay at the dendrite tip which supports this hypothesis.

The second paper explored the change of material properties via ion implantation and the effect on the fracture properties, especially in regard to dendrite growth. After following the same surface preparation as in Paper I, Ag ions were implanted into the top 1 µm of the surface. The impact on the material structure was investigated via scanning precession electron diffraction (SPED) and cross-sectional nano XRD, showing amorphization of the top 650 nm as well as the creation of a compressive stress zone of up to -700 MPa below the amorphized layer. The determination of the Ag location in the LLZTO was attempted via Atom Probe Tomography, APT, but the implanted Ag content was too low for detection. A qualitative Ag detection was achieved via TOF SIMS. Nanoindentation was used to mechanically induce cracks in the implanted region showing cracks growing parallel to the surface. Electrochemically induced cracks show a similar behaviour and deflect after the implanted zone. Electrochemical impedance reveals that the amorphous layer has a significantly lower ionic conductivity and therefore annealing procedures may be necessary for future work. Nevertheless, it suffices as a proof of concept that ion implantation can potentially help extending the lifetime of a battery by deflecting a growing dendrite.

The third paper investigated the state of the solid electrolyte in close proximity to a lithium dendrite via Dark Field X-Ray Microscopy, DFXM, to provide a novel understanding of the point of failure in the solid electrolyte, where the dendrite causes crack growth. It was found that dislocations are created close to the dendrite tip possibly caused by the stress of the dendrite. We hypothesise that those dislocations could pose a weakness in the material guiding the direction of the fracture and why it branches out.

List of abbreviations

AFM	Atomic force microscopy
CCD	Critical current density
DFT	Density functional theory
DFXM	Dark field X-ray Microscopy
EDX	Energy dispersive X-ray analysis
EELS	Electron energy loss spectroscopy
ESRF	European Synchrotron Radiation Facility
FIB	Focused ion beam
LLZO	Lithium Lanthanum Zirconium Oxide
LLZTO	Lithium Lanthanum Zirconium Tantalum Oxide
SEI	Solid electrolyte interphase
SEM	Scanning electron microscopy
SPED	Scanning precession electron diffraction
TEM	Transmission electron microscopy
TOF-SIMS	Time of-Flight secondary ion mass spectrometry
XRD	X-Ray Diffraction

Contents

1

Introduction

1.1 Background and motivation

The impact of climate change can already be felt in various ways. The first and most prominent indicator is the increase in natural disasters, like droughts, which can damage crops and dry out the land, increasing its flammability. This in turn makes wildfires more likely and harder to deal with, such as in the extended forest fires in Australia in 2019-2020.[1–3] There the land was rather parched when there was little precipitation for over 2 years. Bushfires then laid waste to an area of 0.24 - 0.34 million km^2, the area varying due to different reporting standards employed, causing significant damages.[4]

According to the IPCCS sixth assessment report these effects will only continue. Increased temperatures over the oceans are likely to cause an increase in evaporation from ocean water. This can boost the intensity and occurrence of storms, hurricanes and flooding events.[5] Increasing temperatures over landmasses makes droughts and heatwaves more prevalent and more intense. A recent example is the deadly heatwave in India in 2015 which claimed around 2500 human lives in just a few days.[6] The contradictory seeming prediction that droughts and floods are going to be more common is caused by the fact that while more extreme precipitation events, or floods, are likely going to increase, the total rainfall frequency is decreasing.[5] Then there are the more long term effects, which are noticeable over decades, such as the change of ground fertility in swathes of Africa and southern Europe lowering food production and making hunger crises more likely.[7] A reduction in CO_2-emissions is therefore necessary to keep the deleterious effects of the increased temperature to a minimum. One of the major contributors to CO_2 emissions is individual transport using vehicles powered by gasoline or diesel. In 2019 the transport sector emitted 8.9 Gt of CO_2 equivalent and was responsible for around 15% of total greenhouse gas emissions.[8] Figure 1.1 shows the increase in CO_2 emissions from transportation since 1990, containing a slight decrease in 2020 which can be attributed to the COVID 19 pandemic. By phasing out the combustion engine, which is already planned by the European Union to occur until 2035, and using an electric motor instead emissions of greenhouse gasses from transport could be reduced by up to 68%.[8,9]

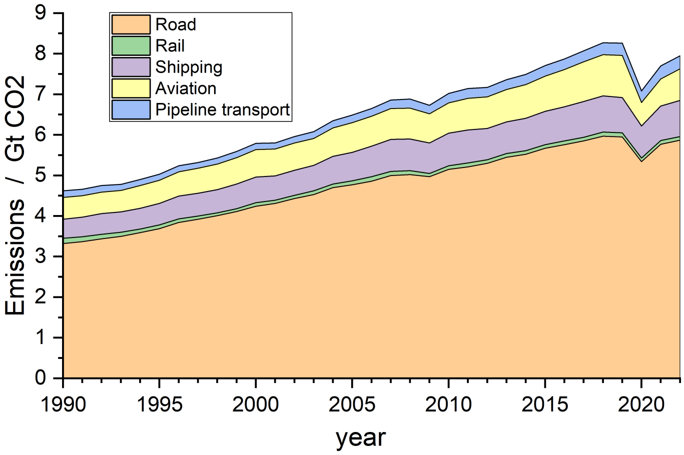

Figure 1.1: Global CO_2 emissions from transport by sub-sector from 1990 to 2022. Adapted from IEA[10]

One vital component of electric vehicles is energy storage and a large focus is placed on lithium-ion batterie systems to fulfill this need. Though lithium has a rather energy intensive and, in some regions, ethically questionable mining and production process and is not the most abundant material, with the largest sources being in Chile, Australia and China, it brings quite few performance advantages to the table.[11,12] It is the lightest and most electronegative choice possible, which translates into a very high specific energy density. For an electric vehicle this means increased range per weight. Other alternatives, which can try to compete with lithium-ion batteries in this regard are sodium and magnesium based systems, neither of which have the technological maturity that lithium ion based systems possess.[13,14]

An added benefit of vehicle electrification is that charging electric vehicles via smart meters, which allow charge of the batteries when there is a peak in energy production, e.g. from intermittent producers like solar or wind and discharge of batteries if there are peaks in the demand on the power grid, levels the demand on the grid itself.[15] Furthermore, it increases the energy storage potential available for renewable energy sources. So far large amounts of energy from renewables can only be reliably stored in hydroelectric pump storages, which cannot be built in all parts of the world. They are also, to some degree, vulnerable to weather events, such as droughts and extreme rainfall, forcing the release of water, to alleviate a drought or to keep the storage from overflowing, reducing available storage capacity.[16,17]

Energy storage in vehicles has safety concerns attached to it, regardless of the type of storage. Gasoline and natural gas are both flammable. Hydrogen is flammable, invisible, odorless and its reaction partner is readily available in the air.[18] Similarly state of the art lithium ion batteries are also flammable, due to the organic electrolyte and the reactivity with water. An additional challenge is that the most commonly used electrolyte salt, $LiPF_6$ creates hydrofluoric acid, HF, in reaction with water.[19,20] This and the fact that lithium metal, if present, can react upon contact with water, enabling it to reignite later on its own, makes it a more hazardous and complicated endeavor to completely douse the flames.[21]

When an electric vehicle crashes in a catastrophic way, that parts, which should be kept away from each other and from the outer atmosphere, like a flame from gasoline, find themselves exposed and in intimate contact it is only expected that it bursts aflame. Unexpected though is that an electric vehicle has the possibility to ignite on its own. One such case of spontaneous combustion was a Tesla in January 2023.[21,22]

A contributor to the spontaneous self ignition can be lithium filaments or dendrites growing within the battery, which is one of the main challenges in lithium battery technology. They can form during the charging of the battery, consuming part of the electrolyte when a passivating solid electrolyte interphase (SEI) grows around them, stopping further reactions. As a result capacity is lost as less lithium ions are available for storage but there is no failure of the cell.[23] The dendrite can also continue to grow, piercing the separator layer, finally causing a short circuit once it connects both electrodes.[24] The subsequent discharge of the battery, which can heat up and ignite the liquid electrolyte used in commercial cells, necessitates multiple safety features. These are voltage controls with automatic disconnects, to prevent overcharging and short circuiting. Pressure vents, also called Current Interrupt Devices, which burst open and electrically disconnect the cell if the internal pressure is too high, which can be caused by evaporating electrolyte. For larger battery packs in electric vehicles there are sensors monitoring temperature, voltage and other safety parameters which shut off electrical connections in case those parameters are exceeded.[25]

If those safety features fail, the worst case scenario can be a thermal runaway, where one cell failure propagates to the neighboring cells, heating them up causing undesired side reactions, which in turn increase the temperature creating a vicious cycle.[24] Particular noteworthy examples of a thermal runaway are the lithium ion batteries of the Samsung Galaxy Note 7 in 2016, which self ignited and exploded during charging.[26]

For the issue of the flammability of lithium ion batteries, there is a solution in sight in the form of solid electrolytes, which are reaching performance close to liquid electrolytes without being flammable. This would allow the usage of lithium metal as an anode material, which was phased out in the 90s due to safety concerns for the graphite anode, even though the capacity of graphite is 10 times lower.[27] The problem of dendritic growth on the other hand still remains unsolved and present, even for solid electrolytes, though it was hoped that they would pose a mechanical barrier for the soft growing lithium metal.[28] The purpose of this work is therefore to investigate the underlying mechanism of lithium dendrite growth in solid electrolytes and the establishment of mitigation strategies to overcome this issue.

1.2 Aim of work

The overarching objective of this work is to further our understanding of the formation of lithium growth in solid electrolytes, more specifically in the garnet $Li_{7-x}La_3Zr_{2-x}Ta_xO_{12}$, LLZTO, as a model system, and to develop possible mitigation strategies to inhibit dendrite growth. This work is split in three parts.

The first part is an investigation into the effect of different current waveforms, such as current pulses, on dendrite growth and if there is a variance in the dendrites between single crystalline and polycrystalline LLZTO. Pulsed current waveforms are already known in literature to lead to denser layer formation, be it in metal deposition or in lithium ion batteries using liquid electrolytes, extending their lifetimes substantially.[29–32] Theoretical work also predicts an inhibiting effect on dendrite growth by employing pulsed currents.[33] Therefore, the effect of pulsed currents on dendrite growth in solid electrolyte was investigated experimentally and a mechanism for the effect was established. The main results are found in Paper I.

The second part focuses on inhibiting dendrite growth by introducing residual stresses into the surface layer via ion implantation. Theoretical work has shown that a zone of compressive stress should be able to stop dendrite growth in a solid electrolyte.[34] Recent experimental work delivered a practical proof of this concept by deflecting dendrites via compressive stress introduced by mechanically bending the solid electrolyte, also using LLZTO.[35] Ion implantation has the possibility to introduce such compressive stresses and has already been shown to increase fracture resistance.[36] Though there has been a publication which investigated the effect of ion implantation on cycle life the effect on the dendrite growth behaviour was not investigated.[37] Therefore, residual stress was introduced by Ag ions implanted into LLZTO, characterized and investigated if dendrite deflection, which has been achieved by mechanically induced stress, also occurs. The findings are included in Paper II.

The third work concerns itself with the region of LLZTO surrounding a dendrite tip. The main challenge in gaining information from this region is locating and investigating it without changing the properties. One available non destructive method is Dark Field X-ray microscopy, DFXM, which is able to probe a larger region with high resolution and delivers information about the strain state of the material, the mosaicity as well as revealing dislocations.[38–40] Therefore the near tip region of a dendrite is investigated with DFXM to shed more light on the impact of the dendrite on the surrounding regions and how it can influence propagation of a dendrite. The results are summarized in Paper III.

2

Literature review

2.1 Li-ion batteries - Working principle

2.1.1 Working principle of a Li ion battery

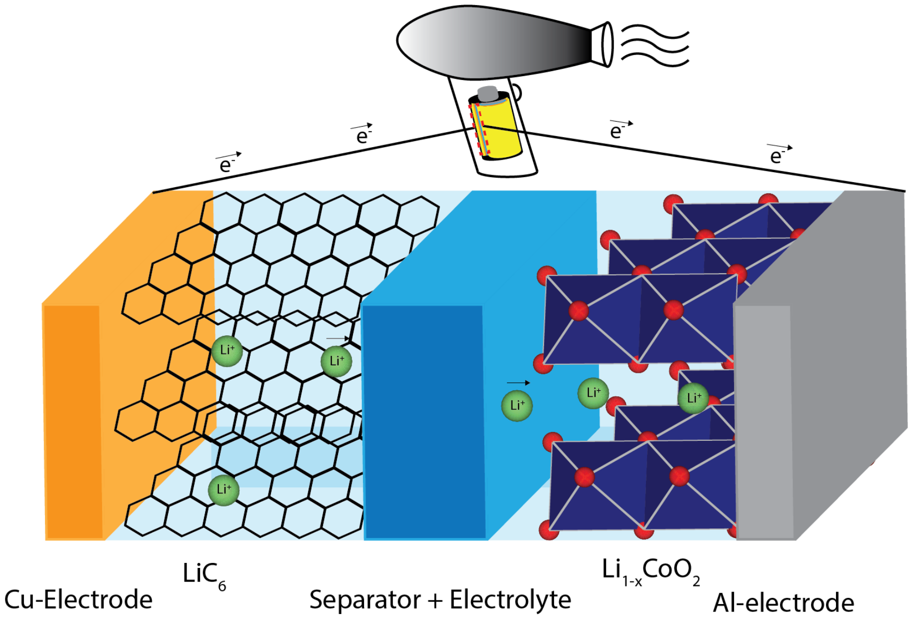

Figure 2.1: Schematic of a lithium ion battery during the discharge process

The working principle of a lithium ion-battery is shown in Figure 2.1 above. Li^+ ions move from the anode, through a separator, containing an organic electrolyte, to the cathode during discharge. At the same time electrons move via the outer connection powering the attached device. In this example the anode consists of graphite in the charged state LiC_6 and the cathode is delithiated $Li_{1-x}CoO_2$. Both of those are intercalation materials where lithium ions can be reversible moved in and out of according to the following reaction equations depicting the discharge process.[27]

$$LiC_6 \rightarrow C_6 + xLi^+ + xe^- \tag{2.1}$$

$$Li_{1-x}CoO_2 + xLi^+ + xe^- \rightarrow LiCoO_2 \tag{2.2}$$

$$Li_xC_6 + Li_{1-x}CoO_2 \rightarrow C_6 + LiCoO_2 \tag{2.3}$$

Equation 2.1 depicts the reaction at the anode side, which occurs at a potential of 0.06 V to 0.2 V, depending on the state of charge, using Li/Li^+ as a reference.[41] Equation 2.2 shows the reaction at the cathode side occurring at a potential of 3.9 V to 4.2 V, again state of charge dependent, against Li/Li^+.[42] Here x can be a value between 0, when the battery is fully charged and 1 for the fully discharged state. Equation 2.3 shows the total cell reaction which also gives the cell potential, being the difference between cathode and anode potential, of 4 V.
These potentials depend on the electrochemical potentials of the materials used. It should be noted that, depending on convention, the naming of anode and cathode can change depending on the current flow. For this work the negative electrode possessing the lower electrochemical potential will be referred to as the anode and the one possessing the higher electrochemical potential will be referred to as the cathode, regardless of the current flow. Furthermore, discharge process will refer to Li^+ ion flow from anode to cathode, whereas a charge process will indicate the reverse.

The amount of lithium that can be stored per amount of charge is referred to as the capacity, though more often the material dependent specific capacity in mAh/g is used. Here the theoretical value, of the maximum amount of lithium able to be stored, would be 372 mAh/g for the graphite anode and 274 mAh/g for $LiCoO_2$.[43–45] Since those capacities differ in practice the weight of anode and cathode are adjusted so an equal capacity is available on both sides.[46] Combining this capacity with the cell potential gives the theoretical energy storage capability of the battery, typically given in Wh/kg. The separator drenched with a organic liquid electrolyte keeps the electrodes separate, while allowing for ions to traverse. It does not contribute to the energy storage capabilities, same as other components such as current collectors and housing, while adding weight to the battery. Which is why practical energy storage values are always below the theoretical maximum.

Another factor which reduces the attainable capacity is the fact that the reactions shown in equations 2.1 to 2.3 are not the only ones that can take place in the battery. If those reactions were exclusive to what is taking place inside of a lithium-ion battery, and were perfectly reversible, energy could be stored rather indefinitely. There are multiple side reactions which can take place, either during operation or during storage which reduces cycle and calendar life. One of those is the reaction of the organic electrolyte with anode and cathode. If the electrochemical stability window, which has its upper bound at the oxidation potential and the lower bound at the reduction potential of a material does not exceed the potentials of anode or cathode, then an oxidation/reduction reaction will take place at the respective electrode. During battery operation, overpotentials needed for the electrochemical reactions to occur, can help to surpass the electrochemical window and cause reactions in a material deemed to be stable.[47]

For lithium-ion batteries this means that in the first few cycles part of the electrolyte and the mobile Li^+ ions are consumed and form a layer of degradation products on top of the anode and cathode, which is called the solid electrolyte interphase (SEI).[48] This SEI layer is passivating the surface, while still allowing the transport of lithium ions through it. As lithium and electrolyte are consumed part of the battery capacity is lost. The other dominant side reaction and a main focus of this work is the formation of lithium metal on the electrodes.[49] This is illustrated in equation 2.4.

$$xLi^+ + xe^- \rightarrow xLi \tag{2.4}$$

While it is possible for the back reaction to occur, the formed lithium can detach and be lost in the electrolyte again losing capacity.[50] More critically though the lithium metal can continue to deposit and bridge the gap between anode and cathode, leading to a short circuit. This deposition often takes the shape of dendritic structures, also called lithium dendrites.[51] In recent literature references to dendrites generally have taken to mean just the growth of lithium metal, regardless of the shape it takes on. Especially if it is rather difficult to determine said shape, such as in solids. For simplicities sake and since this work focuses on dendrites in solids, this terminology of dendrites describing any lithium filament, though somewhat inaccurate, will be used, deviating slightly from the historical and factual meaning.

2.1.2 History of Lithium-ion batteries

The earliest steps for Lithium-ion batteries were made in the late 1950s with the intent of using the low potential of lithium. A suitable solvent was required, as aqueous solvents reacted violently with lithium and were not stable at its potential. Therefore, the solubility of lithium in aprotic electrolytes was investigated and the formation of a passivation layer was found. This layer, which is now known as the solid electrolyte interphase in the battery field stops the reaction of the electrolyte with lithium, while still allowing for the transport of Li^+ across it.[27,48]

This discovery then led to the development of the 3 V primary lithium-ion batteries, using a variety of cathode materials, such as SO_2, MnO_2, while employing propylene carbonate as an electrolyte.[27]
First attempts of rechargeable lithium batteries were made in the beginning of the 1970s when a research focus was placed on cathode materials which could intercalate Li^+, instead of plating it on top. During an intercalation reaction, the Li^+ inserts into the host lattice, without changing or destroying it. Later on it can be removed electrochemically. This way the reaction could be more reversible, with appreciable capacities. The earliest commercial examples are the $Li \mid TiS_2$ battery patented by Whittingham in 1976 and commercialized in the 1980s.[52] Other chalcogenides such as MoS_2 and $NbSe_3$ were also used as cathode materials and commercialized.[27] With a move up in the periodic table from Sulfur to Oxygen a breakthrough was made in 1973, when Goodenough first reported $LiCoO_2$ as a suitable cathode material, with a potential of 3.9 V vs Li^+/Li and good electrochemical properties.[42] The development of those cathode materials resulted in the award of the Nobel prize for Goodenough and Whittingham in 2019.[53]
Though lithium metal batteries were commercialized, there were safety concerns due to the growth of lithium dendrites, combined with the flammability of the organic electrolyte, a concern which remains to a lesser degree even today. To alleviate this concern the anode was exchanged from the highly reactive lithium metal to a different candidate, which would emerge to be graphite. Though it was reported already in the 1950s that lithium could insert into graphite, the reversible electrochemical intercalation was presented in 1976.[54] At that time

the electrolyte that was used, propylene carbonate, lead to co-intercalation into the graphite matrix which delayed its usage. Using an intercalation electrode on the anode as well as on the cathode side was proposed by Armand in the early 1970s to avoid the formation of lithium metal in the cell by only transporting Li^+ back and forth, thus reducing the safety problem.[55] In 1978 Armand showed that graphite is a viable intercalation anode using a polymer electrolyte.[56] Further work by SONY and Yoshino Akira lead to the creation of the carbonaceous anode, that is widely used in lithium ion batteries today and for which Akira was honored as the third co-recipient of the Nobel Prize of 2019.[53]

2.2 Li-ion batteries - State of the art.

2.2.1 Anode materials

Looking at the state of the art of Li-ion battery technology starting from the anode side, the materials can be divided into 4 categories.

- Intercalation anodes
- Alloy formers
- Conversion type materials
- Lithium metal

Examples for intercalation-based anodes are graphite, which is the most commercially used one and the other one of interest is $Li_4Ti_5O_{12}$, LTO.[57,58] Graphite has a theoretical specific capacity of 372 mAh/g if it reaches its fully lithiated form LiC_6.[43,57] Lithium intercalates into graphite at a potential between 0 and 0.25 V vs Li^+/Li (or 3 V vs. normal hydrogen electrode NHE). Through the insertion of the Li^+ in between the graphite layers a slight volume expansion occurs due to the increased interlayer distance, which is 10% larger in the lithiated state.[59]

During the first charging in contact with aprotic electrolytes a SEI layer forms on the graphite which protects the electrolyte kinetically from further electrochemical reduction. The morphology and composition of this layer depends on the electrolyte, salt used, temperature and parameters, like current density, used during the first reduction. Typical thickness of the SEI can range from 0.02 to 1 µm, varying from the age of the electrolyte.[57] Due to the potential of graphite being relatively close to the one of metallic lithium, the formation mechanism of the SEI is similar. One issue of this similar potential though is its propensity for plating metallic lithium, especially at low temperatures and high currents where the overpotentials can shift the reaction from intercalation of lithium to formation of metallic lithium.[49]

This is a problem that LTO solves by having a much larger working potential, of around 1.55 V vs Li^+/Li, which is why it is preferred in areas where safety is paramount, such as batteries for medical devices. This comes at the cost of "only" being a 1.5 V battery and a lower specific capacity of 175 mAh/g, about half of that of graphite.[58,60] Its volume expansion is much lower than the one of graphite, with only 0.1% change in the unit cell volume from the lithiated to the delithiated state. It has a flat potential plateau for charge and discharge, owed to its mechanism, where it undergoes a phase transition upon reaching a sufficient lithium content of $Li_7Ti_5O_{12}$[61] Its disadvantage is that LTO has a low Li^+ diffusion coefficient and a low electronic conductivity below 1e-13 S/cm, which translates into a poor performance at high charge rates.[58,62,63]

The most researched alloy forming anodes are Si and Silicon Oxides (SiO_x). Silicon offers a very high specific capacity of up to 3579 mAh/g and energy density of up to 2194 mAh/cm^3 at room temperature.[57,64] Its voltage against Li^+/Li is slightly higher than graphite at 0.4 V and it is a readily available nontoxic material.[57] The biggest issue for Si is the severe volume expansion it undergoes during lithiation, where it can expand up to 300% if its full capacity is leveraged.[64,65] On the one hand this leads to cracking of the particles, which damages the SEI layer, that formed on its surface and leads to a consumption of electrolyte and available Li^+ each time this happens, causing a rapid capacity fade. On the other hand this can cause the silicon particles to lose electrical contact from the current collector, due to delamination, which also lowers the coulombic efficiency.[64] The most common method to circumvent this is to size down the Si particles to the nanometer regime, so the individual volume expansion is comparatively low. These structures range from just nanoparticles to nanowires and nanosheets. To keep the electrical contact, as Si alone is a rather poor electrical conductor, different 3D nanostructures with conductive carbon coating have been used, such as Core shell structures, to further improve the cycling stability. This cycling stability comes at a lower capacity, as the large surface area consumes more Li^+ and electrolyte to form a SEI layer.[66,67] Therefore, Silicon oxides are often used, which contain a mixture of Si and SiO_2. Due to the oxygen present, there is a smaller volume expansion at the cost of a lower initial capacity. Since the c-$Li_{15}Si_4$ phase, responsible for the largest volume expansion, is not accessible due to the SiO_x structure the cyclability is improved.[57,68] Though there is still a large volume expansion present, through the usage of binders, keeping everything together and mixing it with graphite, batteries with Si/C composite anodes have already been commercialized.[69,70]

In the conversion type anodes transition metal compounds, which can be sulfides, oxides or phosphides, get reduced by the Li^+ ions upon charging and the corresponding lithium sulfide, -oxide or -phosphide forms. A general reaction equation is shown in equation 2.5, where M can be Fe, Co, Cu, Mn or Ni and N can be O, P, S or N.

$$M_xN_y + zLi^+ + ze^- = Li_zN_y + xM \tag{2.5}$$

They can have high capacities (500-1000 mAh/g), since there are a lot of electrons participating in the reaction. The main drawbacks are that they have a low coulombic efficiency and a poor cycle life, owed to an unstable SEI formation, large overpotentials and higher insertion potentials, which is why they remain mainly a research focus and have not been commercialized so far.[71–73]

The last one is lithium metal, which is a category of its own. It possesses the lowest electrochemical potential at -3.04 V vs NHE and the highest theoretical capacity, achievable for an anode in the lithium-ion system with 3860 mAh/g.[27] It is also rather lightweight, owing to the low density of lithium. The main issues for lithium metal as an anode material are twofold. The first issue is that due to the low potential of lithium metal, there is no electrolyte, so far, which does not react with it. The formation of a SEI layer and the passivation of the surface makes operation of a lithium metal anode in a battery cell possible.[27,48] Since there is no host material for the lithium to intercalate into or alloy with, the whole surface morphology can change during cycling.[74] This can damage the SEI and lead to low coulombic efficiency, as the SEI has to reform regularly, consuming electrolyte and lithium. The bigger issue is the high likelihood of lithium to deposit in dendritic structures, as many metals do when electrodeposited.[74,75] These dendrites can continue to grow through the electrolyte, penetrating the separator and causing an internal short circuit.[76] The Joule heating of the cell can cause the electrolyte to evaporate and in the worst case to ignite. These safety concerns were the main reason why the lithium metal anode was discontinued in favor of the graphite anode, as the likelihood of dendrite growth is reduced due to the intercalation mechanism.[27]

2.2.2 Cathode materials

For cathode materials on the other hand there are only two main categories, which can be characterized on the mechanism

- Intercalation materials
- Conversion materials

Lithium cobalt oxide $LiCoO_2$ is the first oxide-based cathode material that was researched in the 1970s and it follows an intercalation mechanism.[42] It possesses a layered structure with alternating Co^{3+} and Li^+ planes in a rock salt crystal structure, which changes into a layered $CdCl_2$ structure upon removal of the lithium. The 2D layers allow for a fast diffusion for Li^+ into and inside of the structure. The theoretical capacity is 272 mAh/g but practically only around 140 mAh/g is accessible as only half of the Li^+ can be intercalated and removed reversibly. If more is removed, a phase transition to a monoclinic structure occurs at a Li content of 0.4 and the layered structure cannot be maintained.[44,45] Though the material is a commercial success, its comparatively low capacity and ethical concerns regarding the mining of cobalt have led to the search for alternatives.[77]

Lithium manganese oxide, $LiMn_2O_4$ or LMO, has a lower capacity than $LiCoO_2$ with a theoretical capacity of only 148 mAh/g, but Mn is less expensive, more abundant and less tainted with ethical concerns for its procurement.[78] It possesses a spinel-type crystal structure and has a 3D Li^+ diffusion path compared to the 2D layer insertion of $LiCoO_2$.[79] Though it is rather safe during charging, it shows poor cycling performances. This is attributed to the dissolution of Mn ions into the electrolyte, which can be remedied with additives, and loss of crystallinity when discharged due to Jahn-Teller distortions caused by Mn^{3+}.[80–82]

$LiNiO_2$ is structurally similar to $LiCoO_2$ and has a theoretical capacity of 275 mAh/g.[83] During cycling Ni^{2+} can form and block Li^+ pathways causing a low capacity retention.[84] This formation of Ni^{2+} can also happen in reaction with ambient air, reducing calendar life.[85] Through substitution of Ni with Al and Co this phenomenon can be somewhat suppressed. The most common composition is $LiNi_{0.8}Co_{0.15}Al_{0.05}O_2$, NCA, with a theoretical capacity of 279 mAh/g and a potential of 3.7V. Its good cycling stability has led to the commercialization as cathodes in electric vehicles.[57,86]

In order to improve the energy storage capacity of LMO it can be doped with Ni and Co to increase the amount of Li that can be stored inside of the structure and the operating potential. The common formula of Lithium Nickel Cobalt Manganese Oxide, often shortened to NMC, is $LiNi_xMn_yCo_zO_2$, where x,y and z can be between 0 and 1 and form a total of 1. Compared to NCA the energy density is lower but the lifetime and the safety was improved. The most common mixtures are NMC111, with equal Ni, Mn and Co contents at 0.3, NMC622, with 0.6 Ni content and 0.2 for Mn and Co and NMC811, with a Ni content of 0.8 and Co and Mn of 0.1.[57]

If the goal is using more abundant materials then Lithium iron phosphate is the clear choice. $LiFePO_4$, LFP, has a theoretical capacity of 170 mAh/g and a potential of 3.5 V. Almost all of the lithium can be reversibly removed and reinserted into the structure, which is an olivine type crystal structure, where PO_4 forms a rather stable lattice for the Li^+. During cycling a metastable Li_xFePO_4 phase is generated allowing for a high rate capability contrary to an expected two phase reaction mechanism.[87] It also has very good thermal stability during charging and excellent cycling performance, though a rather poor electronic conductivity, necessitating carbon coating.[57,88,89]

Looking at energy storage chemistries with a different mechanism there are Lithium sulfur batteries and more specifically sulfur anodes. There Li^+ ions are converted into Li_2S according to equation 2.6. This reaction takes place at 2.15V vs Li^+/Li and results in a theoretical specific energy of 2500 Wh/kg.[90]

$$16Li^+ + 16e^- + S_8 = 8Li_2S \tag{2.6}$$

This is still in the research stage and a few steps away from commercialization due to poor cycling behaviour and large capacity fading. The reaction from S to Li_2S brings a large volume expansion with it (up to 80%) and this crushes the cathode and removes conductive coatings, which are necessary as sulfur is insulating.[90] Furthermore sulfur can dissolve into the electrolyte in the form of polysulfides. Those polysulfides can pass through the separator, if they have a short length, to the anode and transform into Li_2S further reducing capacity.[91,92]

Lithium air batteries are another large research focus of Li battery systems with conversion-based mechanisms. The reaction of Li metal with oxygen to different lithium oxides or hydroxides, if an aqueous system is used, has the potential to store the most energy, of all lithium based battery chemistries. The cell setup uses lithium metal as an anode and a porous oxygen permeable cathode, which can catalyse the reaction of oxygen.[93] The typical reaction mechanism is shown in equation 2.7 below.

$$2Li^{+} + 2e^{-} + O_2 = Li_2O_2 \tag{2.7}$$

This reaction to Li_2O_2 is chosen because Li_2O is deemed to stable to get the reversible reaction pathway. It occurs at 2.96 V vs Li^+/Li and can reach a theoretical energy density of 8 kWh/l, slightly lower than 10.5 kWh/l that the reaction to Li_2O could theoretically achieve. The biggest issues for lithium air batteries remain in allowing only oxygen to pass through the permeable cathode, if atmospheric conditions are to be used, as well as finding a suitable electrolyte, stable against lithium metal and with a good ionic conductivity. The most promising so far are ether based solutions, while a solid state based approach could also be an avenue to choose.[94]

2.2.3 Electrolytes

The last remaining part of the cell is the electrolyte, which is often put in a polymer or glass fiber separator.[27] It is responsible for allowing ion transport between the electrodes and should in the best case fulfill all of the following criteria.

The electrolcyte should possess a high ionic conductivity, for a fast Li^+ ion transport. The potential window of the electrolyte should be large, so it does not react or decompose during operation of the battery. There should be no chemical reaction between the electrolyte and other battery components. It should be cheap while also being chemically and thermally stable. Last but not least it should be non toxic, or only of low toxicity. So far there are no electrolytes that fulfill all of those criteria and so tradeoffs have to be made.[89]

Organic liquid electrolytes are one of the most common electrolytes used in Lithium ion batteries, commercially sold today. It consists of one or more organic solvents with a lithium salt dissolved in them. The key parameters are melting, boiling and flash points, solvability of the lithium salts, viscosity and dielectric properties.[89] The first point is more safety related, whereas the later ones focus more on the performance. The solvents can range from linear carbonates, like Dimethylcarbonate, DMC, Diethylcarbonate, DEC and Ethylmethylcarbonates, EMC, to cyclic carbonates like Ethylenecarbonate, EC and Propylenecarbonate, PC. There are also ethers in use like Dimethoxyether, DME and Tetrahydrofuran, THF. Other solvents used are Acetonitrile, Dimethylsulfoxide and Butyrolacetone. Linear and cyclic carbonates are often used as a mixture to tune the solvability and viscosity, e.g. EC/DMC in a 1:1 ratio.

For the lithium salts large anions are preferred, as they release the Li^+ ions more easily into the solvent such as $LiPF_6$ or Lithium bis(trifluoromethanesulfonyl)imide, LiTFSI.[57,95,96] All of these electrolytes mentioned so far are not stable against the low potential of the anode, regardless if it is graphite or lithium metal, and thus reduce upon contact and further electrochemically during cycling. The products of this reduction, which are stable at the anode potential, deposit as a layer on the anode. This layer, which was a key factor for allowing lithium-ion batteries to work, was named the solid electrolyte interphase and passivates the surface while still conducting lithium ions. The properties of the layer depend on the decomposition products of the specific electrolyte and any additives, which may be added to improve said properties.[57,97] Furthermore, the initial electrochemical reduction plays a major role in the morphology and attributes of the layer. Ideally the layer should be electrically resistive, to self-limit further growth, ionically conductive, while only transporting Li^+ for battery performance and the surface morphology should be as homogeneous as possible. Quite often though the SEI is quite heterogeneous, both in topography and in the lithium ion mobility.[98,99] This in turn causes the current distribution to be inhomogeneous, which will be relevant for the discussion of dendrite growth later on.

2.3 Li-ion batteries - Safety issues

One important property of lithium ion batteries, with their ubiquitous presence in our daily life, in powering electronics, transportation and medical equipment is safety.[100,101] As with any energy storage form, a spontaneous release of the banked energy can have severe consequences, so understanding how and why it can happen is rather important. For lithium ion batteries this can occur in multiple ways. The organic liquid electrolytes often used, have a rather low ignition point, which depending on the mixture used is between 100 and 200°C, and can easily catch fire when the battery is damaged, heated or overcharged.[102] As the battery cell is sealed to protect it from the atmosphere due to the moisture and air sensitivity of its parts, it can also transform into a pressure vessel if the temperature is at a level where the electrolyte evaporates but does not ignite yet. At elevated temperature levels where the electrolyte is still liquid, the battery performance can often increase as ionic conductivity rises and the viscosity of the electrolyte decreases. Increased temperatures also enable parasitic side reactions in the cell, which can be further promoted by overcharging. Those side reactions can be decomposition of individual components, be it cathode, electrolyte, the SEI layer on the electrodes or a combination of all of them.

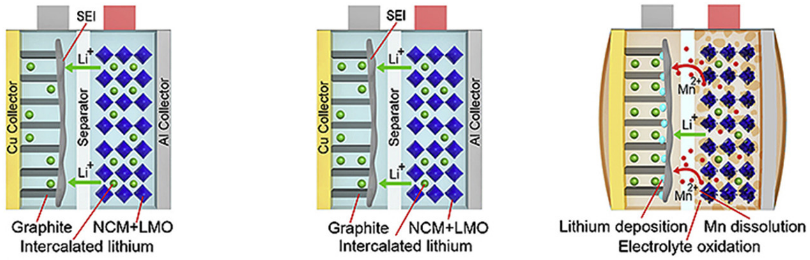

(a) Before overcharge (0<SOC<1)

(b) Stage I (1<SOC<1.2)

(c) Stage II (1.2<SOC<1.4)

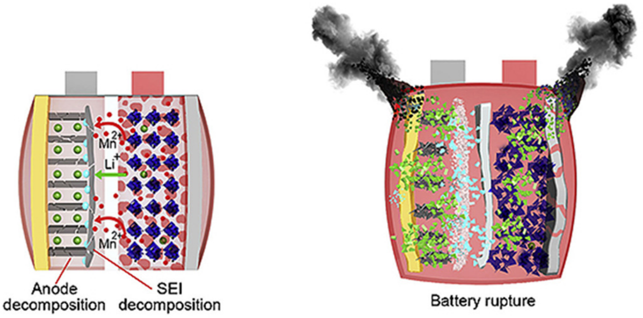

(d) Stage III (1.4<SOC<1.6)

(e) Stage IV (SOC>1.6)

Figure 2.2: Overview of overcharge side reactions at different state of charge for a NCM-LMO lithium ion battery culminating in a thermal runaway with battery rupture. Reprinted with permission from Ren et al[24]

This process of depcomposition followed by failure from overcharging is shown schematically in figure 2.2. Heat is often generated as a byproduct which starts the vicious cycle, as the rising temperature boosts those side reactions. If the temperature cannot be controlled anymore it enters what is called a thermal runaway and can affect the surrounding cells by heating them up as well.[24] This way if a single cell heats up it can affect the whole battery and in the worst case, if the safety features fail, ignite the battery, most often the electrolyte, or cause an explosion if the pressure gets too high.[103,104] Next to mechanical abuse of the battery this process can also be caused by a short circuit, be it an external one or one happening within the battery, through dendrite growth.

2.4 Li-ion batteries - Dendrite growth

Taking a step back from Li-ion batteries and looking at a more general case where dendrites can grow, that is in principle the same, the electrodeposition of metals. When depositing metals from a solution onto a flat surface the morphology of the deposited surface can be divided into three cases, split up according to the exchange current densities, which is the current density I_0 where no net current flows and there is no overpotential of the system. Assuming low overpotential, if I_0 is low, a compact layer will be deposited, for a large I_0 it will be of a spongy morphology and at a very large I_0 boulders will deposit. In all cases if the overpotential gets higher dendritic growth will occur.[105] Therefore the conditions for electrodeposition can be tuned, by changing the solvent and inserting additives to shift the exchange current density to the desired level for a process. In lithium metal batteries the desired case is to achieve a compact metal layer and simulations agree that a low exchange current density would lead to such a layer.[106] This is shown in figure 2.3

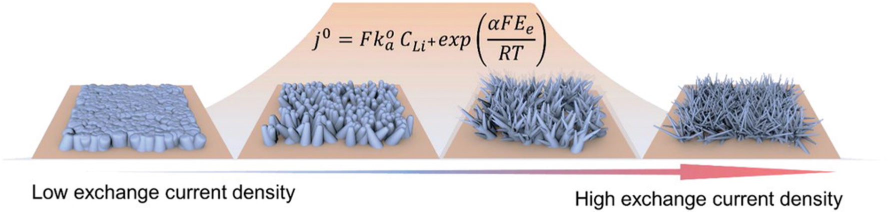

Figure 2.3: Schematic of electrodeposition behaviour of Li under different exchange current densities. Reprinted with permission from Liu et al[106]

Another important aspect is the surface morphology of the substrate plated onto. For real substrates the surface is not atomically flat and will possess a certain surface roughness. Under the caveat that the deposition takes place under diffusion control, the surface roughness can increase under deposition. This is caused by preferential deposition on protruding parts of the surface, which have a thinner effective diffusion layer and therefore experience an increased diffusion flux and current density. This increase in the roughness of the surface rises with the applied current density. If deposition occurs under conditions where only a tip experiences diffusion control, then carrot like growth can occur, even at low overpotentials. Once the overpotential is high enough it will change to a dendritic growth type.[105] Critically for Li-ion batteries charging quickly, with a high current, leads to high overpotentials, which in all cases mentioned here cause dendritic growth. Furthermore, compared to electrodeposition, where a flat polished substrate surface can be chosen to avoid going into the dendritic growth regime, the available morphology is determined by the SEI layer, which can be quite heterogeneous.[107] This combined with the fact that the battery as a whole is a rather complex system with many tunable variables and many different observations of dendrite growth behavior makes the elucidation of the mechanism rather difficult.

Observed phenomena so far regarding the growth mode are, that dendritic growth can be base controlled, where the deposition takes place at the base and this pushes the inactive tip forward[108–110], to the opposite, that certain conditions cause a tip controlled growth, where the tip is electrochemically active and the focal point for the depositing lithium[111], as well as transitions between those two states.[51,110,112]

Using this knowledge different mitigation strategies are employed for conventional lithium ion batteries. Often additives are put into the electrolyte, which can influence the formed SEI layer, or inhibit continued dendrite growth by co depositing with the lithium, or increase the overpotential necessary for lithium deposition, making intercalation more likely.[113–115] The current waveforms during charging can be varied, with current pulses being able to extend the lifetime significantly, by allowing diffusion gradients to dissipate in between current applications.[29] This concept will be explored in more detail in later parts of this work.

2.5 Solid electrolytes

One possible remedy for safety issues caused by dendrite growth and maybe even dendrite growth itself, is to exchange the flammable liquid electrolyte with a non-flammable solid electrolyte. Being a solid it could also pose as a mechanical barrier against the soft lithium metal, whose growth encountered little obstacles in a liquid electrolyte and the polymer separator which it could penetrate.[28]

Performance wise they should fulfill the same criteria as liquid electrolytes, allowing fast ion transport, preferentially only of Li^+, while not conducting electrons, being chemically stable, thermally stable and affordable. They shoud also be compatible with lithium metal, as the decrease in energy density from the increased weight of the electrolyte, can often only be compensated by increasing the capacity of the anode, moving from graphite to lithium metal.[116] Some promising candidates are based on a sulfide chemistry, such as the Li-P-S systems, which can be doped and varied in its composition to arrive at argyrodite based structures with the general formula Li_6PS_5X, where X can be Cl, Br, or I, or at $Li_{10}GeP_2S_{12}$.[117–119] They have high ionic conductivities, with $Li_{9.54}Si_{1.74}P_{1.44}S_{11.7}C_{l0.3}$ possessing the highest reported one so far at 2.5e-2 S/cm at room temperature, which exceeds the conductivity of liquid electrolytes.[120] The sulfide based materials are also rather soft and can easily be densified by cold pressing or calendering, if a tape casting process is used, allowing for rather easy scaling up from a lab production to an industrial one. However, they are very sensitive to moisture, forming H_2S as a toxic decomposition product. Furthermore, they are not thermodynamically stable against lithium metal, decomposing on prolonged contact and during cycling, necessitating interlayers for stability.[121]

2.5.1 LLZO

Another promising chemistry is based on oxides, more specifically $Li_7La_3Zr_2O_{12}$ (LLZO) based solid electrolytes, which show more stability against lithium metal and is therefore used throughout this work.[122] The first $Li_5La_3M_2O_{12}$ garnet, where M can be a transition metal like Nb or Ta, was reported in

2004 by Thangadurai et al.[123] Cubic LLZO, with a higher lithium content than the aforementioned garnets, was first synthesized in 2007 by Murugan et al. At the time its lithium-ion conductivity at room temperature was rather high with 5e-4 S/cm closing in on liquid electrolytes, which are in the range of 1e-2 S/cm.[124] The tetragonal polymorph, which is thermodynamically more stable, was first properly characterized in 2009 by Awaka et al. and has a ionic conductivity two orders of magnitude lower than the cubic counterpart.[125] Through the introduction of dopants into the structure the cubic phase can be stabilized at room temperature and the ionic conductivity can be increased even further. LLZO belongs to the garnet structure, which is derived from the general orthosilicate in the form $A_3B_2(SiO_4)_3$, where A is a divalent transition metal or metal cation, and B is a trivalent cation. The three different cation sites make for a rather complex structure with the A dodecahedra, B octahedra and the Si tetrahedra. Looking at it from the Anion site, shows that there is only one possible coordination environment. The Oxygen is bonded to one Si^{4+}, two A^{2+} and one B^{3+} and this repeats throughout the structure. The crystal structure is shown in Figure 2.4

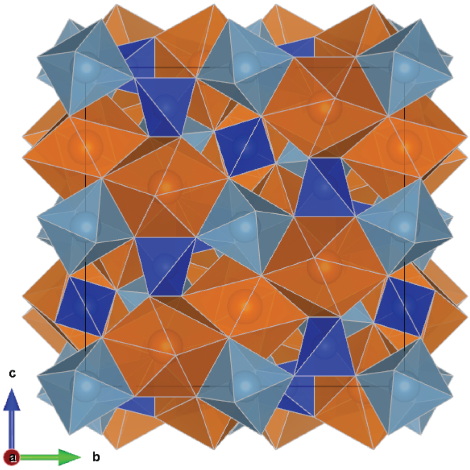

Figure 2.4: Crystal structure of the cubic garnet $Mg_3Al_2Si_3O_{12}$ created in VESTA.[126] The Al^{3+} is shown in green, the Mg^{2+} in orange and the Si^{4+} in blue.

For LLZO there is a tetragonal and a cubic polymorph with their crystal structures shown in Figure 2.4a and b respectively. The tetragonal structure has the space group I41/acd (no. 142) with Li^+ sitting on the three different, fully occupied interstitial sites. The tetrahedral 8a site and the distorted octahedral 16f and 32g sites. Two different LaO_8 dodecahedra occupy the 8b and 16e site and ZrO_6 octahedra are at the 16c site. The lattice constant a is 13.134 Å and the lattice constant c is 12.663 Å.[125]

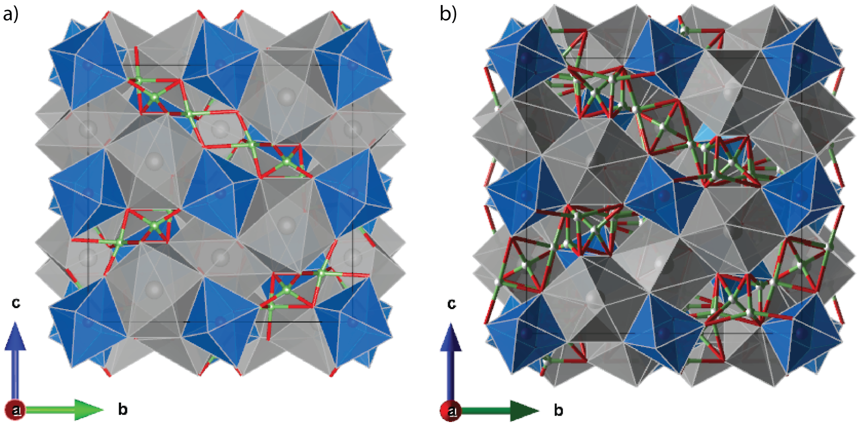

Figure 2.5: a) Crystal structure of tetragonal LLZO. b) crystal structure of cubic LLZO both created in Vesta.[126] Li^+ shown in green, La^{3+} in grey and Zr^{4+} in blue

The cubic structure, which is energetically favoured at higher temperatures, has the space group Ia$\bar{3}$d (no. 230). Here the Li^+ is at also at interstitial sites, the tetrahedral 24d, octahedral 48g and 96h sites. The occupancy of those is random and partial allowing for easier Li^+ conduction, compared to the tetragonal structure where the fullly occuped sites block the Li^+ passage. The LaO_8 dodecahedra is at site 24c and the ZrO_6 octahedra is at site 16a. The lattice constant a is 12.9682 Å.[127]

2.5.2 Phase transition

According to DSC the phase transition from tetragonal to cubic starts at around 700°C.[128] Depending on the dopant and synthesis method used, temperatures between 750°C and 1230°C are necessary to create the cubic phase. Higher temperatures are preferable to sinter a more dense ceramic but increases lithium loss due to vaporization, which can change the stoichiometry. During the phase transition from tetragonal to cubic the a-axis shrinks while the c-axis elongates. For the tetrahedral interstice the fully occupied Li^+ 8a site and the fully vacant 16e site transform into the partially occupied 24d site. In the octahedral interstice the Li^+ from the fully occupied 16f and 32g site moves into the partially occupied octahedral 96h site. The spacing between La and O does not change. The ZrO_6 octahedra on the other hand gets slightly distorted, the bond length changing from 2.125±0.005 Å to 2.130±0.020 Å. The bond angle between Zr and O also varies more, due to the disorder, from 180±0.01° in the tetragonal structure to 180±4.0° in the cubic one, which is energetically more unfavourable. This is balanced out by the higher entropy at high temperatures making the more symmetrical cubic structure possible.[129] The phase transition can be described as a mixture of a displacive transition, in the ZrO_6 octahedra and an order-disorder transition in the lithium sublattice.

2.5.3 Dopants and Defects

The cubic phase of LLZO is not thermodynamically stable at room temperature and therefore has to be stabilized by the addition of dopants. These increase the disorder in the structure, introduce more vacancies and create more possible configurations and therefore make it energetically more favourable to stay in the cubic structure, even at lower temperatures. In LLZO there are three possible dopant sites, the Li site, the La site and the Zr site. For the lithium site Fe^{3+}, Ga^{3+}, Al^{3+} or Ge^{4+} have already been used. In the lanthanum site Sr^{2+}, Ce^{4+} Ca^{2+} and Nd^{3+} were substituted. The Zirconium site has the largest number of possible dopants with Gd^{3+}, Y^{3+}, Ta^{5+}, W^{6+} just to name a few.[130]

Introducing slightly different sized ions widens the lattice parameter, while additional vacancies are induced by the need to compensate the charge difference.

This is shown prototypically for Ga^{3+} at the lithium site in equation 2.8 using Kröger-Vink notation, vacancies are introduced to satisfy charge neutrality.

$$Ga^{3+} + 3Li_{Li}^{x} = Ga_{Li}^{**} + 3Li^{+} + 2V_{Li}^{'} \tag{2.8}$$

Intrinsically, for the Lithium sublattice, it is possible for Li to move to a vacancy site, shown in equation 2.9 or to an interstitial site again in Kröger-Vink notation, in a Frenkel cation defect, shown in equation 2.10 to form point defects.

$$Li_{Li}^{x} = Li_{V}^{*} + V_{Li}^{'} \tag{2.9}$$

$$Li_{Li}^{x} = Li_{i}^{*} + V_{Li}^{'} \tag{2.10}$$

Computational studies have shown that lithium movement to interstitial sites is not favored and vacancy formation is more likely.[131] For orthosilicate garnets in general, the stability of the structure depends on the relation of the cation sizes in the A and B site.[132] In regard to single ion doping this means that there is only a specific amount of the different sized dopant ion, which can be incorporated into the structure before it breaks down. This should also hold true for LLZO and there seems to be an optimum in the lattice parameter, where the ionic conductivity peaks. This is the case when the lattice parameter is in the range of 12.91-12.98 Å, with every kind of dopant and on every dopant site. Any further expansion of the lattice destabilizes the garnet structure. Lower lattice parameters can reduce the size of the lithium channel impairing Li^{+} movement.[130]

2.5.4 Ionic conductivity and conduction pathway

In a purely ionic conductor, the conductivity depends on the number of mobile ions n, their charge q*e, and the mobility of the ions µ. This is expressed in equation 2.11.

$$\sigma = \Sigma_i n_i q_i e \mu_i \tag{2.11}$$

For LLZO the number of mobile ions is determined by the lithium and the vacancy content, whereas the mobility depends on the energy barrier for Li^+ hopping influenced again by the vacancy content, the vacancy distribution and the possible conduction pathway given by the crystal structure. In the cubic structure Li^+ ions sit at the centre of tetrahedra in the 24d site, and at the octahedral 96h sites, which are slightly displaced from the 48g site. Neither of those sites are fully occupied and the vacancies allow for single ion motion. The connected octa- and tetrahedra form the complete pathway throughout the unit cell as shown in Figure 2.6.

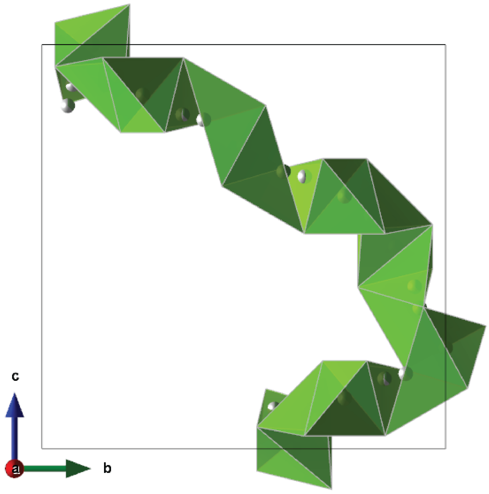

Figure 2.6: VESTA created depiction of the connected lithium-polyhedra, colored green, forming the Li^+ pathway in cubic LLZO[126]

NMR results suggest that the lithium ions at the 24d position are not mobile at lower temperatures and only participate in the conduction in inconsequential amounts.[133] Molecular dynamics simulation show that depending on where a lithium ion jumps it can either be a single ion motion or cause cooperative motion.[134] The experimentally determined ionic conductivity for cubic bulk LLZO is in the range of 1e-4 to 1e-3 S/cm, depending on the exact composition and the dopants used.[130]

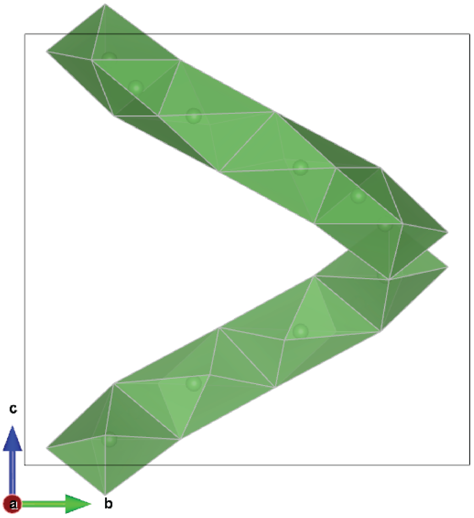

Figure 2.7: VESTA created depiction of the connected lithium-polyhedra, colored green, forming the Li^+ pathway in tetragonal LLZO[126]

In the tetragonal structure on the other hand the tetrahedral 8a site is fully occupied and there is an ordering in the partially filled octahedral 16f and 32g sites. The pathway is shown in Figure 2.7 This prohibits single ion jumps and Li^+ ion transport is only possible when there is a concerted motion of vacancies and Li^+. This increases the energy barrier necessary for Li^+ movement to 0.54 eV and is a reason why the ionic conductivity is two orders of magnitude lower compared to the cubic structure.[125,134]

2.5.5 Electronic structure

According to density functional theory, DFT, calculations by Thompson et al. the calculated band gap of pure cubic LLZO lies between 4.33 eV and 6.42 eV depending on the calculation method and k-point sampling density. Introducing dopants increases the calculated bandgap of a undoped cubic LLZO, from 5.79 eV to 5.87 eV for 0.25 formula units Al doping and to 5.85 eV for 0.5 Ta doping.[135] Calculations of different LLZO surfaces put the position of the upper band edge of LLZO above the one for Li, albeit the difference can be small such as 0.2 eV, and the lower band edge far below an assumed hypothetical 5V cathode. The resulting electrochemical window is shown in Figure 2.8. While this would suggest that the electrochemical window of LLZO is wide enough for the use of a lithium metal anode and a high voltage cathode, the energy difference between the band edges of LLZO and Lithium can be rather small. Furthermore, effects at the interface, which were not considered in this calculation since it only assumes a LLZO slab in contact with vacuum, can vary the electrochemical window locally influencing the stability.[135] Other DFT calculations regarding the stability of LLZO with various anode and cathode materials at the interface show a drastically lower electrochemical window of around 3 eV though the decomposition likely stops kinetically since the products are more stable.[122,136]

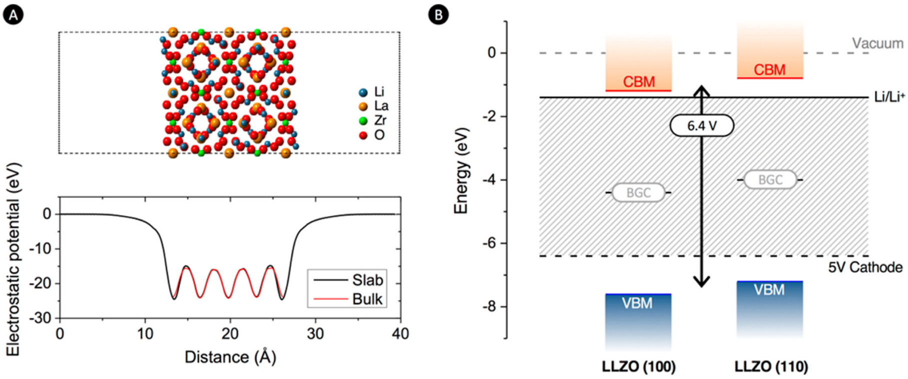

Figure 2.8: a) LLZO in the lowest energy orientation (100) used for the model, with the planar-averaged electrostatic potential at the bottom. b) Calculated electrochemical window. Reprinted with permission from[135]

2.6 Dendrite growth in solid electrolytes

The underlying issue of preferential plating causing dendrite growth still remains for solid electrolytes and is arguably even more severe. In contrast to a liquid electrolyte, which will wet the electrodes given enough time, contacting the electrodes is a more difficult endeavor using solid electrolytes. It was theorized that a solid could pose a mechanical barrier for lithium dendrites and so the preferential plating should be less of an issue. Simulation work, e.g. done by Monroe and Newman or Barai et al, supports this hypothesis.[28,137] To the detriment of this idea, dendrites are still able to penetrate solid electrolytes and short circuit cells, though with less severe consequences. Shown in Figure 2.9 are dendrites grown in LLZTO and LPS. In contrast to liquid electrolytes the dendrite growth happens at much lower current densities, limiting charge rates that can be applied.

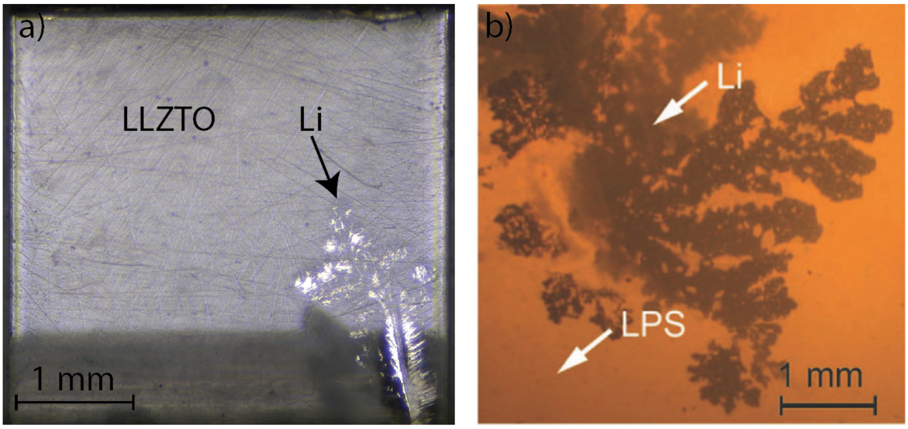

Figure 2.9: Dendrites grown in LLZTO (a) and LPS (b). b) is adapted with permission from Porz et al[138]

The question is therefore how the softer lithium metal is able to create a path through the more mechanically stable solid electrolyte. One theory is that the lithium cracks open the solid electrolyte mechanically starting from existing flaws on the surface of the solid electrolyte. This was explored by Porz et al and their postulated mechanism is summarized briefly below.[138] The premise is that surface flaws are present on the solid electrolyte, size and density of the flaws depending on the surface treatment. The flaws can be filled first by the plated lithium. The local current density is going to be higher at the flaw, compared to the surface that is at a higher distance apart from the other electrode.[139] Once the flaw is filled, lithium continues to deposit and the lithium flux away from the flaw is exceeded by the flux towards the flaw. Therefore, mechanical stresses will rise in the filled flaw. Porz et al set up a model to determine the stress exhibited in a crack that progresses inside the solid electrolyte, where it relates the thickness of the deposited lithium filament, the Poisson ratio ν and the friction coefficient µ to the stress along the length of the filament. Inserting values gained from their experiments, with filament thicknesses of 300 nm and assuming typical values for ν and µ they arrive at a filament length of 1 μm. Cracks exceeding the aspect ratio of $\frac{300nm}{1\mu m}$ can experience hydrostatic pressure buildup leading to fracture. One assumption taken for the model is that the stress far away from the tip of the filament is zero. Cracks which have a smaller aspect ratio could extrude the lithium which, combined with other stress relaxation effects near the surface can cause it not to propagate. The hydrostatic pressure $\sigma_{0,max}$ exerted during fracture is related to the overpotential $\delta\Phi$, the Faraday constant F and the molar volume of lithium plated V_m^{Li} according to the following equation 2.12.

$$\sigma_{0,max} = -F/V_m^{Li} * \delta\Phi \tag{2.12}$$

The stress needed to fracture the material then depends on the crack geometry and the fracture toughness of the material. The fracture toughness of solid electrolytes can vary, depending on the density, grain size, and chemical inhomogeneities.[140]

Evidence is also shown that lithium can penetrate along grain boundaries and voids in solid electrolytes, which can be mechanically weaker than the bulk material, lending further credence to a fracture based mechanism.[141–143] Another theory, which is based on neutron depth profiling measurements of the lithium concentration profile within LLZO, Li_2S-P_2S_5 and Lithium Phosphorus Oxynitride, LiPON, while plating lithium metal, is that an increased electronic conductivity causes the reaction of electrons with Li^+ within the solid electrolyte. This forms dendrites which are detached from the cathode it is plated onto.[144] Han et al base this hypothesis upon a uniformly rising lithium profile, as opposed to a expanding peak, they would expect from a growing dendrite combined with seemingly non connected dendrites in a FIB cross section of a shorted solid electrolyte. Though recent results from transparent solid electrolytes, LLZO specifically, do not repeat this observation of non-connected dendrites.[35] A weakness of this theory is that it does not explain how the electrons are able to skip all the available lithium ions in the LLZO to form lithium metal within the solid electrolyte.

Since most solid electrolytes are not transparent, locating and observing dendrites is now a not trivial issue. One solution is to use highly dense solid electrolytes, such as single crystals or hot pressed polycrystals, which can have a higher transparency. Another approach is to thin down the solid electrolytes until they are almost see-through. This can be combined with using small electrodes so the area where the dendrite has to be located in gets smaller. This combination was used on Al doped LLZO by Kazyak et al to investigate the morphologies of the growing dendrites. They found that when low current densities were applied straight cracks dominated. At higher current densities it transitioned into a more branching structure, coming close to the traditional dendrite structure. Due to being limited in the observational capabilities it is still unknown why the dendrites branch.[145] Focused ion beam scanning electron microscopy, FIB-SEM can be used to cut into the material and get a 3D overview of the shape and extent of dendrite growth at given parameters, though the milling of the material with the ion beam causes some information to be lost. X-ray computer tomography can observe the inner parts of solid electrolytes, but the temporal and spatial resolution can be lacking to detect lithium dendrites.[146] Therefore, information about what happens in the environment next to the dendrite tip is rather lacking in solid electrolytes. Due to the difficulty in linking the employed conditions, such as local current, and when a dendrite grows in the solid electrolyte, there are often only phenomenological descriptions of dendrite growth. Therefore, failure criteria such as the critical current density, also called CCD, which describes the current density when dendrites grow, were established to create an improvable parameter in relation to dendrite growth. The CCD can often be sample specific and is not necessarily material specific, as the sample conditions, such as surface quality, wetting behaviour and surface layers, can influence it quite significantly.[147–149]

2.6.1 Countermeasures against dendrites

So far most of the mitigation strategies against dendrites in solid electrolytes have focused on improving the interface between the electrolyte and lithium metal. The idea is to stop the dendrite as early as possible to stop the vicious cycle of current inhomogeneity promoting dendrites, increasing the current at the dendrite tip, in its infancy. Focusing just on LLZO the methods range from a mechanical surface polishing followed by heat treatment in Argon atmosphere to remove less conductive Li_2CO_3[150], to introducing interlayers, like LiF or Co_3O_4[151,152] or alloying the lithium metal with Na or Sn to improve the wetting behaviour[153,154]. Another approach is to increase the available surface area with a porous-dense-porous trilayer structure, thus keeping the equivalent planar current density below levels at which dendrites grow.[155] It is theorized that introducing compressive stress into the solid electrolyte can increase the fracture thoughness and thus inhibit the penetration of the dendrite into the solid electrolyte.[34] Eperimental proof of this concept was shown in LLZO, deflecting dendrites via mechanically introduced compressive stress.[35] This concept is explored further later on in this work.

3

Methods

3.1 Overview

This chapter provides an overview of the experimental work performed as part of the Papers I-III. The experiments are presented in detail in the methods section of the corresponding appended paper. A simplified outline is shown in figure 3.1 below

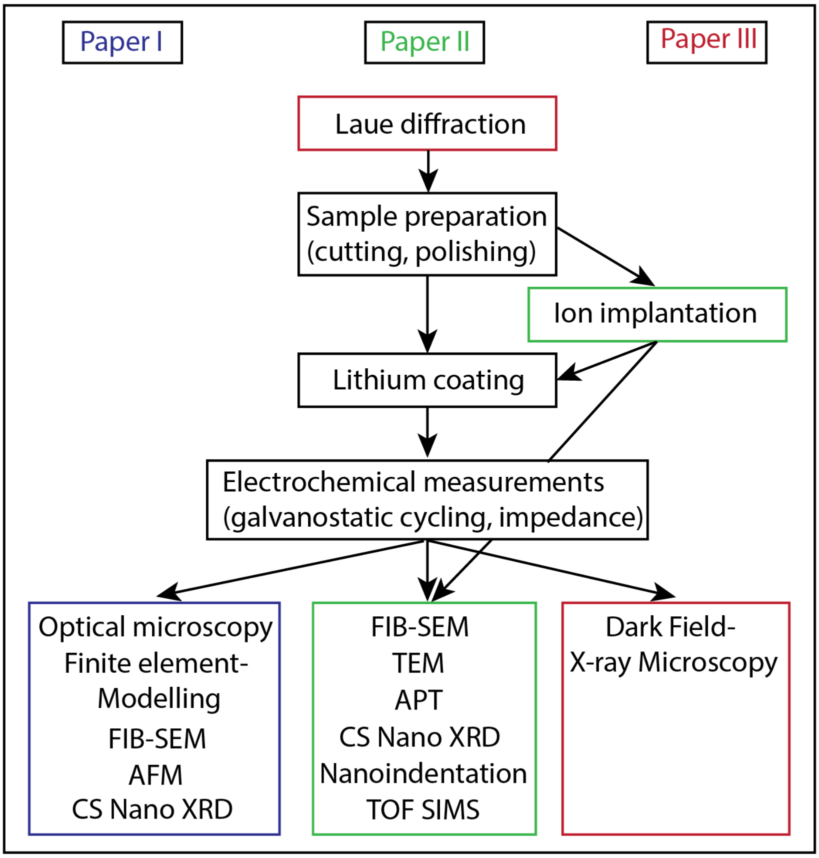

Figure 3.1: Outline of the experimental methods used, color coded to the corresponding paper

3.2 Sample preparation

In this work Czochralski drawn single crystalline $Li_{6.5}Ta_{0.5}La_3Zr_{1.5}O_{12}$, courtesy of the KIZ Berlin Germany and commercially purchased hot pressed polycrystalline $Li_{6.4}Ta_{0.6}La_3Zr_{1.4}O_{12}$ from Toshima were used. They were cut into cuboid shapes using a Well 3500 diamond wire saw. The surfaces were mechanically polished using SiC grinding paper, grit size 500, 800, 1200, 2400, 4000, followed by polishing using MD Dac polishing cloth with diamond suspensions ranging from 3 µm, 1 µm and 1/4 µm employing Isopropanol as a lubricant. In order to remove Li_2CO_3 layers either a heat treatment of around 400°C in Argon atmosphere was applied, or a short acid removal in 0.1M HCl for 10-20s followed by a rinse with Isopropanol was used.

3.2.1 Laue diffraction

Laue diffraction was employed on single crystalline LLZTO to orient it to a known crystal plane before cutting and shaping as described above. A Photonic Science Laue diffractometer was used with the sample mounted on a goniometer to vary the orientation of the sample.

3.2.2 Ion Implantation

As detailed in Paper II ion implantation was performed at the university of Oslo by using a Pelletron implantation system type 3 SDH-2 NEC with a beam energy of 1.930 MeV and a beam dose of 1e14 ^{107}Ag ions/cm^2 . Two parallel sides were implanted, flipping the sample in between the procedure.

3.2.3 Lithium coating

A lithium tin alloy (30 wt% Sn) was applied to two opposite edges of the cuboid shaped samples for electrochemical testing. For this the alloy was molten inside of a stainless steel crucible in an Argon filled glovebox. A stainless steel spatula was used to spread the still molten alloy onto the LLZTO edges, similar to spreading butter on a piece of bread.

3.3 Electrochemical measurements

3.3.1 Impedance measurement

In order to ascertain the coating quality and changes throughout stripping and plating of lithium, potentiostatic impedance measurements were carried out using a Solartron Modulab with a perturbation voltage of 10 mV, from 1 MHz to 0.1 Hz, 19 points per frequency decade. Sometimes the lowest measured frequency was set to 10 Hz if no significant changes were expected in order to save time.

3.3.2 Galvanostatic cycling

To determine the currents at which dendrites formed and penetrated the solid electrolyte constant current was applied and the potential measured. A large focus is placed on this in Paper I where the effect of the applied pulse form during current controlled cycling was investigated. For the duration a constant capacity was assumed and so the duration of current application reduced with increasing current. In Paper II and III currents above the threshold determined in Paper I were used to deliberately cause dendrite growth in the solid electrolyte.

3.4 Material Characterization

3.4.1 X-Ray Diffraction (XRD)

To confirm phase purity of the commercially bought sample a Bruker Da Vinci Diffractometer with a Cu Kα radiation source (λ = 1.5406 Å) was used. A polished and cleaned pellet was placed in a deep Si cavity holder on a piece of plasticine with the surface of the pellet on the same height as the edge of the holder.

3.4.2 Atomic Force Microscopy (AFM)

The Atomic Force Microscopy measurement was carried out on a Cypher ES Atomic Force Microscope from Oxford Instruments(Asylum Research), equipped with a Si cantilever from Budgetsensors(model Tap300GD-G, resonant frequency 300 kHz) and operated in tapping mode under inert gas (Ar).

3.4.3 Cross-sectional nano X ray diffraction (CS nano XRD)

The Cross-sectional nano X ray diffraction was carried out at the beamline ID13 at the ESRF and for this measurement the LLZTO sample had to be mechanically thinned to around 100 µm to allow for x-ray penetration as La and Zr are rather X-ray attenuating atoms. A 13 keV photon energy, monochromatic X-ray beam was focused via multi-layer Laue lenses to an approximately 80 nm spot. The Dectris Eiger X 4M two-dimensional X-ray detector was placed downstream of the beam to measure the diffracted x-rays with an exposure time of 50ms.

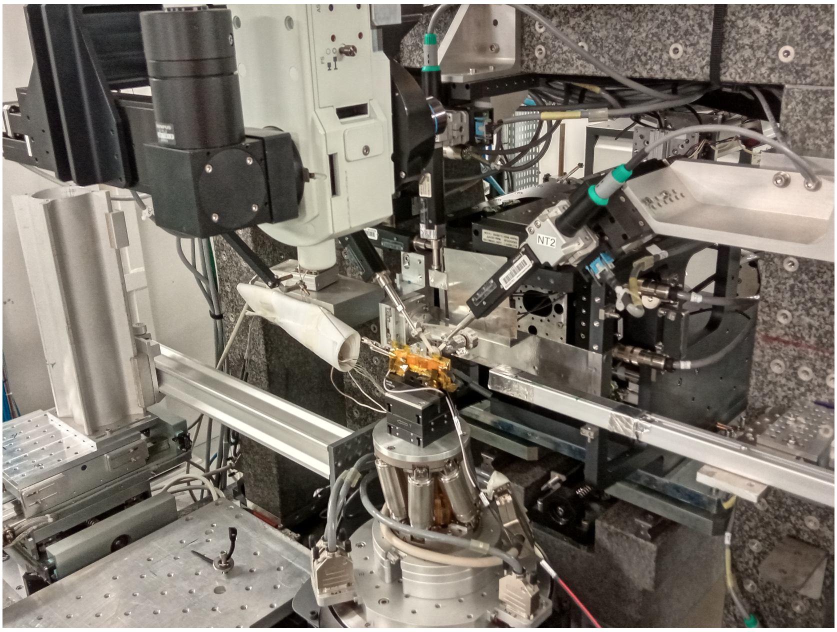

Figure 3.2: CS Nano XRD Setup in the beamline ID13 at the ESRF. The sample being in the middle of the image, covered in Kapton tape. Behind it the X-ray optic can be seen.

3.4.4 Dark Field X-Ray Microscopy (DFXM)

The Dark Field X-Ray microscopy measurement was carried out at the Beamline ID06 at ESRF Grenoble. A LLZO sample was oriented, so a known crystal plane was pointing out of plane and was mechanically thinned to around 100 µm to allow for better x-ray penetration. For the measurement a dendrite was grown partway through the sample. Near Field and Far Field images were taken with the near field detector placed at 25 mm distance in the diffracted beam path, which was swapped after alignment for x ray focusing lenses and the far field detector placed at 5 m distance.

3.4.5 Scanning electron microscopy (SPED)and focused ion beam (FIB)

SEM was carried out on a FEI Helios NanoLab DualBeam FIB or a Helios G5 PFIB, to study the morphology of the solid electrolyte after dendrite growth. Cross sections were made using Focused ion Beam either using Ga ions at the Helios DualBeam or using Xenon ions in the PFIB, to make the effect of the dendrite within the material observable. The TEM lamella was produced and thinned using the standard focused ion beam (FIB) liftout method, with a FEI Helios G4 UX dual-beam instrument. The tips for APT analysis were prepared from a lamella that was lifted out from the Ti coated Specimen, flipped upside-down and welded to flat Si posts inside the FIB. In this way, the Ti surface coating acts as a buffer between the specimen and the carbon-containing welding material, and the apex of each tip could be formed at a controlled distance from the original surface. The tips were formed using annular Ga ion milling, finishing with 2 kV for the final sharpening.

3.4.6 Transmission Electron Microscopy and Scanning Precession Electron Diffraction

Transmission electron microscopy was performed on a JEOL 2100F transmission electron microscope. Scanning precession electron diffraction was performed with a precession angle of 0.8 degrees and a frequency of 100 Hz. 20 ms diffraction patterns were acquired with a MerlinEM direct electron detector. Virtual dark-field imaging was used to separate grains and crystalline/amorphous areas.

3.4.7 Atom Probe tomography (APT)

The atom probe tomography measurement was carried out on a a LEAP 5000 XS from CAMECA equipped with a UV laser with the specimen temperature at 60K. Laser pulses with an energy of 20 to 30 pJ were used at a frequency of 200 kHz to trigger field evaporation. The standing voltage was automatically adjusted by the software to maintain a detection rate of 0 0.3 percent ions per pulse.

3.4.8 Nanoindentation

Nanoindentation was performed on ion implanted single crystalline LLZTO ($Li_{6.5}La_3Zr_{1.5}Ta_{0.5}O_{12}$). The sample was placed in a FT-NMT03 nanomechanical testing system utilized within a Cross Beam 340 ZEISS SEM. Indents were controlled by displacement and were made using a Berkovich indenter tip with an indentation depth of 0.1 µm. After attaching a few µm of Pt protection layer a 20x12x10 µm cross section was cut with FIB using a 20 nA beam current, reduced to 4 nA and 600 pA for final polishing on a cross-beam SEM from Zeiss (AURIGA® - CrossBeam workstation).

3.4.9 Finite Element modelling

A finite element model was employed in an attempt to explain the varying behaviour of pulse plating in Paper I using COMSOL Multiphysics 5.6.

4

Summary of results

4.1 Foreword

In this chapter the main findings of the three papers attached to this thesis are summarized. The following sections contain the main results of those appended papers. The more detailed descriptions can be found in the appendix containing the respective manuscripts.

4.2 Paper I: Effect of pulse current on lithium dendrites

4.2.1 Overview

The first paper focuses on the effect of pulsed currents on the critical current density, the current density where lithium dendrites grow, of LLZO. Commercially acquired hot pressed polycrystalline and Czochralski drawn single crystalline Ta-doped LLZO (LLZTO) were employed in a symmetrical Li-LLZTO-Li cell and cycled with constant current, both with direct current and pulsed current to assess the effects of pulse plating. In operando microscopy observed the dendrite growth and FIB SEM was used for post mortem investigations. To elucidate the mechanism Finite Element simulations were used and the stress caused by dendrites was investigated via CS nano XRD.

4.2.2 Sample Preparation

The hot pressed polycrystalline $Li_{6.4}La_3Zr_{1.4}Ta_{0.6}O_{12}$ (HP) and the single crystalline $Li_6La_3Zr_1Ta_1O_{12}$ (SC) were cut into cuboids with a diamond saw and a multi step mechanical and vibrational polishing procedure was used to minimize surface defects. The effect of this is shown in SEM images in Figure 4.1a and b. Figure 4.1a shows the single crystalline sample, with the geometry visible in the inset, where no polishing marks can be found. Figure 4.1b shows the hot pressed sample, the geometry again visible in the inset, where a slight porosity is still present and the grains are visible with a size of around 2 µm in diameter. To determine the surface quality AFM was used on a HP and a SC sample deemed representative for the whole. The height profile is shown in Figure 4.1c and a RMS roughness of 3 ± 1 nm for the single crystalline sample and 8 ± 3 nm for the polycrystalline sample are achieved. The samples were heat treated in Ar atmosphere at 450°C to remove contamination layers and coated with a molten Li:Sn alloy (30 wt% Sn) to achieve good and consistent wetting. Impedance spectroscopy was employed to determine the quality of the coating and the sample preparation procedure. The effect of the preparation, especially of the heat treatment, is visible in Figure 4.1d, where the Nyquist plots of a single crystalline sample that was coated after heat treatment (black) and one without heat treatment (grey), show a significant second contribution for the sample that was not heat treated. The second contribution is attributed to a Li_2CO_3 contamination layer, which is dealt with via the heat treatment. Figure 4.1e shows the conductivity isotherm of the single crystalline and the hot-pressed polycrystalline sample.

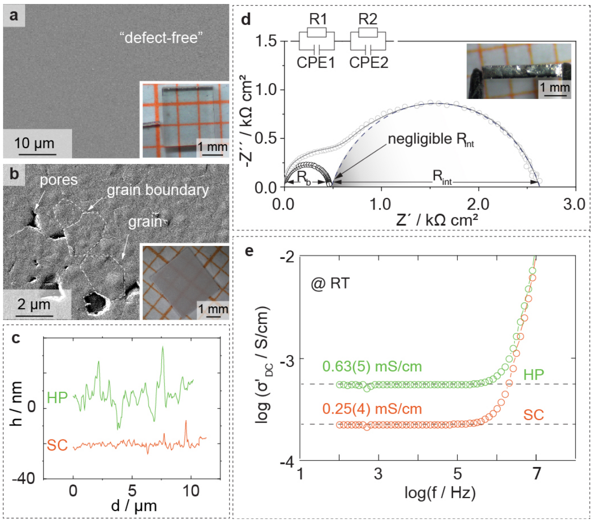

Figure 4.1: a) SEM image of the single crystalline LLZTO, sample geometry shown in the inset. b) SEM image of the hot pressed LLZTO, sample geometry shown in the inset. c) AFM height profiles of single (orange) and hot pressed LLZTO (green), the single crystalline is shifted by -20 nm. d) Nyquist plot of single crystalline LLZO with (black) and without heat treatment (grey). e) Conductivity of the single crystalline (orange) and hot pressed LLZTO (green) in a Bode plot.

4.2.3 Electrochemical Measurements

The coated samples were cycled galvanostatically inside of an Argon filled glovebox, to an assumed capacity of 200 μAh/cm^2, with increasing current densities after each cycle until failure. This was performed with direct current and with a pulsed current program, employing 1 Mhz pulses with a 1:1 pulse to pause ratio. The current density at which dendrites grow is deemed the critical current density. The dendrite growth was also documented via optical microscopy, to better correlate the electrochemical data with the actual growth. The results are summarized in Figure 4.2, where the CCD is plotted for the single crystalline and polycrystalline samples, as well as reports from literature. There is no notable beneficial effect for the use of pulsed currents for single crystalline samples, whereas there is a significant increase in the CCD for the polycrystalline samples.

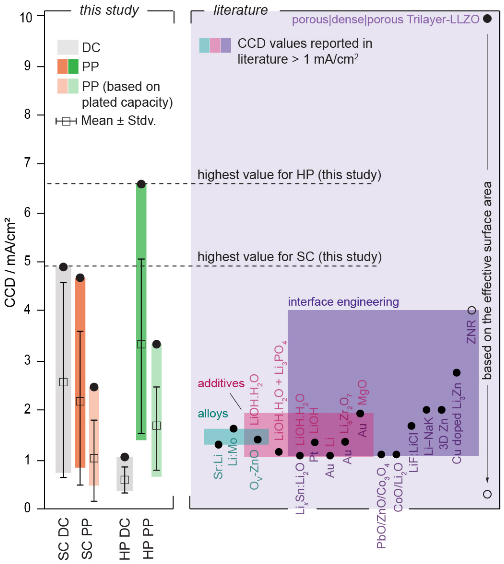

Figure 4.2: CCD values achieved for the single crystalline LLZTO with direct current (grey) and pulsed current (orange) and hot pressed LLZTO with direct current (grey) and pulsed current (green). The effective CCD taking the capacity into account is shown in light orange for the single crystals and in light green for the hot presed LLZTO. On the right the highest reported CCD values from literature are shown.

In order to explain this performance improvement the first approach was to investigate the type of dendrite grown to determine if there is a preferential shape or growth category for direct current or for pulsed current. The detected growth types are shown in Figure 4.3a-b and grouped into three different categories, similar to Kazyak et al, straight, cone or diffuse.[145] There were also examples for multiple initiation sites at once.

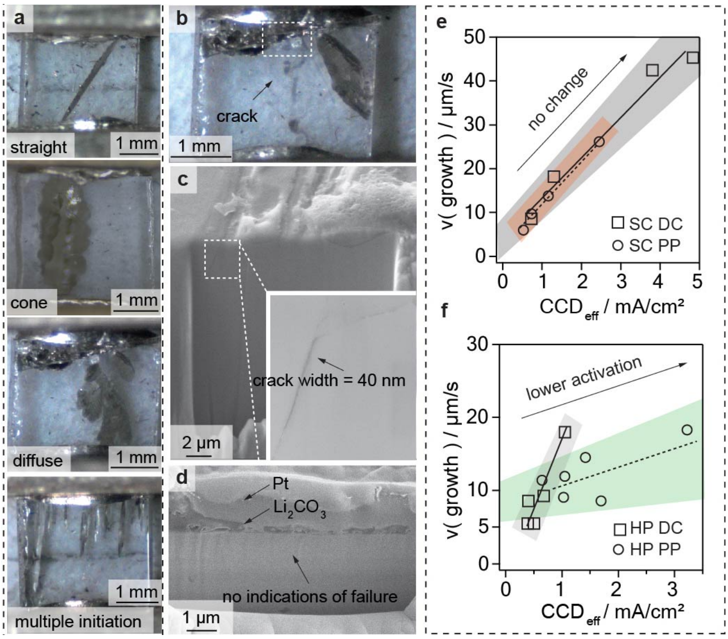

Figure 4.3: a) observed lithium dendrite types in single crystalline LLZTO. b) shorted LLZTO single crystal, the white box denotes the investigated region in the SEM c) FIB SEM cut of single crystalline LLZTO showing the dendrite path. d) FIB cut of a hot pressed LLZTO, no dendrite path could be found with the available resolution. e) growth rate in single crystalline LLZTO for direct current (grey) and pulsed current (orange). f) growth rate in hot pressed LLZTO for direct current (grey) and pulsed current (green)

The crack width was determined via FIB- SEM, being 40 nm in width for the sub-surface cracks found in a single crystalline sample, Figure 4.3c, whereas no signs for crack propagation were found for the hot pressed sample, Figure 4.3d, though this may be due to the resolution limit of the SEM. All of the crack types could be observed for both current waveforms, with the multiple initiation case being limited to high CCDs, so the growth type was not deemed to be the main cause for improvement. The growth rate of the dendrite was also determined via the optical images. It is shown to increase linearly, with the dendrites growing faster at higher CCDs. There was no change in the growth rate between direct and pulsed current for the single crystalline samples, shown in Figure 4.3e. For the hot pressed samples, Figure 4.3f, on the other hand the growth rate decreased when pulsed currents are employed.

4.2.4 The Mechanism

As a basis for crack propagation it was assumed that defects are filled with lithium metal, exerting increasing pressure until the solid electrolyte fractures. Finite element simulations showed that failure occurred instantaneously with applied current and that there should be no effect from the application of pulsed current. Hence our hypothesis is that the Li^+ ion activity surrounding the crack tip is in part responsible for the critical pressure buildup, weakening the surrounding region.

The proposed mechanism is schematically explained in Figure 4.4. Upon application of current Li^+ move toward the filled crack tip and generate the activation front. As the activation front grows larger and distorts the lattice the material is weakened and ultimately fractures, allowing for a growth of the dendrite. If fast enough pulses are employed the activation front can decay and the lattice is only minorly distorted, increasing the applicable current density.

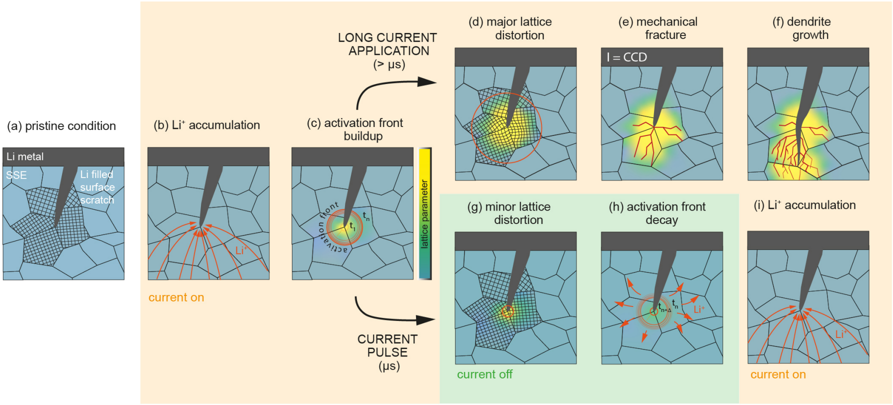

Figure 4.4: Proposed mechanisms in constant current and pulsed current electrochemical experiments

Evidence to support this theory comes from operando cross sectional nano XRD measurements of a growing dendrite, where a deviatoric stress in the order of 750 MPa can be detected surrounding the dendrite tip during growth with direct current. This stress does not decay instantaneously, as would be expected from crack extension which would relax at phonon speed, but after ~10 minutes. Other materials such as $LiCoO_2$ have a similar behaviour where Li ions inserted into the particle cause a volume mismatch, once the relaxation kinetics is slower than the transfer rate.[156] This volume mismatch causes a high enough chemo-mechanical strain to induce plastic deformation, amorphization and mechanical fracturing. To conclude it is demonstrated that pulsed current application can have a beneficial effect for polycrystalline LLZTO, both for the critical current density as well as the growth rate and extends the mechanism for crack propagation.

4.3 Paper II: Deflecting dendrites via ion implantation

4.3.1 Overview

In the second Paper the mitigation of dendrites through deflection via compressive stress was explored. Therefore, Ag ions were implanted into the surface of LLZTO up to 1 μm deep, according to SRIM simulations. The implantation profile and the compressive stress was characterized by CS Nano XRD. It was attempted to locate the Ag ions via SPED and APT, though only a qualitative determination via TOF SIMS was successful. Cracks were induced mechanically as well as electrochemically and successful crack deflection is shown.

4.3.2 Sample Preparation

Similar to Paper 1 the first step was shaping the samples. Hot pressed polycrystalline $Li_{6.4}La_3Zr_{1.4}Ta_{0.6}O_{12}$ (HP) and the Czochralski drawn single crystalline $Li_{6.5}La_3Zr_{1.5}Ta_{0.5}O_{12}$ (SC) were cut into cuboids with a diamond saw. Then two parallel sides of the samples were polished in a multi step mechanical and vibrational polishing procedure. At the University of Oslo Ag ions were implanted up to 1 µm deep into both polished sides of the sample, flipping over after implantation on one side. Two polycrystalline samples were thinned to a final thickness of around 80 µm by conventional mechanical polishing, same as for the initial surface preparation, to allow for sufficient X-Ray penetration in the Synchrotron measurements. For electrochemical experiments the implanted sides were coated with a molten LiSn alloy, containing 30 wt% of Sn.

4.3.3 Implantation Profile

According to the SRIM simulation, Figure 4.5a, an implantation depth of up to 1 µm with a concentration peak at around 630 ± 30 nm and a damage peak at around 430 ± 25 nm, can be expected. In order to visualize the changes from the implantation virtual dark field imaging applied to a SPED measurement of an implanted polycrystalline LLZTO sample as shown in Figure 4.5b. An amorphous region from the ion implantation is visible in the top 650 nm. However, the material showed itself to be rather beam sensitive, being also amorphized by the stationary electron beam, denying atomic resolution, reliable detection of the Ag with EDX and EELS and determination of strain in the material from the diffraction patterns. Since the depth of the amorphized region, correlates well with the SRIM simulation, atom probe tomography was performed at the peak implantation depth at 700 nm as well as after the peak damage depth of 1300 nm. The noise level of the mass spectra under the chosen analysis conditions does, however, not allow to detect the low Ag content. Through the use of FIB-SEM with correlative TOF-SIMS the presence of Ag ions in the implanted region was confirmed. Depth dependent CS nano XRD, Figure 4.5c, also depicts an amorphization in the top 700 nm as indicated by the broad diffuse scattering peak centered around 18 degrees 2Θ. A depth resolved stress profile was calculated, showing a compressive stress peak up to -700 MPa at a depth of 850 nm below the surface, shown in Figure 4.5 d. Based on this stress value and previously established methodology the flaw size of a dendrite which can be deflected and if the implanted depth is sufficient for deflection can be determined. For our values this behaviour should occur for the growing dendrite.

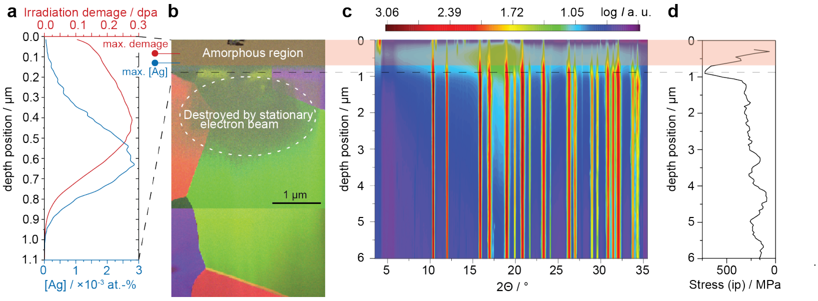

Figure 4.5: a) SRIM simulation of the damage and Ag ion distribution b) SPED composite dark field image of an implanted hot pressed $Li_{6.4}Ta_{0.6}La_3Zr_{1.4}O_{12}$ polycrystal an amorphous layer 650 nm deep is clearly visible c) Compilation of cross-sectional nano X-ray diffraction patterns of the implanted polycrystalline LLZTO sample. The implanted region is shaded in orange. An amorphous region can be seen, starting from the surface down to a depth of 700 nm. d) Depth dependent compressive in plane stress

4.3.4 Crack Deflection

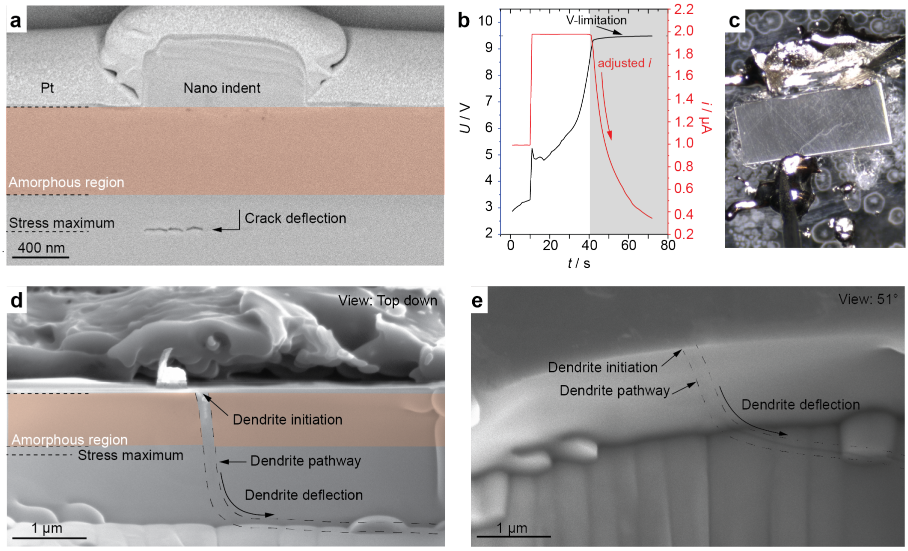

Figure 4.6: a) SEM image of a mechanically induced crack by nano indentation in Ag implanted LLZTO. b) Voltage profiles during the short circuiting measurement, spliced together.(c) Optical microsope image of the thinned hot pressed LLZTO during the short-circuit measurement. (d,e) SEM image of an electrochemically induced crack in Ag implanted LLZTO. Top view (d) and 51° angled view (e) implanted region shaded in orange.

An implanted single crystalline sample was probed via nanoindentation followed by FIB SEM to investigate the crack propagation. As can be seen in Figure 4.6a the fracture runs parallel to the surface at the stress maximum, determined beforehand. An amorphized region is again visible. There are no cracks connecting the indent with the fracture below, which should be present if it was a radial fracture. To test if a similar deflection occurs for dendrites, they were induced by applying current well above the CCD to a thinned implanted sample with Li metal on both sides until device limitations were reached, due to reducing contact area from lithium stripping. The voltage curve and the setup is shown in Figure 4.6b-c. Subsequent FIB-SEM cuts show the path of the dendrite. In the top down view in Figure 4.6d the initial crack begins to kink at around 700 nm and is fully deflected at 1.5 µm, the path is highlighted with dashed lines surrounding it. In the angled view in Figure 4.6e, the fully deflected dendrite is visible. The later deflection is attributed to locally differing stress, as the value gained from XRD is averaged over the width.

Impedance spectroscopy was performed to assess the influence of the amorphized layer on the ionic conductivity of the LLZTO, which is reduced by four orders of magnitude compared to the bulk conductivity. Annealing procedures could be employed to regain crystallinity, while they can also affect the stress zone in the material. Therefore this was not further pursued in this work. To conclude the deflection of dendrites via an ion implanted compressive stress zone is shown and can be a viable strategy for dendrite free solid state electrolytes but further work will be needed on the annealing procedures to regain performance.

4.4 Paper III: Dislocations and dendrite branching

4.4.1 Overview

The third paper investigated the immediate environment of a dendrite in LLZTO with Dark field X-ray Microscopy to gain more information on how dendrites can penetrate the solid electrolyte. The DFXM measurement revealed dislocations near the dendrite tip, with one of them pinning the tip. The effect of those dislocations is discussed and through correlation with the dendrite shape a mechanism for the influence on the dendrite path is established.

4.4.2 Sample preparation

Czochralski drawn single crystalline $Li_{6.5}La_3Zr_{1.5}Ta_{0.5}O_{12}$ was oriented with Laue diffraction to a known crystal orientation. The single crystal was cut into cuboids with the known orientation pointing out of the large surface and two parallel sides of the samples were polished in a multi step mechanical polishing procedure. The samples were thinned to a final thickness of around 100 μm by conventional mechanical polishing, same as in Paper I and II, to allow for sufficient X-Ray penetration in the Synchrotron measurements. The polished sides were coated with a molten LiSn alloy, containing 30 wt% of Sn. A current density of 1 mA/cm^2, increased to 5 mA/cm^2 was applied to grow a dendrite partway into the solid electrolyte.

4.4.3 DFXM measurement

The first DFXM images were taken in the near-field configuration. 17 keV photons were selected by a Si monochromator and the beam was focused vertically using a Compound Refractive Lens. A single plane through the crystal was illuminated by the horizontal line beam, defining the observation plane of the microscope. The results of the near field rocking curve measurement can be seen in Figure 4.7. The shape of the dendrite from the optical microscopy image in Figure 4.7a corresponds well to the measurements in Figure 4.7b. From the orientation spread in Figure 4.7c it shows that the orientation of the dendrite, or at least from the main crack in blue, differs from the surrounding matrix. The full width half maximum map in Figure 4.7d confirms that the orientation spread around the dendrite is significantly higher than the matrix.

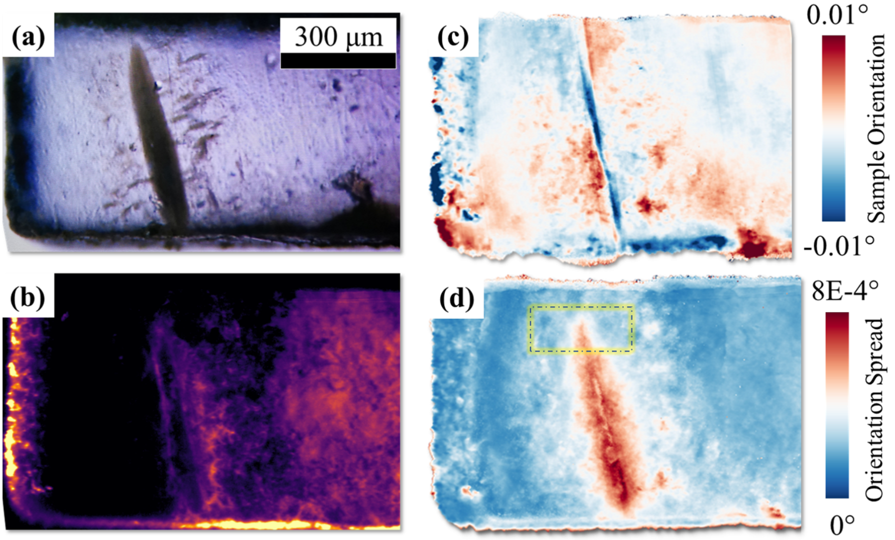

Figure 4.7: a) optical image of the LLZTO with the dendrite visible. b) background corrected raw image from the nearfield projection. c) generated center of mass map of the rocking curve showing the local orientation distribution. d)generated full width half maximum map of the rocking curve indicating the high angular spread of the dendrite. The yellow box marks the field of view for the far field measurement

After the alignment in the near-field was completed, the near-field camera was removed, and the image was magnified by an X-ray objective lens. The Compound Refractive Lens was aligned 269 mm from the sample along the diffracted beam using a far-field detector. Three scan types were conducted in the far-field: rocking scans, mosaicity scans, and axial strain scans. Rocking scans involved a tilt angle ϕ range of $\Delta\phi = 0.15°$ in 25 steps (0.006° per step) to map displacement gradient tensor field components. Mosaicity scans and axial strain scans assessed distortions along orthogonal tilts χ and ϕ, and the 2θ axis, respectively.

Voxels were associated with (HKL) pole figure subsets, allowing the generation of Center of Mass (COM) maps for voxel-level (HKL) orientation. Finally, axial strain scans quantified residual strain by scanning the 2θ axis ($\Delta 2\theta = 0.01°$) and were reconstructed into the COM maps. The results are shown in Figure 4.8. The COM maps in Figure 4.8a, for the rocking tilt, and Figure 4.8b, for the rolling tilt show an inhomogeneous orientation around the dendrite, with it acting like a boundary between the different spreads. Furthermore isolated dislocations can be seen, recognizable from their strain field. One is pinning the dendrite tip and is marked with a yellow arrow. Two more can be found to the side of the dendrite, marked with red arrows and it is plausible taking the dimensions of the dendrite into account, that they are connected to the sideways branching part of the dendrite.

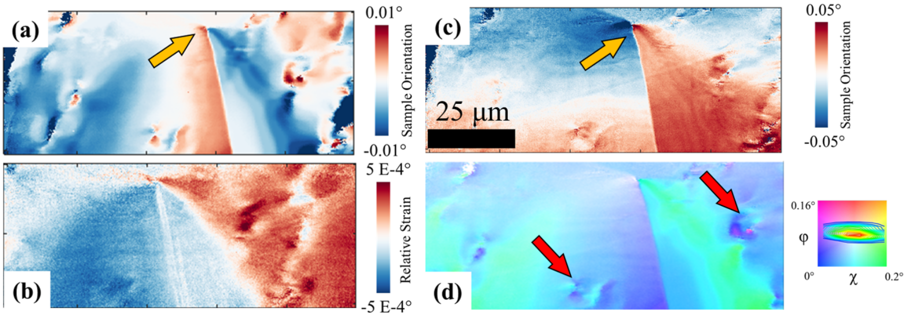

Figure 4.8: a) Far field center of mass map of the rocking tilt. b) Strain map. c) Far field center of mass map of the rolling tilt. d) Mosaicity map of the two sample tilts with the color key on the right showing the intensity.

Taking into account the typically low dislocation density of single crystalline ceramics, which can be as low as 10e6 m^{-2}, it is highly unlikely that the dislocations appear randomly in the surrounding of the dendrite. Assuming that they are connected it is also not expected that the dislocations move ahead of the dendrite as their speed is much slower. The growth speed of the dendrite, at the current densities applied here, is in the range of ~50 μm/s, whereas the speed of dislocations in ceramic is in the range of nm/s up to µm/s at room temperature. It is feasible for the dislocations to be nucleated by the stress of the growing dendrite, which can reach up to GPa levels. Reported values for dislocation nucleation in garnets at high temperatures, around 1000°C, are in the GPa range, though recent deformation tests for single crystalline LLZTO only needed 100 MPa at 1000°C. The necessary stresses at room temperature are likely higher but could still be in range. Those dislocations could then pose a mechanical weakness in the material and enable a direction for the fracture to continue on or to branch out. This mechanism of stress generated by the dendrite, nucleating dislocations where the fracture can continue, is briefly summarized in Figure 4.9. In order to confirm this an operando DFXM measurement would be necessary to determine if the dendrite nucleates dislocations and continues along their direction. .

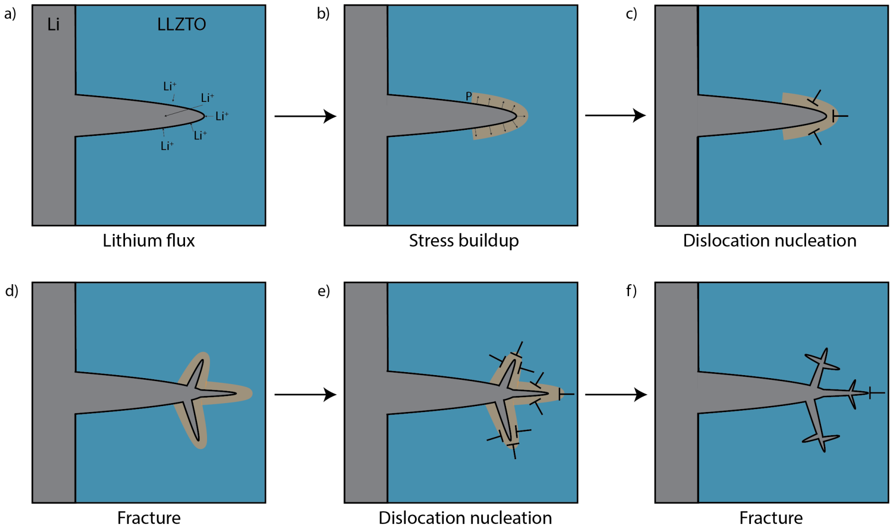

Figure 4.9: Proposed mechanism for the dislocation nucleation and fracture in LLZTO. a) high current is applied causing increased Li^+ flux towards a lithium filled flaw, based on Porz et al. b) the filled flaw exerts pressure on the LLZTO and causes the stress (zone drawn in orange) to increase. c) the high stress causes dislocations to nucleate. d) fracturing of the LLZTO and the crack fills with lithium. Note here that the precise order and timing of the events is not known. The stress zone adapts to the new cracks e) new dislocations nucleate in the stressed zone. f) cracks grow further until the current is switched off, extinguishing almost all dislocations

Next to paving the way for dendrites, dislocations could also be used to stop them in their tracks. By increasing the dislocation density the fracture toughness of the material can be heightened by allowing plastic deformation as a competing mechanism to fracture. For sintered ceramics this could be achieved via flash sintering or blacklight sintering to reduce the time for diffusion to occur at elevated temperatures.

To conclude dislocations in the vicinity of a dendrite were detected for the first time in LLZTO. They are likely to be connected to the growing dendrite and could offer them branching paths, though further experiments are necessary to confirm this. Increasing the amount of dislocations could diminish dendrite growth by increasing the fracture toughness of the material.

5

Overview and outlook

This work has encompassed multiple aspects of lithium dendrites in solid electrolytes, from the localized effect of the dendrite on the surrounding material, to locally stressing the material via implanted ions and to investigating the influence of the charging protocol on the dendrite growth and the mechanism behind it. The goal was to get more insight into dendrite growth in solid electrolytes and to formulate mitigation strategies to increase the lifetime of future solid state Li ion batteries. This chapter presents the conclusions of each part and where future steps could be taken.

Literature for electrochemical metal deposition and for lithium ion batteries, which could be seen as just a special case of metal deposition where certain degrees of freedom are removed, already show that using pulsed current can lead to a denser deposited layer.[29] This translates to an extended lifetime for lithium ion batteries as the denser, more homogeneous, layer means a reduced likelihood of dendrite growth. Paper I replicated the method onto solid electrolytes, though the focus is moved from the dense layer deposition to the propensity of dendrite growth, as that issue plagues solid electrolytes quite a bit. While no improvement is shown for single crystalline LLZTO, dense, polycrystalline LLZTO showed an increase in the critical current density and a reduction in the growth rate of the dendrite. As a purely mechanical failure mechanism is not sufficient to explain why this improvement is only occurring for the polycrystals the local lithium activity was added as an additional factor contributing to fracture. The time to reach a critical activity causing failure is dependent on the flaw size, which for single crystals is smaller than for polycrystals, and thus would require faster current pulses to mitigate. Synchrotron measurements detecting the local stress at the tip of a dendrite show that it decays based on a diffusion like process over time, giving further credence to this mechanism. Though a significant performance improvement is shown, the experiments were limited to symmetric Li-LLZTO-Li cells, and full cell tests would likely be needed to confirm similar improvements before it is implemented in actual solid state batteries. The method of pulse plating has seen industry interest and there is already a patent filed on pulse plating by Quantumscape, an American manufacturer of solid state lithium metal batteries.[157]

In Paper II Ag ions were implanted into the top surface layer of LLZTO, up to 1 µm deep, causing a compressive stress of up to -750 MPa. This residual stress causes mechanically induced cracks, as well as dendrites to deflect parallel to the surface. The beam damage from the implantation amorphizes the top 650 nm, which causes a decrease in the ionic conductivity of four orders of magnitude for this layer. Locating the implanted Ag ions was attempted via TEM and APT, but the high beam sensitivity denied EDX and EELS results from TEM and the concentration was too low for APT to detect the Ag reliably. A qualitative detection of the Ag was managed using TOF-SIMS. This work serves as a proof of concept, that dendrite growth can be inhibited through compressive stress caused by implanted ions. In literature it was already speculated that compressive stress in the soid electrolyte can stop dendrites and in mechnically stressed LLZTO a similar deflection was already shown.[34,35] However the decrease in the ionic conductivity from the amorphisation is something that would need to be adresses, as otherwise the internal resistance of the battery will be a significant power drain. This can be achieved in keeping the implantation depth low and therefore the amorphous layer small as well. Though this runs the risk of encountering surface effects during implantation and defects extending past the implanted layer diminishing the effect on dendrite growth. Another approach is to anneal the solid electrolyte after ion implantation though research into the correct parameters, which are annealing time and temperature, to recrystallize the amorphous zone while keeping the diffusion of the implanted ions and the effect on the compressive stress to a minimum, will be necessary. Once these parameters are known this technique can be scaled up to industrial processes, as is already the case in the semiconductor industry.

The last part of this work observed the environment next to a dendrite tip in LLZTO with DFXM. Through this method dislocations could be observed for the first time near a dendrite tip in LLZTO. Due to the typically low dislocation density in ceramics and the near vicinity of the dislocations to the tip, they are likely to be connected and not just products of chance. Dislocations are therefore an additional parameter to be kept in mind when describing the fracture of LLZTO by a dendrite. A preliminary mechanism how it could occur is established and possible dendrite mitigation using dislocations are proposed, though operando DFXM measurements are necessary to confirm the mechanism. The other method typically used to investigate dislocations, TEM, needs a thin FIB lamella created by removal of material. Therefore either the dislocation density in the material needs to be high enough or the exact location where dislocations are expected needs to be known. Following from our results the near tip region of a dendrite is a good place to start looking. Though it has to be said that even finding the tip of a dendrite in a solid electrolyte is a non trivial problem.

The problem of dendrite growth itself will continue to accompany lithium ion batteries further, as it is in part an optimization issue. Just looking at LLZO this can range from dopants, to surface condition and applied current programme. These challenges are not necesarily the same for other solid electrolytes. Once a set goal of charge rate or lifecycles is reached it is often enough to move the bar slightly higher, like Icarus reaching for the sun, for dendrites to rear their head again. So this work concludes in front of this seemingly sysiphean task hopefully having singed some of the hydras heads that are lithum dendrites but with numerous remaining for the torch to be carried on for this Odyssey in pursuit of knowledge.

Bibliography

[1] W. M. O. (WMO), “Weather-related disasters increase over past 50 years, causing more damage but fewer deaths,” 2021.

[2] N. J. Abram, B. J. Henley, A. Sen Gupta, T. J. Lippmann, H. Clarke, A. J. Dowdy, J. J. Sharples, R. H. Nolan, T. Zhang, M. J. Wooster, *et al.*, “Connections of climate change and variability to large and extreme forest fires in southeast australia,” *Communications Earth & Environment*, vol. 2, no. 1, p. 8, 2021.

[3] M. M. Boer, V. Resco de Dios, and R. A. Bradstock, “Unprecedented burn area of australian mega forest fires,” *Nature Climate Change*, vol. 10, no. 3, pp. 171–172, 2020.

[4] M. R. M. AM, M. C. Carnegie, G. de Brouwer, M. S. de Castro, M. J. Clough, M. M. Dixon, M. S. Fernando, M. M. McDonald, M. M. M. AC, M. G. P. AO, *et al.*, “Royal commission into national natural disaster arrangements locked bag 2000 manuka act 2603 rcnda. enquiries@ royalcommission. gov. au,” 2020.

[5] D. H., K. Raghavan, J. Renwick, P. A. R.P. Allan, R. C.-M. M. Barlow, T. G. A. Cherchi, J. Gergis, A. K. D. Jiang, W. P. Mba, D. Rosenfeld, J. Tierney, and O. Zolina, “2021: Water cycle changes. in climate change 2021: The physical science basis.,” *Contribution of Working Group I to the Sixth Assessment Report of the Intergovernmental Panel on Climate Change*, 2021.

[6] P. Kishore, G. Basha, M. Venkat Ratnam, A. AghaKouchak, Q. Sun, I. Velicogna, and T. Ouarda, “Anthropogenic influence on the changing risk of heat waves over india,” *Scientific reports*, vol. 12, no. 1, p. 3337, 2022.

[7] R. R., A. Ruane, R. Vautard, E. C. N. Arnell, F. Cruz, S. Dessai, A. Islam, M. Rahimi, D. R. Carrascal, J. Sillmann, M. Sylla, C. Tebaldi, W. Wang, and R. Zaaboul, "2021: Climate change information for regionalimpact and for risk assessment. in climate change 2021: The physical science basis.," *Contribution of Working Group I to the Sixth Assessment Report of the Intergovernmental Panel on Climate Change*, 2021.

[8] J. P., S. K. Ribeiro, P. Newman, S. Dhar, O. Diemuodeke, T. Kajino, D. Lee, S. Nugroho, X. Ou, A. H. Strømman, and J. Whitehead, "2022: Transport. in ipcc, 2022: Climate change 2022: Mitigation of climate change.," *Contribution of Working Group III to the Sixth Assessment Report of the Intergovernmental Panel on Climate Change*, 2022.

[9] E. C. P. Release, "Zero emission vehicles: first 'fit for 55' deal will end the sale of new co2 emitting cars in europe by 2035," 2022.

[10] IEA, "Global co2 emissions from transport by sub-sector in the net zero scenario, 2000-2030," 2023.

[11] C. Grosjean, P. H. Miranda, M. Perrin, and P. Poggi, "Assessment of world lithium resources and consequences of their geographic distribution on the expected development of the electric vehicle industry," *Renewable and Sustainable Energy Reviews*, vol. 16, no. 3, pp. 1735–1744, 2012.

[12] R. B. Kaunda, "Potential environmental impacts of lithium mining," *Journal of energy & natural resources law*, vol. 38, no. 3, pp. 237–244, 2020.

[13] K. Chayambuka, G. Mulder, D. L. Danilov, and P. H. Notten, "From li-ion batteries toward na-ion chemistries: challenges and opportunities," *Advanced energy materials*, vol. 10, no. 38, p. 2001310, 2020.

[14] A. Ponrouch, J. Bitenc, R. Dominko, N. Lindahl, P. Johansson, and M. R. Palacín, "Multivalent rechargeable batteries," *Energy Storage Materials*, vol. 20, pp. 253–262, 2019.

[15] K. M. Tan, V. K. Ramachandaramurthy, and J. Y. Yong, "Integration of electric vehicles in smart grid: A review on vehicle to grid technologies and optimization techniques," *Renewable and Sustainable Energy Reviews*, vol. 53, pp. 720–732, 2016.

[16] L. A. Cuartas, A. P. M. d. A. Cunha, J. A. Alves, L. M. P. Parra, K. Deusdará-Leal, L. C. O. Costa, R. D. Molina, D. Amore, E. Broedel, M. E. Seluchi, *et al.*, "Recent hydrological droughts in brazil and their impact on hydropower generation," *Water*, vol. 14, no. 4, p. 601, 2022.

[17] A. Wasti, P. Ray, S. Wi, C. Folch, M. Ubierna, and P. Karki, "Climate change and the hydropower sector: A global review," *Wiley Interdisciplinary Reviews: Climate Change*, vol. 13, no. 2, p. e757, 2022.

[18] M. A. DeLuchi, “Hydrogen vehicles: an evaluation of fuel storage, performance, safety, environmental impacts, and cost,” *International Journal of Hydrogen Energy*, vol. 14, no. 2, pp. 81–130, 1989.

[19] F. Larsson, P. Andersson, P. Blomqvist, A. Lorén, and B.-E. Mellander, “Characteristics of lithium-ion batteries during fire tests,” *Journal of Power Sources*, vol. 271, pp. 414–420, 2014.

[20] F. Larsson, P. Andersson, P. Blomqvist, and B.-E. Mellander, “Toxic fluoride gas emissions from lithium-ion battery fires,” *Scientific reports*, vol. 7, no. 1, p. 10018, 2017.

[21] P. Sun, R. Bisschop, H. Niu, and X. Huang, “A review of battery fires in electric vehicles,” *Fire technology*, vol. 56, pp. 1361–1410, 2020.

[22] N. Universal, “Tesla car battery 'spontaneously' catches fire on california freeway, requiring 6,000 gallons of water to put it out,” 2023.

[23] E. Peled, “The electrochemical behavior of alkali and alkaline earth metals in nonaqueous battery systems—the solid electrolyte interphase model,” *Journal of The Electrochemical Society*, vol. 126, no. 12, p. 2047, 1979.

[24] D. Ren, X. Feng, L. Lu, M. Ouyang, S. Zheng, J. Li, and X. He, “An electrochemical-thermal coupled overcharge-to-thermal-runaway model for lithium ion battery,” *Journal of power sources*, vol. 364, pp. 328–340, 2017.

[25] G. Berdichevsky, K. Kelty, J. Straubel, and E. Toomre, “The tesla roadster battery system,” *Tesla Motors*, vol. 1, no. 5, pp. 1–5, 2006.

[26] M. J. Loveridge, G. Remy, N. Kourra, R. Genieser, A. Barai, M. J. Lain, Y. Guo, M. Amor-Segan, M. A. Williams, T. Amietszajew, *et al.*, “Looking deeper into the galaxy (note 7),” *Batteries*, vol. 4, no. 1, p. 3, 2018.

[27] M. V. Reddy, A. Mauger, C. M. Julien, A. Paolella, and K. Zaghib, “Brief history of early lithium-battery development,” *Materials*, vol. 13, no. 8, p. 1884, 2020.

[28] C. Monroe and J. Newman, “The impact of elastic deformation on deposition kinetics at lithium/polymer interfaces,” *Journal of The Electrochemical Society*, vol. 152, no. 2, p. A396, 2005.

[29] G. García, S. Dieckhöfer, W. Schuhmann, and E. Ventosa, “Exceeding 6500 cycles for lifepo 4/li metal batteries through understanding pulsed charging protocols,” *Journal of Materials Chemistry A*, vol. 6, no. 11, pp. 4746–4751, 2018.

[30] X. Sun, X. Zhang, Q. Ma, X. Guan, W. Wang, and J. Luo, “Revisiting the electroplating process for lithium-metal anodes for lithium-metal batteries,” *Angewandte Chemie International Edition*, vol. 59, no. 17, pp. 6665–6674, 2020.

[31] H. Yang, E. O. Fey, B. D. Trimm, N. Dimitrov, and M. S. Whittingham, "Effects of pulse plating on lithium electrodeposition, morphology and cycling efficiency," *Journal of Power Sources*, vol. 272, pp. 900–908, 2014.

[32] H. Cheh, "Electrodeposition of gold by pulsed current," *Journal of the Electrochemical Society*, vol. 118, no. 4, p. 551, 1971.

[33] A. Aryanfar, D. Brooks, B. V. Merinov, W. A. Goddard III, A. J. Colussi, and M. R. Hoffmann, "Dynamics of lithium dendrite growth and inhibition: pulse charging experiments and monte carlo calculations," *The journal of physical chemistry letters*, vol. 5, no. 10, pp. 1721–1726, 2014.

[34] Y. Qi, C. Ban, and S. J. Harris, "A new general paradigm for understanding and preventing li metal penetration through solid electrolytes," *Joule*, vol. 4, no. 12, pp. 2599–2608, 2020.

[35] C. D. Fincher, C. E. Athanasiou, C. Gilgenbach, M. Wang, B. W. Sheldon, W. C. Carter, and Y.-M. Chiang, "Controlling dendrite propagation in solid-state batteries with engineered stress," *Joule*, vol. 6, no. 12, pp. 2794–2809, 2022.

[36] V. Gurarie, P. Otsuka, D. Jamieson, and S. Prawer, "Crack-arresting compression layers produced by ion implantation," *Nuclear Instruments and Methods in Physics Research Section B: Beam Interactions with Materials and Atoms*, vol. 242, no. 1-2, pp. 421–423, 2006.

[37] X. Yao, E. Olsson, M. Wang, J. Wang, Q. Cai, N. Peng, R. Webb, and Y. Zhao, "Xenon ion implantation induced surface compressive stress for preventing dendrite penetration in solid-state electrolytes," *Small*, vol. 18, no. 23, p. 2108124, 2022.

[38] H. Simons, A. C. Jakobsen, S. R. Ahl, C. Detlefs, and H. F. Poulsen, "Multiscale 3d characterization with dark-field x-ray microscopy," *Mrs Bulletin*, vol. 41, no. 6, pp. 454–459, 2016.

[39] A. Jakobsen, H. Simons, W. Ludwig, C. Yildirim, H. Leemreize, L. Porz, C. Detlefs, and H. Poulsen, "Mapping of individual dislocations with dark-field x-ray microscopy," *Journal of Applied Crystallography*, vol. 52, no. 1, pp. 122–132, 2019.

[40] C. Yildirim, P. Cook, C. Detlefs, H. Simons, and H. F. Poulsen, "Probing nanoscale structure and strain by dark-field x-ray microscopy," *MRS Bulletin*, vol. 45, no. 4, pp. 277–282, 2020.

[41] B. Markovsky, M. D. Levi, and D. Aurbach, "The basic electroanalytical behavior of practical graphite–lithium intercalation electrodes," *Electrochimica acta*, vol. 43, no. 16-17, pp. 2287–2304, 1998.

[42] K. Mizushima, P. Jones, P. Wiseman, and J. B. Goodenough, "Lixcoo2 (0< x<-1): A new cathode material for batteries of high energy density," *Materials Research Bulletin*, vol. 15, no. 6, pp. 783–789, 1980.

[43] Y. Wu, C. Jiang, C. Wan, and E. Tsuchida, "Effects of catalytic oxidation on the electrochemical performance of common natural graphite as an anode material for lithium ion batteries," *Electrochemistry Communications*, vol. 2, no. 4, pp. 272–275, 2000.

[44] L. P. L. M. Rabou and A. Roskam, "Cycle-life improvement of lilicoo2 batteries," *Journal of power sources*, vol. 54, no. 2, pp. 316–318, 1995.

[45] Z. Chen and J. Dahn, "Methods to obtain excellent capacity retention in licoo2 cycled to 4.5 v," *Electrochimica Acta*, vol. 49, no. 7, pp. 1079–1090, 2004.

[46] J. Kasnatscheew, T. Placke, B. Streipert, S. Rothermel, R. Wagner, P. Meister, I. C. Laskovic, and M. Winter, "A tutorial into practical capacity and mass balancing of lithium ion batteries," *Journal of the electrochemical society*, vol. 164, no. 12, p. A2479, 2017.

[47] C. Wang, A. J. Appleby, and F. E. Little, "Charge–discharge stability of graphite anodes for lithium-ion batteries," *Journal of Electroanalytical Chemistry*, vol. 497, no. 1-2, pp. 33–46, 2001.

[48] P. Verma, P. Maire, and P. Novák, "A review of the features and analyses of the solid electrolyte interphase in li-ion batteries," *Electrochimica Acta*, vol. 55, no. 22, pp. 6332–6341, 2010.

[49] T. Waldmann, B.-I. Hogg, and M. Wohlfahrt-Mehrens, "Li plating as unwanted side reaction in commercial li-ion cells–a review," *Journal of Power Sources*, vol. 384, pp. 107–124, 2018.

[50] K.-H. Chen, K. N. Wood, E. Kazyak, W. S. LePage, A. L. Davis, A. J. Sanchez, and N. P. Dasgupta, "Dead lithium: mass transport effects on voltage, capacity, and failure of lithium metal anodes," *Journal of Materials Chemistry A*, vol. 5, no. 23, pp. 11671–11681, 2017.

[51] O. Crowther and A. C. West, "Effect of electrolyte composition on lithium dendrite growth," *Journal of the Electrochemical Society*, vol. 155, no. 11, p. A806, 2008.

[52] M. S. Whittingham, "Electrical energy storage and intercalation chemistry," *Science*, vol. 192, no. 4244, pp. 1126–1127, 1976.

[53] N. N. P. O. A. 2023, "The nobel prize in chemistry 2019.," 2019.

[54] J. Besenhard and G. Eichinger, "High energy density lithium cells: Part i. electrolytes and anodes," *Journal of Electroanalytical Chemistry and Interfacial Electrochemistry*, vol. 68, no. 1, pp. 1–18, 1976.

[55] A. Mauger, C. M. Julien, J. B. Goodenough, and K. Zaghib, "Tribute to michel armand: from rocking chair–li-ion to solid-state lithium batteries," *Journal of The Electrochemical Society*, vol. 167, no. 7, p. 070507, 2019.

[56] M. B. Armand and M. Duclot, "Electrochemical generators for producing current and new materials for their manufacture," Dec. 1 1981. US Patent 4,303,748.

[57] M. Armand, P. Axmann, D. Bresser, M. Copley, K. Edström, C. Ekberg, D. Guyomard, B. Lestriez, P. Novák, M. Petranikova, *et al.*, "Lithium-ion batteries–current state of the art and anticipated developments," *Journal of Power Sources*, vol. 479, p. 228708, 2020.

[58] C. Sandhya, B. John, and C. Gouri, “Lithium titanate as anode material for lithium-ion cells: a review,” *Ionics*, vol. 20, pp. 601–620, 2014.

[59] D. Billaud, E. McRae, and A. Hérold, “Synthesis and electrical resistivity of lithium-pyrographite intercalation compounds (stages i, ii and iii),” *Materials Research Bulletin*, vol. 14, no. 7, pp. 857–864, 1979.

[60] Y.-J. Hao, Q.-Y. Lai, J.-Z. Lu, H.-L. Wang, Y.-D. Chen, and X.-Y. Ji, “Synthesis and characterization of spinel li4ti5o12 anode material by oxalic acid-assisted sol–gel method,” *Journal of Power Sources*, vol. 158, no. 2, pp. 1358–1364, 2006.

[61] H. Zhou *et al.*, “Two-phase transition of li-intercalation compounds in li-ion batteries,” *Materials Today*, vol. 17, no. 9, pp. 451–463, 2014.

[62] I. Leonidov, O. Leonidova, L. Perelyaeva, R. Samigullina, S. Kovyazina, and M. Patrakeev, “Structure, ionic conduction, and phase transformations in lithium titanate li 4 ti 5 o 12,” *Physics of the Solid State*, vol. 45, pp. 2183–2188, 2003.

[63] K. Zaghib, M. Simoneau, M. Armand, and M. Gauthier, “Electrochemical study of li4ti5o12 as negative electrode for li-ion polymer rechargeable batteries,” *Journal of Power Sources*, vol. 81, pp. 300–305, 1999.

[64] Y. Jin, B. Zhu, Z. Lu, N. Liu, and J. Zhu, “Challenges and recent progress in the development of si anodes for lithium-ion battery,” *Advanced Energy Materials*, vol. 7, no. 23, p. 1700715, 2017.

[65] S.-J. Lee, J.-K. Lee, S.-H. Chung, H.-Y. Lee, S.-M. Lee, and H.-K. Baik, “Stress effect on cycle properties of the silicon thin-film anode,” *Journal of power sources*, vol. 97, pp. 191–193, 2001.

[66] H. Wu and Y. Cui, “Designing nanostructured si anodes for high energy lithium ion batteries,” *Nano today*, vol. 7, no. 5, pp. 414–429, 2012.

[67] M. A. Rahman, G. Song, A. I. Bhatt, Y. C. Wong, and C. Wen, “Nanostructured silicon anodes for high-performance lithium-ion batteries,” *Advanced Functional Materials*, vol. 26, no. 5, pp. 647–678, 2016.

[68] Z. Liu, Q. Yu, Y. Zhao, R. He, M. Xu, S. Feng, S. Li, L. Zhou, and L. Mai, “Silicon oxides: a promising family of anode materials for lithium-ion batteries,” *Chemical Society Reviews*, vol. 48, no. 1, pp. 285–309, 2019.

[69] S. Chae, S.-H. Choi, N. Kim, J. Sung, and J. Cho, “Integration of graphite and silicon anodes for the commercialization of high-energy lithium-ion batteries,” *Angewandte Chemie International Edition*, vol. 59, no. 1, pp. 110–135, 2020.

[70] H. F. Andersen, C. E. L. Foss, J. Voje, R. Tronstad, T. Mokkelbost, P. E. Vullum, A. Ulvestad, M. Kirkengen, and J. P. Mæhlen, “Silicon-carbon composite anodes from industrial battery grade silicon,” *Scientific reports*, vol. 9, no. 1, p. 14814, 2019.

[71] S. Goriparti, E. Miele, F. De Angelis, E. Di Fabrizio, R. P. Zaccaria, and C. Capiglia, "Review on recent progress of nanostructured anode materials for li-ion batteries," *Journal of power sources*, vol. 257, pp. 421–443, 2014.

[72] L. Zhang, H. B. Wu, and X. W. Lou, "Iron-oxide-based advanced anode materials for lithium-ion batteries," *Advanced Energy Materials*, vol. 4, no. 4, p. 1300958, 2014.

[73] J. Cabana, L. Monconduit, D. Larcher, and M. R. Palacin, "Beyond intercalation-based li-ion batteries: the state of the art and challenges of electrode materials reacting through conversion reactions," *Advanced materials*, vol. 22, no. 35, pp. E170–E192, 2010.

[74] K. N. Wood, E. Kazyak, A. F. Chadwick, K.-H. Chen, J.-G. Zhang, K. Thornton, and N. P. Dasgupta, "Dendrites and pits: Untangling the complex behavior of lithium metal anodes through operando video microscopy," *ACS central science*, vol. 2, no. 11, pp. 790–801, 2016.

[75] W. Xu, J. Wang, F. Ding, X. Chen, E. Nasybulin, Y. Zhang, and J.-G. Zhang, "Lithium metal anodes for rechargeable batteries," *Energy & Environmental Science*, vol. 7, no. 2, pp. 513–537, 2014.

[76] R. Guo, L. Lu, M. Ouyang, and X. Feng, "Mechanism of the entire overdischarge process and overdischarge-induced internal short circuit in lithium-ion batteries," *Scientific reports*, vol. 6, no. 1, p. 30248, 2016.

[77] B. K. Sovacool, "The precarious political economy of cobalt: Balancing prosperity, poverty, and brutality in artisanal and industrial mining in the democratic republic of the congo," *The Extractive Industries and Society*, vol. 6, no. 3, pp. 915–939, 2019.

[78] Y. Zhang, H. Xie, H. Jin, Q. Zhang, Y. Li, X. Li, K. Li, and C. Bao, "Research status of spinel limn2o4 cathode materials for lithium ion batteries," in *IOP Conference Series: Earth and Environmental Science*, vol. 603, p. 012051, IOP Publishing, 2020.

[79] E. Kelder, J. Thomas, *et al.*, "Neutron diffraction study of stoichiometric spinel li 1+ x mn 2–x o 4 showing octahedral 16 c-site li-occupation," *Journal of Materials Chemistry*, vol. 9, no. 2, pp. 427–429, 1999.

[80] R. Gummow, A. De Kock, and M. Thackeray, "Improved capacity retention in rechargeable 4 v lithium/lithium-manganese oxide (spinel) cells," *Solid State Ionics*, vol. 69, no. 1, pp. 59–67, 1994.

[81] S. Zhou, H. Han, J. Nie, M. Armand, Z. Zhou, and X. Huang, "Improving the high-temperature resilience of limn2o4 based batteries: Lifnfsi an effective salt," *Journal of The Electrochemical Society*, vol. 159, no. 8, p. A1158, 2012.

[82] Y. Shao-Horn, S. Hackney, A. Kahaian, K. Kepler, E. Skinner, J. Vaughey, and M. Thackeray, "Structural fatigue in spinel electrodes in li/lix [mn2] o4 cells," *Journal of power sources*, vol. 81, pp. 496–499, 1999.

[83] H. Arai, S. Okada, Y. Sakurai, and J.-i. Yamaki, “Reversibility of linio2 cathode,” *Solid State Ionics*, vol. 95, no. 3-4, pp. 275–282, 1997.

[84] J. Peres, C. Delmas, A. Rougier, M. Broussely, F. Perton, P. Biensan, and P. Willmann, “The relationship between the composition of lithium nickel oxide and the loss of reversibility during the first cycle,” *Journal of Physics and Chemistry of Solids*, vol. 57, no. 6-8, pp. 1057–1060, 1996.

[85] I. A. Shkrob, J. A. Gilbert, P. J. Phillips, R. Klie, R. T. Haasch, J. Bareño, and D. P. Abraham, “Chemical weathering of layered ni-rich oxide electrode materials: evidence for cation exchange,” *Journal of The Electrochemical Society*, vol. 164, no. 7, p. A1489, 2017.

[86] K. K. Lee, W. S. Yoon, K. B. Kim, K. Y. Lee, and S. T. Hong, “Characterization of lini0. 85co0. 10m0. 05o2 (m= al, fe) as a cathode material for lithium secondary batteries,” *Journal of power sources*, vol. 97, pp. 308–312, 2001.

[87] H. Liu, F. C. Strobridge, O. J. Borkiewicz, K. M. Wiaderek, K. W. Chapman, P. J. Chupas, and C. P. Grey, “Capturing metastable structures during high-rate cycling of lifepo4 nanoparticle electrodes,” *Science*, vol. 344, no. 6191, p. 1252817, 2014.

[88] A. Yamada, S.-C. Chung, and K. Hinokuma, “Optimized lifepo4 for lithium battery cathodes,” *Journal of the electrochemical society*, vol. 148, no. 3, p. A224, 2001.

[89] K. Y., O. Z., and P. M. J.M., *Lithium-Ion Batteries: Overview, Simulation, and Diagnostics (1st ed.)*. Jenny Stanford Publishing, 2019.

[90] X. Ji and L. F. Nazar, “Advances in li–s batteries,” *Journal of Materials Chemistry*, vol. 20, no. 44, pp. 9821–9826, 2010.

[91] J.-Q. Huang, Q. Zhang, H.-J. Peng, X.-Y. Liu, W.-Z. Qian, and F. Wei, “Ionic shield for polysulfides towards highly-stable lithium–sulfur batteries,” *Energy & environmental science*, vol. 7, no. 1, pp. 347–353, 2014.

[92] Y. V. Mikhaylik and J. R. Akridge, “Polysulfide shuttle study in the li/s battery system,” *Journal of the electrochemical society*, vol. 151, no. 11, p. A1969, 2004.

[93] D. Kwabi, N. Ortiz-Vitoriano, S. A. Freunberger, Y. Chen, N. Imanishi, P. G. Bruce, and Y. Shao-Horn, “Materials challenges in rechargeable lithium-air batteries,” *Mrs Bulletin*, vol. 39, no. 5, pp. 443–452, 2014.

[94] S. A. Freunberger, Y. Chen, N. E. Drewett, L. J. Hardwick, F. Bardé, and P. G. Bruce, “The lithium–oxygen battery with ether-based electrolytes,” *Angewandte Chemie International Edition*, vol. 50, no. 37, pp. 8609–8613, 2011.

[95] S. Callens, J.-F. Le Nest, A. Gandini, and M. Armand, “A novel solid polymer electrolyte: Synthesis and characterization,” *Polymer bulletin*, vol. 25, pp. 443–450, 1991.

[96] J. Kalhoff, G. G. Eshetu, D. Bresser, and S. Passerini, "Safer electrolytes for lithium-ion batteries: state of the art and perspectives," *ChemSusChem*, vol. 8, no. 13, pp. 2154–2175, 2015.

[97] S. S. Zhang, "A review on electrolyte additives for lithium-ion batteries," *Journal of Power Sources*, vol. 162, no. 2, pp. 1379–1394, 2006.

[98] C. Chen, T. Zhou, D. L. Danilov, L. Gao, S. Benning, N. Schön, S. Tardif, H. Simons, F. Hausen, T. U. Schülli, *et al.*, "Impact of dual-layer solid-electrolyte interphase inhomogeneities on early-stage defect formation in si electrodes," *Nature communications*, vol. 11, no. 1, p. 3283, 2020.

[99] P. B. Balbuena and Y. X. Wang, *Lithium-ion batteries: solid-electrolyte interphase*. World Scientific, 2004.

[100] E. S. Takeuchi and R. A. Leising, "Lithium batteries for biomedical applications," *MRS bulletin*, vol. 27, no. 8, pp. 624–627, 2002.

[101] G. Zubi, R. Dufo-López, M. Carvalho, and G. Pasaoglu, "The lithium-ion battery: State of the art and future perspectives," *Renewable and Sustainable Energy Reviews*, vol. 89, pp. 292–308, 2018.

[102] Y. Chen, Y. Kang, Y. Zhao, L. Wang, J. Liu, Y. Li, Z. Liang, X. He, X. Li, N. Tavajohi, *et al.*, "A review of lithium-ion battery safety concerns: The issues, strategies, and testing standards," *Journal of Energy Chemistry*, vol. 59, pp. 83–99, 2021.

[103] X. Feng, M. Ouyang, X. Liu, L. Lu, Y. Xia, and X. He, "Thermal runaway mechanism of lithium ion battery for electric vehicles: A review," *Energy storage materials*, vol. 10, pp. 246–267, 2018.

[104] Q. Wang, P. Ping, X. Zhao, G. Chu, J. Sun, and C. Chen, "Thermal runaway caused fire and explosion of lithium ion battery," *Journal of power sources*, vol. 208, pp. 210–224, 2012.

[105] K. I. Popov, S. S. Djokić, and B. N. Grgur, "Surface morphology of metal electrodeposits," *Fundamental aspects of electrometallurgy*, pp. 29–100, 2002.

[106] L. Yangyang, X. Xieyu, S. Matthew, K. O. O, K. V. A, B. Jun, W. Jialin, J. Xingxing, S. Zhongxiao, S. Jiangxuan, *et al.*, "Insight into the critical role of exchange current density on electrodeposition behavior of lithium metal," *Advanced Science*, vol. 8, no. 5, p. 2003301, 2021.

[107] P. Lu, C. Li, E. W. Schneider, and S. J. Harris, "Chemistry, impedance, and morphology evolution in solid electrolyte interphase films during formation in lithium ion batteries," *The Journal of Physical Chemistry C*, vol. 118, no. 2, pp. 896–903, 2014.

[108] P. C. Howlett, D. R. Macfarlane, and A. F. Hollenkamp, "A sealed optical cell for the study of lithium-electrode| electrolyte interfaces," *Journal of power sources*, vol. 114, no. 2, pp. 277–284, 2003.

[109] M. Arakawa, S.-i. Tobishima, Y. Nemoto, M. Ichimura, and J.-i. Yamaki, “Lithium electrode cycleability and morphology dependence on current density,” *Journal of power sources*, vol. 43, no. 1-3, pp. 27–35, 1993.

[110] A. Jana and R. E. García, “Lithium dendrite growth mechanisms in liquid electrolytes,” *Nano Energy*, vol. 41, pp. 552–565, 2017.

[111] M. Dollé, L. Sannier, B. Beaudoin, M. Trentin, and J.-M. Tarascon, “Live scanning electron microscope observations of dendritic growth in lithium/polymer cells,” *Electrochemical and solid-state letters*, vol. 5, no. 12, p. A286, 2002.

[112] P. Bai, J. Li, F. R. Brushett, and M. Z. Bazant, “Transition of lithium growth mechanisms in liquid electrolytes,” *Energy & Environmental Science*, vol. 9, no. 10, pp. 3221–3229, 2016.

[113] P. Shi, L. Zhang, H. Xiang, X. Liang, Y. Sun, and W. Xu, “Lithium difluorophosphate as a dendrite-suppressing additive for lithium metal batteries,” *ACS applied materials & interfaces*, vol. 10, no. 26, pp. 22201–22209, 2018.

[114] J.-S. Kim, D. W. Kim, H. T. Jung, and J. W. Choi, “Controlled lithium dendrite growth by a synergistic effect of multilayered graphene coating and an electrolyte additive,” *Chemistry of Materials*, vol. 27, no. 8, pp. 2780–2787, 2015.

[115] F. Ding, W. Xu, G. L. Graff, J. Zhang, M. L. Sushko, X. Chen, Y. Shao, M. H. Engelhard, Z. Nie, J. Xiao, *et al.*, “Dendrite-free lithium deposition via self-healing electrostatic shield mechanism,” *Journal of the American Chemical Society*, vol. 135, no. 11, pp. 4450–4456, 2013.

[116] M. J. Wang, E. Kazyak, N. P. Dasgupta, and J. Sakamoto, “Transitioning solid-state batteries from lab to market: Linking electro-chemo-mechanics with practical considerations,” *Joule*, vol. 5, no. 6, pp. 1371–1390, 2021.

[117] N. Kamaya, K. Homma, Y. Yamakawa, M. Hirayama, R. Kanno, M. Yonemura, T. Kamiyama, Y. Kato, S. Hama, K. Kawamoto, *et al.*, “A lithium superionic conductor,” *Nature materials*, vol. 10, no. 9, pp. 682–686, 2011.

[118] A. Hayashi, S. Hama, H. Morimoto, M. Tatsumisago, and T. Minami, “Preparation of li2s–p2s5 amorphous solid electrolytes by mechanical milling,” *Journal of the American Ceramic Society*, vol. 84, no. 2, pp. 477–79, 2001.

[119] H.-J. Deiseroth, S.-T. Kong, H. Eckert, J. Vannahme, C. Reiner, T. Zaiß, and M. Schlosser, “Li6ps5x: a class of crystalline li-rich solids with an unusually high li+ mobility,” *Angewandte Chemie International Edition*, vol. 47, no. 4, pp. 755–758, 2008.

[120] Y. Kato, S. Hori, T. Saito, K. Suzuki, M. Hirayama, A. Mitsui, M. Yonemura, H. Iba, and R. Kanno, “High-power all-solid-state batteries using sulfide superionic conductors,” *Nature Energy*, vol. 1, no. 4, pp. 1–7, 2016.

[121] A. L. Davis, R. Garcia-Mendez, K. N. Wood, E. Kazyak, K.-H. Chen, G. Teeter, J. Sakamoto, and N. P. Dasgupta, "Electro-chemo-mechanical evolution of sulfide solid electrolyte/li metal interfaces: operando analysis and ald interlayer effects," *Journal of Materials Chemistry A*, vol. 8, no. 13, pp. 6291–6302, 2020.

[122] F. Han, Y. Zhu, X. He, Y. Mo, and C. Wang, "Electrochemical stability of li10gep2s12 and li7la3zr2o12 solid electrolytes," *Advanced Energy Materials*, vol. 6, no. 8, p. 1501590, 2016.

[123] V. Thangadurai, S. Adams, and W. Weppner, "Crystal structure revision and identification of li+-ion migration pathways in the garnet-like li5la3m2o12 (m= nb, ta) oxides," *Chemistry of materials*, vol. 16, no. 16, pp. 2998–3006, 2004.

[124] R. Murugan, V. Thangadurai, and W. Weppner, "Fast lithium ion conduction in garnet-type li7la3zr2o12," *Angewandte Chemie International Edition*, vol. 46, no. 41, pp. 7778–7781, 2007.

[125] J. Awaka, N. Kijima, H. Hayakawa, and J. Akimoto, "Synthesis and structure analysis of tetragonal li7la3zr2o12 with the garnet-related type structure," *Journal of solid state chemistry*, vol. 182, no. 8, pp. 2046–2052, 2009.

[126] K. Momma and F. Izumi, "Vesta: a three-dimensional visualization system for electronic and structural analysis," *Journal of Applied crystallography*, vol. 41, no. 3, pp. 653–658, 2008.

[127] R. Wagner, G. J. Redhammer, D. Rettenwander, A. Senyshyn, W. Schmidt, M. Wilkening, and G. Amthauer, "Crystal structure of garnet-related li-ion conductor li7–3 x ga x la3zr2o12: fast li-ion conduction caused by a different cubic modification?," *Chemistry of materials*, vol. 28, no. 6, pp. 1861–1871, 2016.

[128] I. Kokal, M. Somer, P. Notten, and H. Hintzen, "Sol–gel synthesis and lithium ion conductivity of li7la3zr2o12 with garnet-related type structure," *Solid State Ionics*, vol. 185, no. 1, pp. 42–46, 2011.

[129] N. Bernstein, M. Johannes, and K. Hoang, "Origin of the structural phase transition in li 7 la 3 zr 2 o 12," *Physical review letters*, vol. 109, no. 20, p. 205702, 2012.

[130] A. J. Samson, K. Hofstetter, S. Bag, and V. Thangadurai, "A bird's-eye view of li-stuffed garnet-type li 7 la 3 zr 2 o 12 ceramic electrolytes for advanced all-solid-state li batteries," *Energy & Environmental Science*, vol. 12, no. 10, pp. 2957–2975, 2019.

[131] K. Santosh, R. C. Longo, K. Xiong, and K. Cho, "Point defects in garnet-type solid electrolyte (c-li7la3zr2o12) for li-ion batteries," *Solid State Ionics*, vol. 261, pp. 100–105, 2014.

[132] G. A. Novak and G. Gibbs, "The crystal chemistry of the silicate garnets," *American Mineralogist: Journal of Earth and Planetary Materials*, vol. 56, no. 5-6, pp. 791–825, 1971.

[133] A. Kuhn, S. Narayanan, L. Spencer, G. Goward, V. Thangadurai, and M. Wilkening, "Li self-diffusion in garnet-type li 7 la 3 zr 2 o 12 as probed directly by diffusion-induced li 7 spin-lattice relaxation nmr spectroscopy," *Physical Review B*, vol. 83, no. 9, p. 094302, 2011.

[134] K. Meier, T. Laino, and A. Curioni, “Solid-state electrolytes: revealing the mechanisms of li-ion conduction in tetragonal and cubic llzo by first-principles calculations,” *The Journal of Physical Chemistry C*, vol. 118, no. 13, pp. 6668–6679, 2014.

[135] T. Thompson, S. Yu, L. Williams, R. D. Schmidt, R. Garcia-Mendez, J. Wolfenstine, J. L. Allen, E. Kioupakis, D. J. Siegel, and J. Sakamoto, “Electrochemical window of the li-ion solid electrolyte li7la3zr2o12,” *ACS Energy Letters*, vol. 2, no. 2, pp. 462–468, 2017.

[136] W. D. Richards, L. J. Miara, Y. Wang, J. C. Kim, and G. Ceder, “Interface stability in solid-state batteries,” *Chemistry of Materials*, vol. 28, no. 1, pp. 266–273, 2016.

[137] P. Barai, K. Higa, and V. Srinivasan, “Lithium dendrite growth mechanisms in polymer electrolytes and prevention strategies,” *Physical Chemistry Chemical Physics*, vol. 19, no. 31, pp. 20493–20505, 2017.

[138] L. Porz, T. Swamy, B. W. Sheldon, D. Rettenwander, T. Frömling, H. L. Thaman, S. Berendts, R. Uecker, W. C. Carter, and Y.-M. Chiang, “Mechanism of lithium metal penetration through inorganic solid electrolytes,” *Advanced Energy Materials*, vol. 7, no. 20, p. 1701003, 2017.

[139] Q. Tu, L. Barroso-Luque, T. Shi, and G. Ceder, “Electrodeposition and mechanical stability at lithium-solid electrolyte interface during plating in solid-state batteries,” *Cell Reports Physical Science*, vol. 1, no. 7, 2020.

[140] P. Barai, A. T. Ngo, B. Narayanan, K. Higa, L. A. Curtiss, and V. Srinivasan, “The role of local inhomogeneities on dendrite growth in llzo-based solid electrolytes,” *Journal of the Electrochemical Society*, vol. 167, no. 10, p. 100537, 2020.

[141] E. J. Cheng, A. Sharafi, and J. Sakamoto, “Intergranular li metal propagation through polycrystalline li6. 25al0. 25la3zr2o12 ceramic electrolyte,” *Electrochimica Acta*, vol. 223, pp. 85–91, 2017.

[142] S. Yu and D. J. Siegel, “Grain boundary softening: a potential mechanism for lithium metal penetration through stiff solid electrolytes,” *ACS applied materials & interfaces*, vol. 10, no. 44, pp. 38151–38158, 2018.

[143] M. Nagao, A. Hayashi, M. Tatsumisago, T. Kanetsuku, T. Tsuda, and S. Kuwabata, “In situ sem study of a lithium deposition and dissolution mechanism in a bulk-type solid-state cell with a li 2 s–p 2 s 5 solid electrolyte,” *Physical Chemistry Chemical Physics*, vol. 15, no. 42, pp. 18600–18606, 2013.

[144] F. Han, A. S. Westover, J. Yue, X. Fan, F. Wang, M. Chi, D. N. Leonard, N. J. Dudney, H. Wang, and C. Wang, “High electronic conductivity as the origin of lithium dendrite formation within solid electrolytes,” *Nature Energy*, vol. 4, no. 3, pp. 187–196, 2019.

[145] E. Kazyak, R. Garcia-Mendez, W. S. LePage, A. Sharafi, A. L. Davis, A. J. Sanchez, K.-H. Chen, C. Haslam, J. Sakamoto, and N. P. Dasgupta, "Li penetration in ceramic solid electrolytes: operando microscopy analysis of morphology, propagation, and reversibility," *Matter*, vol. 2, no. 4, pp. 1025–1048, 2020.

[146] G. Qian, G. Zan, P. Pianetta, and Y. Liu, "Perspective—morphology and dynamics of metal dendrites in batteries revealed by x-ray computed tomography," *Journal of The Electrochemical Society*, vol. 169, no. 12, p. 120540, 2023.

[147] T. Dussart, N. Rividi, M. Fialin, G. Toussaint, P. Stevens, and C. Laberty-Robert, "Critical current density limitation of llzo solid electrolyte: microstructure vs interface," *Journal of The Electrochemical Society*, vol. 168, no. 12, p. 120550, 2021.

[148] F. Flatscher, M. Philipp, S. Ganschow, H. M. R. Wilkening, and D. Rettenwander, "The natural critical current density limit for li 7 la 3 zr 2 o 12 garnets," *Journal of Materials Chemistry A*, vol. 8, no. 31, pp. 15782–15788, 2020.

[149] Y. Lu, C.-Z. Zhao, H. Yuan, X.-B. Cheng, J.-Q. Huang, and Q. Zhang, "Critical current density in solid-state lithium metal batteries: mechanism, influences, and strategies," *Advanced Functional Materials*, vol. 31, no. 18, p. 2009925, 2021.

[150] A. Sharafi, E. Kazyak, A. L. Davis, S. Yu, T. Thompson, D. J. Siegel, N. P. Dasgupta, and J. Sakamoto, "Surface chemistry mechanism of ultra-low interfacial resistance in the solid-state electrolyte li7la3zr2o12," *Chemistry of Materials*, vol. 29, no. 18, pp. 7961–7968, 2017.

[151] G. Lu, Z. Dong, W. Liu, X. Jiang, Z. Yang, Q. Liu, X. Yang, D. Wu, Z. Li, Q. Zhao, *et al.*, "Universal lithiophilic interfacial layers towards dendrite-free lithium anodes for solid-state lithium-metal batteries," *Science Bulletin*, vol. 66, no. 17, pp. 1746–1753, 2021.

[152] M. Cai, Y. Lu, L. Yao, J. Jin, and Z. Wen, "Robust conversion-type li/garnet interphases from metal salt solutions," *Chemical Engineering Journal*, vol. 417, p. 129158, 2021.

[153] R. J.-Y. Park, C. M. Eschler, C. D. Fincher, A. F. Badel, P. Guan, M. Pharr, B. W. Sheldon, W. C. Carter, V. Viswanathan, and Y.-M. Chiang, "Semi-solid alkali metal electrodes enabling high critical current densities in solid electrolyte batteries," *Nature Energy*, vol. 6, no. 3, pp. 314–322, 2021.

[154] C. Wang, H. Xie, L. Zhang, Y. Gong, G. Pastel, J. Dai, B. Liu, E. D. Wachsman, and L. Hu, "Universal soldering of lithium and sodium alloys on various substrates for batteries," *Advanced Energy Materials*, vol. 8, no. 6, p. 1701963, 2018.

[155] G. T. Hitz, D. W. McOwen, L. Zhang, Z. Ma, Z. Fu, Y. Wen, Y. Gong, J. Dai, T. R. Hamann, L. Hu, *et al.*, "High-rate lithium cycling in a scalable trilayer li-garnet-electrolyte architecture," *Materials Today*, vol. 22, pp. 50–57, 2019.

[156] H. Wang, Y.-I. Jang, B. Huang, D. R. Sadoway, and Y.-M. Chiang, “Tem study of electrochemical cycling-induced damage and disorder in licoo2 cathodes for rechargeable lithium batteries,” *Journal of the Electrochemical Society*, vol. 146, no. 2, p. 473, 1999.

[157] T. Holme, M. Mayer, G. Loveness, Z. Chen, and R. Fasching, “Pulse plating of lithium material in electrochemical devices,” Sept. 22 2020. US Patent 10,784,497.

Appended papers

Paper I

Paper II

Paper III

Paper I

Effect of pulse-current-based protocols on the lithium dendrite formation and evolution in all-solid-state batteries

V. Reisecker, F.Flatscher, L. Porz, C. Fincher, J.Todt, I. Hanghofer,V. Hennige, M. Linares-Moreau, P. Falcaro , S. Ganschow, S. Wenner, Y.-M. Chiang, J. Keckes, J. Fleig and D. Rettenwander. *Nature Communications* **14** (1), 2432 (2023).

nature communications

Article

https://doi.org/10.1038/s41467-023-37476-y

Effect of pulse-current-based protocols on the lithium dendrite formation and evolution in all-solid-state batteries

Received: 5 July 2022

Accepted: 17 March 2023

V. Reisecker[1,2,11], F. Flatscher[2,3,11], L. Porz[3], C. Fincher[4], J. Todt[5], I. Hanghofer[6], V. Hennige[6], M. Linares-Moreau[7], P. Falcaro[7], S. Ganschow[8], S. Wenner[9], Y.-M. Chiang[4], J. Keckes[5], J. Fleig[10] & D. Rettenwander[1,2,3]

Understanding the cause of lithium dendrites formation and propagation is essential for developing practical all-solid-state batteries. Li dendrites are associated with mechanical stress accumulation and can cause cell failure at current densities below the threshold suggested by industry research (i.e., >5 mA/cm^2). Here, we apply a MHz-pulse-current protocol to circumvent low-current cell failure for developing all-solid-state Li metal cells operating up to a current density of 6.5 mA/cm^2. Additionally, we propose a mechanistic analysis of the experimental results to prove that lithium activity near solid-state electrolyte defect tips is critical for reliable cell cycling. It is demonstrated that when lithium is geometrically constrained and local current plating rates exceed the exchange current density, the electrolyte region close to the defect releases the accumulated elastic energy favouring fracturing. As the build-up of this critical activity requires a certain period, applying current pulses of shorter duration can thus improve the cycling performance of all-solid-solid-state lithium batteries.

Providing future generations with sustainable and emission-free electrified transportation requires the development of energy storage concepts with specific energies of at least 400 Wh/kg[1]. This demand exceeds, however, the limit which can be reached by conventional Li-ion batteries (LiBs; ~250 Wh/kg)[2–5]. One viable solution to this issue could be the replacement of the flammable non-aqueous liquid electrolyte solution with an inorganic solid-state electrolyte (SSE), which, not only allows for an improved safety, but also the application of Li metal as the negative electrode, leading to a substantial increase in energy density (up to 50%)[3,5]. One of the most promising SSEs to enable such high performance solid-state Li batteries is cubic $Li_7La_3Zr_2O_{12}$ (LLZO) and its variants. In comparison to other SSEs, it can provide a high room-temperature Li-ion conductivity approaching that of a conventional non-aqueous liquid electrolyte solution, whilst simultaneously showing good chemical and electrochemical stability toward Li metal and high-voltage cathodes[6–8].

However, to reach the promised performance, solid-state Li batteries must plate a large Li thickness of at least 15 μm or 3 mAh/cm^2 at a high (charging) current rate (>5 mA/cm^2) for a minimum of 1000 full cycles[5,9–12]. Today, under such conditions, these batteries invariably fail due to the formation of Li dendrites penetrating the SSE and causing a short-circuit[3,4,9,10,13]. One of the main reasons for this battery failure are

---

[1]Institute of Chemistry and Technology of Materials, Graz University of Technology, Graz, Austria. [2]Christian Doppler Laboratory for Solid-State Batteries, NTNU Norwegian University of Science and Technology, Trondheim, Norway. [3]Department of Material Science and Engineering, NTNU Norwegian University of Science and Technology, Trondheim, Norway. [4]Department of Materials Science and Engineering, Massachusetts Institute of Technology, Cambridge, MA, USA. [5]Department of Materials Physics, Montanuniversität Leoben and Erich Schmid Institute for Materials Science, Austrian Academy of Sciences, 8700 Leoben, Austria. [6]AVL List GmbH, Graz, Austria. [7]Institute of Physical and Theoretical Chemistry, Graz University of Technology, Graz, Austria. [8]Leibniz-Institut für Kristallzüchtung, Berlin, Germany. [9]Sintef Industry, Department of Materials and Nanotechnology, Trondheim, Norway. [10]Institute of Chemical Technologies and Analytics, TU Wien, Vienna, Austria. [11]These authors contributed equally: V. Reisecker, F. Flatscher. e-mail: daniel.rettenwander@ntnu.no

current constrictions at the Li|SSE interface that arise from, e.g., (1) poor contact between the Li metal electrode and the SSE, (2) grain boundaries, or (3) void formation at the Li|SSE interface during Li metal stripping[9,10]. The resulting high local current densities lead to electrochemo-mechanical stresses high enough to initiate Li penetration into the SSE, finally resulting in a short circuit and even cell failure[9,11,13].

To address this issue, various concepts have been explored like the introduction of Li-alloys/interphases (e.g., Sr, ZnO, and Mo)[14–16], additives (e.g., Li_3PO_4 or excess LiOH)[17,18] or interface engineering (e.g., introducing different atomic interlayers or creating 3D structures)[19,20], all of which are measures to enhance the SSE's wetting and/or increase the Li|SSE contact area. Applied on their own, these approaches are, however, not sufficient to meet the performance demand for practical applications. Only in combination with a constant heat supply, leading to a faster Li^+ diffusion[21], or the application of stack pressure to enhance the Li creep from the anode toward the interface[22], the necessary current density threshold becomes tangible. An increased operating temperature is, unfortunately, not applicable under all circumstances and additionally represents a constant energy drain. Furthermore, the application of stack pressure increases the risk of mechanical failure and is technologically challenging, as are some alloy formations[23]. To make use of the already achieved progress while bypassing critical temperature and pressure conditions, a different approach is needed that is compatible with the aforementioned methods. One such solution could be the alteration of the external current application. Pulsed currents are often utilized in electroplating of metals to achieve more uniform deposits[24–26] and have already been applied in Na||O_2 battery and N_2O electrochemical reduction systems[27,28]. Current pulses therefore represent a potentially useful method for inhibiting Li dendrite formation[29–32].

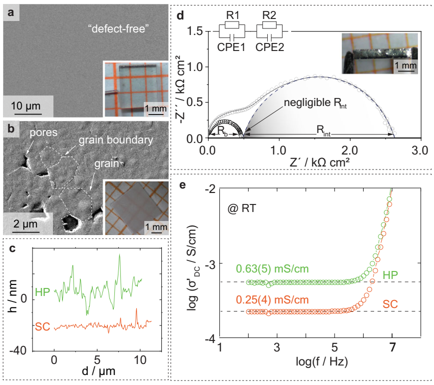

Fig. 1 | Physicochemical and electrochemical characterizations of the inorganic solid-state electrolytes. a (inset) Single crystalline $Li_6La_3ZrTaO_{12}$ (SC) specimen and **b** (inset) hot-pressed polycrystalline $Li_{6.4}La_3Zr_{1.4}Ta_{0.6}O_{12}$ (HP) specimen in top view after shaping and thorough polishing on millimeter paper. The samples were additionally investigated via scanning electron microscopy (**a**, **b**) prior to coating with Li:Sn. In the case of the SC sample no indication of any microstructural defect was found, whereas the HP pellet shows a very dense microstructure composed of grains with diameters around 2 µm and pores up to 1.5 µm. **c** Corresponding atomic force microscopy analyses were conducted to assess the defect concentration of the SC (orange) and HP (green) surface, and the measured height *h* profile plotted against the distance *d* covered. Note: for comparison reasons the topography profile of the SC sample was shifted by −20 nm. **d** Impedance data of an SC sample with (black) and without (gray) a proper surface treatment, measured in a symmetrical Li:Sn cell at 21 ± 1 °C without stack pressure. The inset demonstrates the homogeneity of the coating procedure after polishing. The negative imaginary part $-Z''$ is plotted against the real part of impedance Z' in form of a Nyquist plot. In case of the polished sample, only the bulk contribution (R_b) can be properly identified, whereas the interfacial contribution (R_{int}) is negligibly small. Fits were calculated using the circuit shown on top, consisting of resistance elements R and constant phase elements CPE. Experimental data are represented by circular markers, fitted data by line markers. **e** Conductivity σ is plotted against the frequency in form of a conductivity isotherm of an SC (orange) and HP sample (green), again, measured in a symmetrical Li cell at 21 ± 1 °C.

Upon application of a direct current to a conventional LiB, Li-ions start to deposit throughout the whole electrode|electrolyte interface and can gather in certain areas causing concentration gradients. In case of a pulsed current program, where the current profile is interrupted by pausing/current-off times, the Li-ions have time to diffuse from regions of high concentrations toward regions of low concentrations (during said pausing times) which overall results in a denser and uniform Li-ion deposition[33–35]. Implementing a voltage pulse into the charging protocol of an all-solid-state high-voltage Li metal cell has already proven to reduce the interfacial impedance by refilling formed voids via Joule heating[36]. While a single pulse was not found to significantly enhance the current density limit, a repetitive application of pulses in a Li||LiFePO4 cell with conventional non-aqueous liquid electrolyte solution has turned out to produce dense microstructures. The application of conventional direct current on the other hand initiated rapid growth of porous Li film structures, degrading the cycling performance significantly[37]. Moreover, it has been shown that the mitigation of current constrictions by pulsed current waveforms enables a substantial suppression of the dendrite growth[34,38,39]. Another application is to intermittently apply a reverse current in a pulse form or a very small direct current (1–20 µA/cm²) to remove grown dendrites and receive a denser Li morphology[40,41]. Besides for morphological aspects, pulsed currents have also been studied as a measure to adjust the operating temperature of a battery by means of a self-heating mechanism[42,43].

Despite the potential of pulse plating to surmount the limitation imposed by Li dendrites in conventional LiBs, its effectiveness with respect to solid-state Li batteries has received only minor attention. Theoretical work has mostly focused on the effects of pulsed currents on non-aqueous liquid electrolyte solutions and the mechanisms studied therein are not necessarily transferable to solid electrolytes, where ions are spatially confined and much less mobile[29,34,35,38,39].

Specifically, it is not clear to which extent and how pulsed current waveforms can increase the so-called Critical Current Density (CCD) of solid-state batteries, which is the current density up to which safe cycling can be conducted without the formation of Li filaments[10,44,45] and what impact setting parameters like the pulse/pause ratio, frequency or applied current density have. Since the application of pulsed currents is an external electrochemical measure and does not interfere with any internal measures taken to increase the CCD, such as the application of alloys, additives, or interface engineering, it can be widely applied on top of such methods.

Herein, to analyze the impact of current pulses on different inorganic solid-state electrolyte morphologies, single crystalline $Li_6La_3ZrTaO_{12}$ (SC) and hot-pressed polycrystalline $Li_{6.4}La_3Zr_{1.4}Ta_{0.6}O_{12}$ (HP) cuboids of high geometrical and interfacial quality were prepared and subjected to different pulse plating protocols. A wide spectrum of techniques, such as focused ion beam, scanning electron microscopy, transmission electron microscopy, atomic force microscopy and electrochemical impedance spectroscopy were applied to retrieve a full sample profile. Afterwards, all samples were galvanostatically cycled in symmetrical Li cells using either direct or pulsed currents, whereby short circuits have been identified and tracked via operando Optical Microscopy.

This study reveals that MHz pulses enable up to a six-fold increase in CCD, leading to values as high as (6.6 - 0.1) mA/cm². The increase in

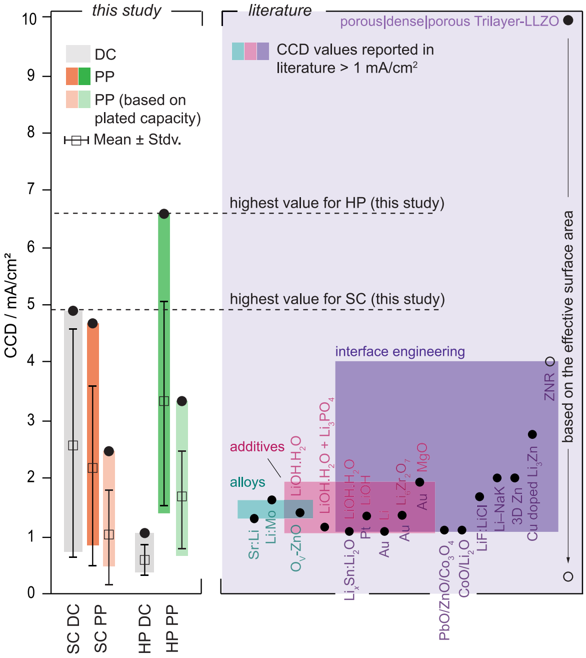

Fig. 2 | Analysis and comparison of the experimental electrochemical measurements. Ranking of the critical current density (CCD) values achieved for single crystalline (SC) and hot-pressed polycrystalline (HP) samples during either direct current application (DC; marked in gray) or pulse plating (PP; marked in orange and green for single crystalline and polycrystalline samples, respectively) operation. CCD values obtained during pulse plating are represented by black circular markers, whereas effective CCD_{eff} values, considering the time increase during the measurement compared to the values when direct current has been applied, are plotted as white rectangular markers. The violet section shows CCD values above $1\,\text{mA/cm}^2$ reported in literature for different LLZO chemistries (excluding potentially soft shorted samples or values obtained at temperatures higher than room temperature and/or high stack pressure, to our best knowledge; based on refs. 14–20,23,55–63. from left to right—see also Supplementary Table 5). Values were grouped into one or two of three categories depending on their strategy being either (1) the coating of an alloy onto the SSE (petrol), (2) application of an additive during the sintering procedure (pink) or (3) the engineering of the SSE interface by e.g., structuring or application of an additional interlayer (purple). For the rightmost value the full circle corresponds to the reported current density for the porous structure and the empty circle to the current density if the porous structure were planar.

CCD can be associated with the application of current pulses shorter than the time required to build up a critical Li activity near a defect tip located at the Li|SSE interface. Once reached, this critical Li activity leads to the structural destabilization and fracture of the SSE, which is accompanied by Li dendrite initiation and propagation.

Results and discussion

Ensure minimum sample-to-sample variation

One of the main challenges in studying the CCD in a reliable and reproducible manner is its dependency on microstructural features like grain boundaries, voids and flaws[46–48] or also chemical variations even within similarly prepared samples[49,50]. In order to reduce the impact of sample-specific parameters on the CCD measurements and guarantee comparable starting conditions for all experiments, special attention was paid to minimize sample-to-sample variations for each morphology type. Therefore, rectangular shaped SC and HP samples exhibiting similar sizes of roughly 3 mm × 3 mm × 0.5 mm (width, length, thickness) with densities of 100% and >99%, respectively, were prepared (see Fig. 1a, b, details regarding the sample preparation can be found in "Methods" section and Supplementary Figs. 1 and 2). To achieve a minimal defect concentration at the electrolyte surface, a thorough surface treatment procedure consisting of multiple rotational and vibrational polishing steps was applied. Scanning electron microscopy images of the SCs did not reveal any macroscopic pores or larger scratches (Fig. 1a) present at the polished surface. The HP samples showed a dense microstructure with grains in the size of about 4 μm in diameter (Fig. 1b) and only minor pores up to about 1 μm in diameter. In both cases, a smooth surface profile was achieved with root mean square (RMS) roughness values of (3 ± 1) nm and (8 ± 3) nm for the SC and HP samples, respectively (Fig. 1c and Supplementary Fig. 3).

Besides its morphological dependency, the CCD has been found to be heavily influenced by current constrictions along the Li|SSE interface[9,10]. Current constrictions are related to missing contact associated with insufficient Li wetting or surface contaminants for instance.

Moreover, the ratio between the conductivity of the SSE and the exchange current density has been shown to have a significant impact

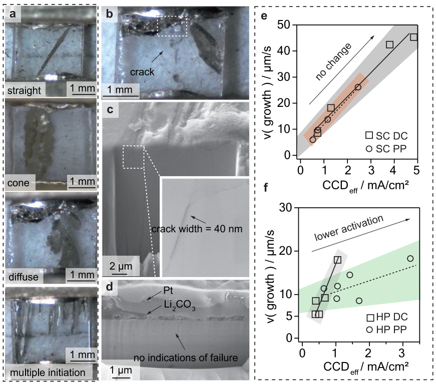

Fig. 3 | Microscopy investigations of the Li metal depositions. a Overview of different Li dendrites observed during optical tracking of single crystalline samples being of either straight, cone or diffuse, type. In some cases, multiple dendrite initiation was spotted, where dendrites started growing from several initiation sites at the same time. The dendrite growth can be seen in motion in Supplementary Videos 1–5. Crack analysis performed on an SC (**b**–**d**) and HP (**f**), cut parallel to the formerly coated electrolyte surface with a focused ion beam. For the single crystalline sample small subsurface cracks at a width of 40 nm were found, whereas for the hot-pressed no cracks large enough to resolve were found. Growth rates plotted against the effective critical current density (CCD_{eff}) values in case of direct current (DC) or pulsed current (PP) operation for single crystalline LLZTO (SC, **e**) and hot-pressed polycrystalline LLZTO (HP, **f**). The trends have been colored in gray (DC), orange (SC PP) and green (HP DC) for visualization purposes.

on the uniformity of metal deposits[51]. The area specific resistance (ASR) directly reflects both, the exchange current density (according to Butler-Volmer) and the degree of physical contact[9,45]. Hence, a reliable experimental platform has to ensure similar ASR values, as well as similar Li-ion conductivities within one experiment series. Therefore, potential contaminants at the SSE surface, such as LiOH and Li_2CO_3, have been removed by a proper polishing sequence with a subsequent heat treatment at 400 °C in Ar atmosphere[52]. Moreover, a molten Li:Sn electrode (70:30 wt%) has been used to improve the wetting of Li on the SSE[53]. The combination of both approaches led to a reproducible reduction of the ASR value down to negligible values (see Fig. 1d and Supplementary Note 1). This is elaborated further in Supplementary Tables 1 and 2 as well as Supplementary Fig. 4. The variation in Li-ion conductivity across the SC and HP samples was investigated by plotting the electrochemical impedance spectroscopy data in a Bode-like fashion (Fig. 1e). Both conductivity isotherms reveal a single direct current plateau, which, in the case of the SC, can be related to the bulk conductivity due to the lack of grain boundaries. In case of the HP sample, the grain boundaries appear to not significantly contribute to the total resistance of the SSE, resulting in a single contribution as well. The averaged conductivities and deviations of the SC and HP samples amount to (0.25 ± 0.04) mS/cm (mean ± std) and (0.63 ± 0.05) mS/cm at (21 ± 1) °C, respectively, pointing toward minor sample-to-sample variations in terms of resistance. Additional information can be found in Supplementary Figs. 5 and 6.

In addition to these parameters, experimental conditions, like temperature[21] and pressure[54] impact the CCD. Increasing either of the two can significantly elevate the CCD value, e.g., by enhancing the creep of Li metal and its diffusivity. Therefore, all experiments were conducted at a constant temperature (21 ± 1) °C and without the application of significant stack pressure (less than 3 kPa, see Supplementary Note 2).

The critical current density

Different pulsing sequences were tested in preliminary experiments with polycrystalline LLZTO (PC) pellets prepared by conventional solid-state synthesis, where the pulse-pause ratio was varied from 1:1 to 1:10 in the ms-range. Whereas these cycling conditions did not improve the electrochemical performance of the PC pellets, reducing the respective timeframes to the µs-regime enhanced the CCD values achieved in contrast to direct current operation for a 1:1 pulsed current condition (see Supplementary Note 3 and Supplementary Table 2). The same pulsing sequence was then applied to the SC and HP samples and compared to the CCD values achieved under direct current operation (see Fig. 2, Supplementary Note 4 and 5 and Supplementary Tables 3 and 4). Since the pausing time in the pulsing sequence prolongs the overall cycling time, an "effective" CCD value (CCD_{eff}) was defined on the basis of the plated capacity for better comparison. For a 1:1 pulsing sequence, taking twice as long as direct current cycling, the obtained CCD value was therefore divided by two. Prior to any cycling experiment conducted with pulsed waveforms, the efficiency was evaluated by galvanostatic titration and plating experiments. The measurements revealed that pulsed currents down to the µs-range can achieve efficiencies up to 100% (see Supplementary Note 6 and Supplementary Figs. 7 and 8). In the case of the SC and HP samples, the cycling profile was complemented by simultaneously taken optical microscopy images, easing the identification of Li dendrite formation (details are given in Supplementary Note 4, Supplementary Figs. 9 and 10 and Supplementary Videos 1–5).

For the SC samples, CCD values up to (4.95–0.05) mA/cm² (current at potential drop–current step size, taken as range containing actual CCD value) have been achieved by using direct current application. Compared to similar samples lacking an extensive surface treatment[45], this represents an increase of around 170%, thereby highlighting the sensitivity of the CCD on the electrolyte's surface condition. In Fig. 2 and in Supplementary Table 5 previously reported CCD values are summarized (note: based on the effective surface area; values related to potential soft shorts, higher temperature and high stack pressure are excluded). Values up to 4 mA/cm² have so far been achieved by using alloys (e.g., Li:Mo, Sr:Li), additives (e.g., $LiOH•H_2O$) and/or interface engineering (e.g., MgO, Cu-doped Li_3Zn)[14–20,23,55–63]. While the SC samples exceed these values by 1 mA/cm², they are, however, not practicable for large-scale production, due to possible cost and manufacturing concerns. Applying a direct current protocol to the HP samples, however, led to average CCD values below 1 mA/cm², proving that the presence of grain boundaries and small pores reduces the CCD (see Supplementary Tables 3 and 4). When switching to pulsed currents, no significant difference in electrochemical performance could be found for the SC samples. While the maximum CCD reached a similarly high value of (4.8–0.1) mA/cm², the overall average was lower, taking on a value of (2.1 ± 1.6) mA/cm², as opposed to (2.7 ± 2.0) mA/cm² for direct current cycling. Based on the CCD_{eff} of (1.0 ± 0.8) mA/cm² it becomes evident that in the case of SCs, pulsed currents cannot effectively enhance the CCD. For HP samples on the other hand, an improvement could be observed with a maximum CCD of (6.6–0.1) mA/cm² and an average of (3.3 ± 1.8) mA/cm². Even based on the CCD_{eff} of (1.7 ± 0.9) mA/cm², pulsed currents can by far outperform cells cycled under direct current conditions reaching average CCDs around (0.6 ± 0.3) mA/cm².

These results indicate that MHz pulsed currents can mitigate critical defects up to a certain current density range, enabling current densities as high as (6.6–0.1) mA/cm², and an increase by a factor of three concerning the plated capacity. Notably, despite our efforts to mitigate as many influencing factors as possible, large variations in

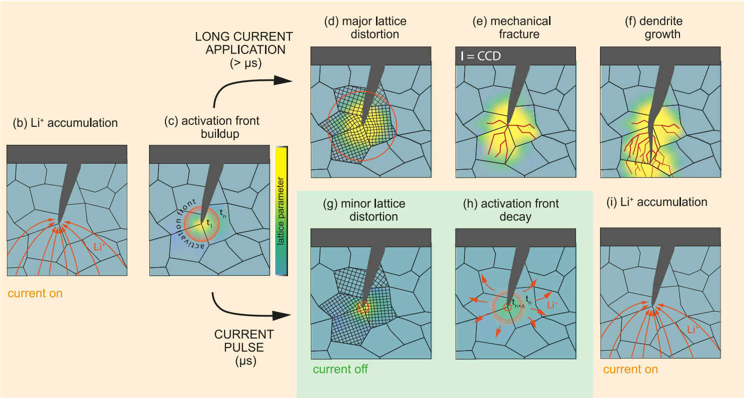

Fig. 4 | Proposed mechanisms in constant current and pulsed current electrochemical experiments. Flow diagram showing the proposed mechanistic differences between direct current and pulsed current (µs) operation of a solid-state cell employing a Li metal anode: **a** pristine condition of the Li|SSE interface exhibiting a surface scratch of the SSE filled with Li, along with the lattice orientations of the adjacent grains near the defect tip. **b** Once the current is switched on Li-ions start to concentrate near the defect tip and **c** cause the buildup of an activation front, increasing over time t_n. LLZTO is thereby locally reduced and the lattice parameter in this region changed. **d** In case of direct or long current pulse (>µs) application this continuous lattice distortion causes a continuously increasing amount of pressure which, at some point, is released in form of (**e**) mechanical fracture. As a consequence, Li is plated along the new cracks (**f**) and drives the mechanical fracture even further until a short circuit is caused. **g** In case of short current pulses (µs) the time for the activation front buildup is short enough to just cause a minor lattice distortion before the current is switched off again. **h** The accumulated Li-ions start to diffuse and distribute into the neighboring regions, hindering a significant pressure to arise. **i** Afterwards, the current is switched on again like in (**b**) and the process repeats itself.

CCD values were still observed. This suggests that studies on CCDs should, in general, be statistically evaluated to ensure reproducibility.

Li dendrite characteristics

During optical tracking of Li dendrite initiation and propagation in SCs, a multitude of different dendrites has been observed, which were essentially grouped into one of three different categories similar to the classification used by Kazyak et al.[64]: straight, cone or diffuse type (see Fig. 3a). The straight type is characterized by a 2D Li deposition throughout the SSE, whereas the cone type branches out at the sides causing more of a 3D growth pattern. In the case of the diffuse type, Li did plate in a flowing manner followed by a macroscopic fracture of the electrolyte. For the multiple initiation type, filament growth started at several initiation sites at once and continued growing at the same time. Figure 3b–d shows the analysis of the crack widths of a typical shorted SC and HP sample using a focused ion beam-scanning electron microscope. In the SC sample sub-surface cracks with widths of about 40 nm were observed, whereas the HP sample did not show any signs of intra- and/or intergranular crack propagation. This observation could, however, also be related to the formation of dendrites below the resolution limit of the scanning electron microscope. As all dendrite types were observed in both cycling programs, no clear correlation between the current waveform and the respective shape of the dendrite could be found. In most cases, either a straight or cone-like Li propagation was observed, whereas the diffuse type was encountered very rarely. In contrast to the observations Kazyak et al.[64] have made, the propagation of each dendrite type was accompanied by a decrease in potential. Overall, initiation sites were found to be randomly distributed across the whole interface and only numerous in case of high CCDs (Fig. 3a bottom). As for the HP samples, Li dendrite formation was not observed to follow a single initiation event, but multiple ones, starting simultaneously throughout larger areas of the Li|SSE interface (Supplementary Fig. 11). Next to so-called hard shorts, soft shorts, in some cases exhibiting seemingly reversible Li deposition, have also been observed but were not further studied herein (see Supplementary Note 7 and Supplementary Figs. 12 and 13).

The growth kinetics

Growth rates were determined by dividing the distance between the electrodes overcome by the time needed to reach the opposing electrode. Figure 3e, f shows the average growth rates of both morphology types obtained under either direct or pulsed current conditions. A linear relationship between the CCD and the growth rate becomes evident, which is in agreement with previous studies[64]. In the case of the SCs, Li deposition rates as a function of CCD progressed at speeds of 8.4 µm/(s(mA/cm²)) and 10.5 µm/(s(mA/cm²)) under direct and pulsed current operation, respectively, indicating little dependence of the Li deposition mechanism on the pulse waveform. Applying the same approach to the HPs, pulsed currents were observed to reduce the growth rate increase with increasing CCD from 13.7 µm/(s(mA/cm²)) to 1.1 µm/(s(mA/cm²)). These observations suggest that Li propagation follows a different mechanism in polycrystalline samples under pulsed currents as opposed to in single crystalline ones.

The growth rate of a dendrite can be expressed by dx/dt and based on our observation takes on a value of about 10 µm/s at 1 mA/cm². The current density at the tip, required to enable growth rates up to 10 µm/s, can be derived from Eq. (1):

$$j = \frac{I}{A} = \frac{\left(\frac{dV}{dt} \times \frac{1}{V_m^{Li}}\right) \times F}{A} = \frac{\left(A \times \frac{dx}{dt} \times \frac{1}{V_m^{Li}}\right) \times F}{A} = 7\,\frac{A}{cm^2} \qquad (1)$$

The total current flowing is denoted by I, the molar volume by V_m^{Li}, which amounts to 13.148 cm³/mol and F represents the Faraday constant. Note that the tip area of the dendrite A cancels out in the equation, which means that the current density is independent of the size of the dendrite in a first approximation. If the current for the entire cell is much larger than the current needed for driving the dendrite, which is typically the case evidenced by no or only minor voltage drops before a short circuit, such an approximation can be made. According to this relation, the current densities needed to achieve the observed growth rates are in the range of 7 A/cm^2 when considering the required charge transfer to provide the necessary volume of Li. This value is larger than the exchange current densities reported for LLZO so far, which lie around 0.3 A/cm^2 [65]. Hence, the high current density causes a significant polarization at the dendrite tip during plating with detrimental consequences.

The mechanism

As previously mentioned[46,66], the propagation of dendrites through ceramic electrolytes is suggested to be associated with the geometrical constraint for Li within a defect. Due to this constraint, a critical pressure builds up as soon as the defect is filled, causing a protrusion of Li into the SSE. This failure occurs instantaneously with the applied current (see finite element calculation described in Supplementary Note 8 and Supplementary Figs. 14 and 15), which would indicate that the longer pulses in the μs-range should not have any implications on the propagation of Li dendrites. The experiments with the HP samples, however, showed that the CCD is increased by a factor of six, whereas the Li growth rate decreases by one order of magnitude when switching from direct to MHz pulsed currents. Hence, the previously proposed mechanism of mechanical failure associated with the penetration of Li needs to be revisited to describe our observations.

Our main hypothesis is that the buildup of a Li-ion activity front in the neighboring region of a defect tip is responsible for a critical pressure buildup, eventually followed by fracture of the SSE and dendrite propagation. As the buildup of this critical Li-ion activity does not occur instantaneously once the current is switched on, current pulses of short enough duration can prevent the incident of this case. In this sense mechanical fracture actively drives the formation of Li dendrites rather than merely accompanying it. This suggested new mechanism not only explains the formation of Li dendrites under DC operation (see Fig. 4a–f) but would also be in accordance with the electrochemical performance increase observed for pulsed current operation (Fig. 4a-c, g–i), as elucidated in the following.

In its pristine condition (Fig. 4a), a solid-state cell employing a Li-metal electrode and polycrystalline LLZTO electrolyte will show surface defects like scratches (as observed in Supplementary Fig. 3) ultimately filled with Li after construction. In order to extend cracks within an SSE and allow the propagation of Li dendrites, bonds need to be broken. We suggest that the corresponding driving force is introduced locally and not as approximated previously by a homogeneous load[46]. The required energy gain to overcompensate the energy needed to break bonds can come from (1) the release of the chemical driving force from a Li chemical potential (or activity) in the SSE being above that of Li metal, and (2) the release of elastic energy due to an enhanced Li activity near the dendrite (and crack) tip. Both energy contributions emerge from the same phenomenon, being the accumulation of Li-ions and electrons in close proximity to the Li-filled crack tip once an electrode overpotential is applied (Fig. 4b). This is in accordance with Han et al. where a substantial enhancement of the electronic conductivity is found close to the Li electrode upon polarization[67]. In Solid-State Ionics this is well known as stoichiometry polarization or Wagner-Hebb polarization, where a blocking of ionic charge carriers at the electrode is present[67,68]. This is valid, as long as the critical conditions leading to the initiation and growth of Li dendrites are not met. Then, LLZTO is locally reduced and thus the electron concentration enhanced, driven by the very high current densities of beyond 1 A/cm² (see Eq. (1) above).

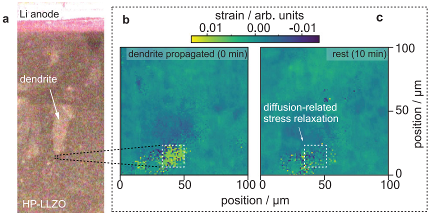

Fig. 5 | Operando microscopy and X-ray measurements of the Li metal and solid-state electrolyte. a The dendrite is highlighted in an optical microscope overview image, while the mapped region of 10 × 10 μm is marked as a black-dashed square. The corresponding operando synchrotron X-ray nano diffraction strain maps show the region ahead of a Li dendrite directly after its growth and after a waiting time of ~10 min. A single grain is highlighted and exhibits a deviatoric strain of -0.0045 (**b**, 0 min), and −0.0015 (**c**, 10 min), equivalent to a change in deviatoric stress of ~750 MPa. This relaxation was not detected when comparing the state during the dendrite's growth and to the state directly thereafter. The grain is located ~8–10 μm in front of the assumed dendrite tip.

The local stoichiometry change (i.e., additional Li-ions and changed ionic valences due to additional electrons, Fig. 4c) induces a change of the local lattice parameter similar to, e.g., doped ceria (i.e., SSE for solid oxide fuel cells) under very reducing conditions[69]. This change only arises near the defect-tip region and is therefore suppressed by the mechanical constraints toward the bulk part of LLZTO, which is unaffected by Li activity changes (Fig. 4d). Accordingly, a substantial elastic energy builds up until a critical Li activity is reached resulting in stress relaxation by fracture (Fig. 4e) followed by Li dendrite propagation (Fig. 4f). Further evidence for this theory is given by observations of grain relaxation in an HP sample (Fig. 5a) measured by operando synchrotron XRD (1) directly during dendrite growth (Fig. 5b) and (2) after 10 min of current pause (Fig. 5c), allowing for diffusion. These measurements highlight the apparently strong mechanical sensitivity of LLZTO toward the local Li activity. Specifically, the 2nd-order (grain-average) deviatoric strain was observed to change from -0.0045 to ~ −0.0015 within a single grain located between 8 to 10 μm away from the dendrite tip within 10 min. This corresponds to a difference in deviatoric stress on the order of 750 MPa. Other phenomena such as crack extension would act much faster, i.e., with the propagation speed of phonons, and can therefore be ruled out as explanation for this observed relaxation. Similar behavior can be also found, e.g., in $LiCoO_2$[70], and Si[71] where the insertion of Li-ions into the particle causes a volume mismatch between the new phase near the surface and the existing phase in the bulk once the relaxation kinetics is slower than the transfer rate. This volume mismatch causes a high enough chemo-mechanical strain to induce plastic deformation, mechanical fracturing and even amorphization. This effect can also be found in, e.g., fracture of rock formations as a consequence of water uptake, which could be seen as an analogous mechanism. The change of the unit cell upon incorporation leads to an expansion or shrinkage, inducing stresses which eventually cause the stone to crack[72].

Overall, these arguments strengthen the theory that dendrite propagation is promoted by the mechanical weakening of the SSE (i.e., decrease of the fracture resistance) at the crack tip caused by the constant increase in Li activity under current application. The time dependence of this process can be described by the ambipolar (chemical) diffusion coefficient of Li-ions in LLZTO. The exact time and space thereby depend on the geometry of the defect and the location at which Li-ions are injected and where electrons originate from[73]. Contrary to the concept of Sand's time, which has been used to

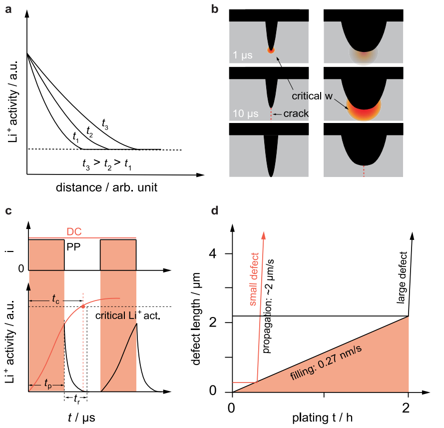

Fig. 6 | Trends and observations concerning Li activity front and defect size. **a** Activity front at SSE|Li interface and growth of rim with increasing time (arbitrary chosen times t_1, t_2 and t_3 where $t_1 < t_2 < t_3$). **b** Schematics illustrating that a smaller activity front (red) with a critical width w is sufficient to crack up the environment of small defects, (black) in the solid electrolyte (gray) whereas a thicker activity front is needed for the same result in case of bigger defects. It therefore takes for a longer time to induce fracture in the vicinity of big defects as opposed to smaller ones. **c** Increase of Li activity as a function of plating time between pulse plating (PP) and direct current (DC) application. The illustration shows that if the current is applied for a shorter amount of time (t_p) than what is needed to reach the critical Li activity (t_C), a structural degradation can be avoided/delayed, while relaxing for t_r. **d** Time required until a defect gets critical (i.e., filled completely) by considering a plating rate of 0.27 nm/s (assuming a current density of 0.2 mA/cm^2), demonstrating that smaller defects are most critical in terms of filament initiation and propagation. Further elaborated in Supplementary Note 9.

describe the transition from mossy Li growth to dendritic growth in liquid cells via the formation of a Li-ion depletion layer and subsequent Li-ion deposition in current hotspots[74,75], we postulate a local increase of Li-ions. As already mentioned, this increase in Li-ion activity takes place at a defect near the Li|LLZTO interface (Fig. 4b), whereby in a first approximation a few assumptions can be made. On the one hand that there is an equilibration of electrons and on the other hand that any change of the interfacial double layer and any additional contribution of the interfacial charge transfer to the kinetics (i.e., considering diffusion rather than the Butler-Volmer limited case, due to the local constrain of Li metal in a filled crack tip) can be neglected. Hence, the applied overpotential directly transfers to a locally enhanced Li activity creating an activity front at the Li dendrite tip. The diffusion into the surrounding LLZTO regions (Figs. 4b and 6a), is determined by the chemical diffusion coefficient of Li-ions, D. Assuming radial symmetry for diffusion with the concentration C(R) at the center, a constant D value and concentrations instead of activities, the additional Li-ion concentration $C(r,t)$ at radius r and time t in the corresponding region can be determined with Eq. (2):

$$C(r,t) = C(R) \cdot \operatorname{erf}\sqrt{r/Dt} \tag{2}$$

The quantitative relation between the additional Li-ion concentration and the activity of Li (or the overpotential) is not known. However, the effective thickness w of such a diffusion front with the diffusion coefficient D and the time t can be approximated according to Eq. (3):

$$w = \sqrt{Dt} \tag{3}$$

It shows that this "rim", having an enhanced Li-ion activity, increases with time (Fig. 6a). From a mechanistic point of view, the tip radius R defines the stress concentration at a flaw. We suppose that to reach the critical condition for dendrite growth, a certain Li-ion activity is needed at the tip. For example, based on Eq. (3), it will take 100 times longer to reach critical conditions for a ten times larger R (Fig. 6b). Therefore, a tip with a large radius R (e.g., pores, scratches) requires a thicker activity front as opposed to a sharp tip (e.g., grain boundaries). In other words, the time required to reach the critical activity front is shorter for a tip with smaller R. Since the accumulation of a critical activity front at a dendrite takes place in the sub-ms range (depending on the applied current), this time dependence does not play a significant role for direct current charging.

In the case of pulsed currents, however, this time dependence becomes significant. For 1 MHz pulses the activity front can build up for just one microsecond, which is too short to reach critical conditions and only a minor lattice distortion takes place (see Figs. 6c and 4g). In the subsequent microsecond the Li-ion activity front can then relax again during the pausing time (Fig. 4h). As the current is switched on again, a similar starting condition is given and the cycle repeats itself (Fig. 4i). Hence, the propagation of Li dendrites is suppressed by taking away the driving force, i.e., fracture of the SSE at high Li-ion activity.

This explains the increase in CCDs and lower propagation rates of Li dendrites in case of the HP samples when pulsed currents are applied and why the SC samples remain unaffected under the same conditions. Considering that grain boundaries are sharp defects with lower fracture toughness compared to the bulk, Li dendrites are predominantly formed in these regions (see detailed discussion on the failure likeliness of different types of defects and defect sizes in Supplementary Note 9 and Supplementary Fig. 16). Hence, when the pulsed current frequency is sufficiently high, Li penetration will then take place, e.g., along grain boundaries at much higher currents (or any other defect for which the time required to reach a critical Li activity front is less than the pulse frequency) explaining the six-fold increased CCD for HP samples. The lower propagation rate during pulsed current application can be associated with local fluctuations in Li-ion transport and Li deposition rates[67]. These cause stress accumulation at the branch tips, which are created once Li starts to penetrate the SSE. Considering that the branch tips are "sharper", as opposed to the primary tip, they are most sensitive to failure (see Fig. 6d). Consequently, dendrites under pulsed conditions must pass a longer pathway, hence, require more time until a short-circuit occurs. Due to the absence of grain boundaries, SCs naturally short at higher current density values approaching those of HP under pulsed current conditions. At these current densities, however, 1 MHz pulses are not sufficient anymore to mitigate the build-up of a critical activation front, keeping the CCD unaffected by pulsing. Hence, the application of pulsed currents appears to be particularly powerful for improving the behavior of industrially relevant polycrystalline solid-state electrolytes.

To this date, lithium dendrites remain the weak point of solid-state Li batteries and hinder their implementation in practical electrochemical energy storage[2,3]. In order to overcome the critical current density (CCD) barriers set by industrial researchers (>5 mA/cm^2) and become a competitive option for electric vehicles, different strategies are needed to exceed this limitation. Herein, we demonstrate that the application of 1 MHz-pulsed currents increases the CCD by a factor of six, leading to values as high as 6.5 mA/cm^2, thereby exceeding values reported in literature so far. To understand the origin of this improvement, the preexisting mechanism of Li dendrite formation must be extended. We propose that an enhanced Li-ion activity close to the filament tip arises once Li deposition within a defect is limited by geometrical constraints, which, in turn, causes the effective current density at the crack tip to exceed the exchange current density. The increase in Li activity is accompanied by a lattice expansion that is constrained toward the bulk causing a buildup of elastic energy. Once a critical current has been reached, this energy is released by fracture of the ceramics. Since the buildup of a critical Li-ion activity requires a certain time, the application of current pulses with shorter durations can be used to extend the stability range of the solid-state electrolyte, and therefore increase the achievable CCD. We speculate that a combination of pulsed current waveforms in combination with other established methodologies, like the application of interlayers or increased interfacial surface areas, can significantly boost the performance of solid-state Li batteries.

Methods

Sample preparation

For this study, three different model systems of LLZTO were used. For preliminary tests, e.g., to determine coating and plating behavior and find suitable pulsing parameters, polycrystalline $Li_{6.5}La_3Zr_{1.5}Ta_{0.5}O_{12}$-pellets (PC) were prepared via solid-state synthesis. Therefore, stoichiometric amounts of La_2O_3 (Alfa Aesar, CAS No.1 preheated for 8 h at 900 °C), ZrO_2 (Millipore Sigma, CAS No. 1314-23-4) and Ta_2O_5 (Alfa Aesar, CAS No.1314-61-0) were mixed with LiOH (Alfa Aesar, CAS No.1310-65-2) in 10 wt% excess to account for any Li losses during synthesis. The powder was then wet milled with isopropyl alcohol (Sigma-Aldrich, CAS No.67-63-0; 15 ml) in 100 ml Zr jars with Zr balls for 6 h at 400 rpm. The finished slurry was dried in a Nabertherm oven at 60 °C followed by a calcination step (950 °C, 6 h) in an Al crucible. The sample was again wet milled with isopropyl alcohol (6 h, 400 rpm) to obtain a fine powder and isostatically pressed into green bodies of 10 mm diameter by applying a load of 5 tonnes for 1 min. The pellets were transferred to a Pt crucible, stacked and each covered in calcined power to avoid Li-evaporation. The crucible was again transferred to the oven and subjected to a two-step sintering procedure (950 °C for 0.5 h, 1180 °C for 16 h). A more detailed description of this procedure can be found in ref. 76. For the main cycling experiments hot-pressed, and therefore denser, polycrystalline $Li_{6.4}La_3Zr_{1.4}Ta_{0.6}O_{12}$ (HP) pellets were purchased from Toshima Manufacturing Co., Ltd. Materials System Division. Finally, single crystalline $Li_6La_3Zr_1Ta_1O_{12}$ pellets (SC) were prepared via the Czochralski pulling technique. Composition of the starting melt was stoichiometric with an additional excess of Li_2O of 20 mol%. The raw materials, Li_2CO_3 (99.99% Merck), La_2O_3 (99.999% Fox Chemicals), ZrO_2 (Puratronic© Johnson Matthey), and Ta_2O_5 (99.999% Alfa Aesar) were weighed, mixed, isostatically pressed at 2 kbar, sintered for 6 h at 850 °C, ground, pressed again, and sintered for 6 h at 1230 °C. For the growth process, this starting material was melted in an inductively heated, 40 ml iridium crucible enclosed by alumina ceramic insulation in a pure N_2 ambient environment. After melt homogenization a thick iridium wire was immersed in the melt to initiate crystallization. With some material attached, the wire was slowly pulled upwards ($0.5\,mm\,h^{-1}$) and the generator controlled by the automatic diameter control routine of the pulling station. After the growth was completed, the crystal was withdrawn from the melt and cooled down to room temperature in 15 h. The obtained crystal had a length of 40 mm at a diameter of 15 mm. The single crystals were compressed along a [150] direction which allows a maximum Schmid factor of 0.38 for the <111> {1–10} slip system. The influence of crystal orientation was excluded by cross-check experiments with a compression axis tilted by 45°. Testing in these two directions makes sure that any slip system is oriented with a Schmid factor >0 in at least one experiment.

The polycrystalline pellets were used for proof-of principle and coating experiments, so no special attention was paid to keep the surface roughness and defects to a minimum. Therefore, the cylindrical pellets were simply sanded and polished using up to 4000# grit SiC paper and a polishing cloth (Supplementary Figs. 2a and 4a). The SC and HP samples on the other hand were cut into geometrical cuboids with a diamond saw to obtain dimensions of ~2.7 mm × 3.3 mm × 0.5 mm and 2.3 mm × 2.5 mm × 0.8 mm (width, length, thickness), respectively. Special attention was paid to assure a parallel arrangement of both interface areas (Supplementary Fig. 2b) to avoid stress concentration at elevated regions when clamped into the measuring setup. Afterwards, the samples were glued (with Crystalbond) to a steel ingot for mechanical stabilization and polished in a multi-step mechanical and vibrational polishing procedure. To get rid of any surface contaminants, all samples were finally heat-treated at 450 °C for 3 h (heating rate 5 °C/min) in Argon atmosphere according to a study executed by Sharafi et al.[52] and wiped down with the polishing cloth directly prior to coating.

Coating

In order to achieve good contact between the metal anode and the SSE throughout the whole interface, various Li:M-alloys (M = Sn, Zn, Na) were tested instead of pure Li to improve the wetting behavior and therefore reduce the interfacial resistance. In addition, combinations with Carbon (C-) and Au-interlayers were investigated to check for further improvements (Supplementary Fig. 4c and Supplementary Table 1). All tests were carried out with the PC samples. Interlayers were applied after the final polishing step in an Ar-filled glovebox from Braun (O_2 and H_2O levels below <1 ppm) at (21 ± 1) °C directly prior to application of the Li:M alloy. The C-layer was applied by abrading a pure graphite crucible onto the pellet, whereas the 10 nm-thick Au-layer was sputter-coated in a Leica EM QSG100. The alloys were heated to around 250 °C and the pellet immersed for up to 10 min. Residual Li:M alloy at the sides of the pellet were removed by sanding, such that only the top and bottom sides were coated (see Supplementary Fig. 4b, d, e). While interfacial resistances were comparably low for all alloys, the Li:Sn-alloy stood out the most in terms of success rate and ease of handling, which is why this coating approach was chosen for all later measurements. In case of the SC and HP samples, only the polished sides (Supplementary Fig. 2b, green arrows) were dipped into the Li:Sn bath for around one second.

Physicochemical characterization

For the synthesized polycrystalline and purchased hot-pressed polycrystalline samples, phase purity was checked via powder X-ray diffraction. The measurements were carried out with a Rigaku MiniFlex X-ray diffractometer with a step size of 0.1°/min in a scanning window ranging from 10 to 60° (see Supplementary Fig. 1).

Focused ion beam cross-sectioning and scanning electron microscopy imaging of cracks after failure were carried out using a FEI Helios G4 dual-beam instrument. The samples were placed in a sealed container with Argon atmosphere in the glovebox, transferred to the electron microscope and installed as quickly as possible with an estimated air exposure of 1 min. Additionally, atomic force microscopy measurements were conducted on polished SC and HP samples to analyze their surface roughness. Topography images were acquired with a Cypher ES Atomic Force Microscope from Oxford Instruments (Asylum Research), equipped with a Si cantilever from Budgetsensors (model Tap300GD-G, resonant frequency 300 kHz) and operated in tapping mode under inert gas (Ar).

Operando synchrotron X-ray nanodiffraction studies were carried out at the nanofocus extension of beamline ID13 at the European Synchrotron (ESRF)[77]. Images of the experimental setup can be found in Supplementary Fig. 17. HP samples were placed on microscope slides and mapped by an X-ray beam of 0.09537 nm wavelength ~80 nm in diameter. The region of interest was chosen to include an area of 10 × 10 μm in size placed directly ahead of a growing Li dendrite, identified using an optical microscope. Diffraction patterns from the gauge volume ~80 nm × 80 nm × 80 μm included the diffraction signal from several grains at each mapped position and were collected on a Dectris Eiger X 4 M detector placed 104.9 mm downstream of the sample. Evaluation was performed using the pyFAI[78,79] software package and custom python scripts according to the methods described in refs. 80,81. Compared to the referenced earlier works, the diffraction statistics were poor and therefore the evaluated strains and stresses represent a mixture of second-order (grain-averaged) values and first-order (polycrystal-averaged) values. In the case of the maps presented (Fig. 5) the values for the highlighted grain can be understood to represent second-order strain. The grain stands out from the surrounding material probably due to its comparatively large size.

Electrochemical characterization

Electrochemical impedance spectroscopy measurements were performed with either a Novocontrol Alpha analyzer or a Solartron Modulab ECS XM with an FRA module exhibiting a range of 1 MHz. A 10 mV sinusoidal perturbation signal was applied in a frequency range of 1 MHz to 10 Hz with 10 points per decade after a 1 min open circuit voltage (OCV) period and the resulting signal response of the material was probed. A 10 mV signal was used due to the very small sample geometries present and the concern that galvanostatic electrochemical impedance spectroscopy (GEIS) may lead to Li deposition, especially at lower frequencies. For commercial batteries, which can have much lower impedance due to the large area, GEIS can result in a better signal to noise ratio[82]. Furthermore, it was found that for our specific setup GEIS is more vulnerable to interferences, especially at higher frequencies (see Supplementary Fig. 18). The combination of this led to the use of potentiostatic electrochemical impedance spectroscopy (PEIS).

Cycling under direct and pulsed current conditions (ms-, μs-regime) was conducted with either a Solartron ModuLab XM-unit or a 2450 SourceMeter from Keithley. For the determination of the applied current density, the apparent contact area was used (see Supplementary Note 10 and Supplementary Figs. 19 and 20). Li filament formation and propagation during electrochemical cycling was visually tracked with an optical microscope and images recorded on a 2–7 s period.

The electrochemical impedance spectroscopy measurements, plating proof of concept test and efficiency measurements (see Supplementary Note 6) of the PC-samples were conducted with a two-electrode Swagelok-setup, whereas plating experiments were conducted with a self-assembled coin cell setup as shown in Supplementary Fig. 21a, b. The estimated pressure in these setups is below 1.8 kPa. A homemade setup was also used for the electrochemical characterization of the SC- and HP-samples, where the pellet was clamped between two brass current collectors by means of a screw (see Supplementary Fig. 21c). All regular cycling experiments were conducted with a symmetric cell employing the Li:Sn alloy as both electrodes, whereas in case of the efficiency and plating experiments one side was switched for either Cu or Au, respectively. It should be noted that when contacting the Li:Sn electrodes only around (1.8 ± 0.8) kPa pressure was applied (details see Supplementary Note 2), which is three orders of magnitude lower than what is used during battery assembly[54,83,84] and that all measurements were performed in an Ar-filled glovebox under inert conditions (O_2 and H_2O levels below <1 ppm) at (21 ± 1) °C.

Modeling stress buildup inside a filament under pulsed plating conditions

In modeling the stress buildup within a metal filament, the authors used COMSOL Multiphyics 5.6. A Li metal electrode was modeled using elastic-rate-dependent plastic material behavior. The elastic and plastic material behavior were calibrated using data from Fincher et al.[85]. The elastic modulus was taken as 9.4 GPa, while the rate-dependent plastic behavior was modeled using a Norton Power Law Model, where the strain rate $\dot{\varepsilon}$ is related to the stress σ through Eq. (4):

$$\dot{\varepsilon} = A\left(\frac{\sigma}{\sigma_{ref}}\right)^{n}. \tag{4}$$

Here, σ_{ref} (a reference stress) is taken as 1 MPa, and fitting coefficients A and n were taken as 0.0052 and as 7.04, respectively. The sample was modeled as in the geometry shown in Supplementary Fig. 14, using red boundaries as "roller" boundary conditions. Under such a specification, the displacement normal to a "roller" boundary is set to zero. In this way, the resulting part effectively models a filament against an infinitely stiff solid electrolyte. Such a model would tend to experience larger stress buildups (and thus, potential relaxation) than one with a compliant solid electrolyte.

The temperature within the metal "filament" was prescribed as a function of time such that an equivalent amount of thermal strain was induced to the metal that would otherwise be plated. That is, one can define a "strain-rate" induced by plating as Eq. (5):

$$\dot{\varepsilon} = \frac{\dot{r}}{r_0} = \frac{V_m i}{F r_0}, \tag{5}$$

where F is Faraday's constant, V_m is the molar volume, and r_0 is the initial radius of the filament, r is the radius of the filament and i is the current density. The strain rate can then be defined as a function of time such that the temperature within the filament follows Eq. (6):

$$\dot{\varepsilon} = \frac{V_m i}{F r_0} = \alpha \Delta \dot{T}. \tag{6}$$

Where α is the coefficient of thermal expansion. Thus, by prescribing temperature as a function of time, the strain rate within the filament was controlled to match that of pulsed currents. The elastic energy in the filament was then calculated with Eq. (7) as:

$$\int \sigma : \varepsilon dV, \tag{7}$$

integrated over the body of the filament. The metal filament were meshed with free triangular mesh, for a total of 22,160 elements.

Reporting summary

Further information on research design is available in the Nature Portfolio Reporting Summary linked to this article.

Data availability

The data that support the findings of this study are available from the corresponding author on reasonable request.

References

1. Frith, J. T., Lacey, M. J. & Ulissi, U. A non-academic perspective on the future of lithium-based batteries. *Nat. Commun.* **14**, 420 (2023).
2. Liu, J. et al. Pathways for practical high-energy long-cycling lithium metal batteries. *Nat. Energy* **4**, 180–186 (2019).
3. Shen, Y. et al. Unlocking the energy capabilities of lithium metal electrode with solid-state electrolytes. *Joule* **2**, 1674–1689 (2018).
4. Judez, X. et al. Opportunities for rechargeable solid-state batteries based on Li-intercalation cathodes. *Joule* **2**, 2208–2224 (2018).
5. Albertus, P. et al. Status and challenges in enabling the lithium metal electrode for high-energy and low-cost rechargeable batteries. *Nat. Energy* **3**, 16–21 (2018).

6. Murugan, R., Thangadurai, V. & Weppner, W. Fast lithium ion conduction in garnet-type $Li_7La_3Zr_2O_{12}$. *Angew. Chem. Int. Ed.* **46**, 7778–7781 (2007).
7. Han F. et al. Electrochemical Stability of $Li_{10}GeP_2S_{12}$ and $Li_7La_3Zr_2O_{12}$ Solid Electrolytes. *Adv. Energy Mater.* **6**, 1501590 (2016).
8. Wang C. et al. Garnet-Type Solid-State Electrolytes: Materials Interfaces and Batteries *Chem. Rev.* **120**, 4257–4300 (2020).
9. Krauskopf, T. et al. Toward a fundamental understanding of the lithium metal anode in solid-state batteries—an electrochemo-mechanical study on the garnet-type solid electrolyte $Li_{6.25}Al_{0.25}La_3Zr_2O_{12}$. *ACS Appl. Mater. Interfaces* **11**, 14463–14477 (2019).
10. Kasemchainan, J. et al. Critical stripping current leads to dendrite formation on plating in lithium anode solid electrolyte cells. *Nat. Mater.* **18**, 1105–1111 (2019).
11. Krauskopf, T. et al. Lithium-metal growth kinetics on LLZO garnet-type solid electrolytes. *Joule* **3**, 2030–2049 (2019).
12. Neudecker, B. J., Dudney, N. J. & Bates, J. B. "Lithium-Free" thin-film battery with in situ plated Li anode. *J. Electrochem. Soc.* **147**, 517 (2000).
13. Cao, D. et al. Lithium dendrite in all-solid-state batteries: growth mechanisms, suppression strategies, and characterizations. *Matter.* **3**, 1400993 (2020).
14. He, X. et al. Tuning interface lithiophobicity for lithium metal solid-state batteries. *ACS Energy Lett.* **7**, 131–139 (2021).
15. Liu, B. et al. A simple strategy that may effectively tackle the anode-electrolyte interface issues in solid-state lithium metal batteries. *Chem. Eng. J.* **427**, 131001 (2022).
16. Wei, Y. et al. An oxygen vacancy-rich ZnO layer on garnet electrolyte enables dendrite-free solid state lithium metal batteries. *Chem. Eng. J.* **433**, 133665 (2022).
17. Yang, L. et al. Rapid preparation and performances of garnet electrolyte with sintering aids for solid-state Li–S battery. *Ceram. Int.* **47**, 18196–18204 (2021).
18. Chen, Y. et al. Nanocomposite intermediate layers formed by conversion reaction of SnO_2 for Li/garnet/Li cycle stability. *J. Power Sources* **420**, 15–21 (2019).
19. Liao, Y.-K. et al. Extensively reducing interfacial resistance by the ultrathin Pt layer between the Garnet-type solid-state electrolyte and Li–metal anode. *ACS Appl. Mater. Interfaces* **13**, 56181–56190 (2021).
20. Wan, Z. et al. Three-dimensional alloy interface between $Li_{6.4}La_3Zr_{1.4}Ta_{0.6}O_{12}$ and Li metal to achieve excellent cycling stability of all-solid-state battery. *J. Power Sources* **505**, 230062 (2021).
21. Wang, M., Wolfenstine, J. B. & Sakamoto, J. Temperature dependent flux balance of the Li/$Li_7La_3Zr_2O_{12}$ interface. *Electrochim. Acta* **296**, 842–847 (2019).
22. Chang, W. et al. Evolving contact mechanics and microstructure formation dynamics of the lithium metal-$Li_7La_3Zr_2O_{12}$ interface. *Nat. Commun.* **12**, 1–12 (2021).
23. Zhong, Y. et al. A highly efficient all-solid-state lithium/electrolyte interface induced by an energetic reaction. *Angew. Chem. Int. Ed.* **59**, 14003–14008 (2020).
24. Chandrasekar, M. S. & Pushpavanam, M. Pulse and pulse reverse plating—conceptual, advantages and applications. *Electrochim. Acta* **53**, 3313–3322 (2008).
25. Hasannaeimi, V. & Mukherjee, S. highly catalytic amorphous Ni–P synthesized via pulsed electrodeposition. *Adv. Eng. Mater.* **21**, 1801122 (2019).
26. Allahkaram, S. R., Golroh, S. & Mohammadalipour, M. Properties of Al_2O_3 nano-particle reinforced copper matrix composite coatings prepared by pulse and direct current electroplating. *Mater. Des.* **32**, 4478–4484 (2011).
27. Langsdorf, D. et al. Pulse discharging of sodium-oxygen batteries to enhance cathode utilization. *Energies* **13**, 5650 (2020).
28. Konishi, N. et al. Electrochemical reduction of N_2O on gas-diffusion electrodes. *BCSJ* **69**, 2159–2162 (1996).
29. Yang, H. et al. Effects of pulse plating on lithium electrodeposition, morphology and cycling efficiency. *J. Power Sources* **272**, 900–908 (2014).
30. Grecia, G., Ventosa, E. & Schuhmann, W. Complete prevention of dendrite formation in Zn metal anodes by means of pulsed charging protocols. *ACS Appl. Mater. Interfaces* **9**, 18691–18698 (2017).
31. Xinrong, H. et al. A review of pulsed current technique for lithium-ion batteries. *Energies* **13**, 2458 (2020).
32. Qiao, D. et al. Quantitative analysis of the inhibition effect of rising temperature and pulse charging on lithium dendrite growth. *J. Energy Storage* **49**, 104137 (2022).
33. Sun, X. et al. Revisiting the electroplating process for lithium-metal anodes for lithium-metal batteries. *Angew. Chem. Int. Ed.* **59**, 6665–6674 (2020).
34. Aryanfar, A. et al. Dynamics of lithium dendrite growth and inhibition: pulse charging experiments and Monte Carlo calculations. *J. Phys. Chem.* **5**, 1721–1726 (2014).
35. Li, Q. et al. Understanding the molecular mechanism of pulse current charging for stable lithium-metal batteries. *Sci. Adv.* **3**, e1701246 (2017).
36. Parejiya, A. et al. Improving contact impedance via electrochemical pulses applied to lithium–solid electrolyte interface in solid-state batteries. *ACS Energy Lett.* **6**, 3669–3675 (2021).
37. García, G. et al. Exceeding 6500 cycles for LiFePO4/Li metal batteries through understanding pulsed charging protocols. *J. Mater. Chem. A* **6**, 4746–4751 (2018).
38. Schneider, N. M. et al. Nanoscale evolution of interface morphology during electrodeposition. *Nat. Commun.* **8**, 1–10 (2017).
39. Mayers, M. Z., Kaminski, J. W. & Miller, T. F. III Suppression of dendrite formation via pulse charging in rechargeable lithium metal batteries. *J. Phys. Chem.* **116**, 26214–26221 (2012).
40. Wang, D. et al. Synchronous healing of Li metal anode via asymmetrical bidirectional current. *Iscience* **23**, 100781 (2020).
41. Parejiya, A. et al. Electrochemical healing of dendrites in garnet-based solid electrolytes. *ACS Energy Lett.* **5**, 3368–3373 (2020).
42. Qu, Z. G., Jiang, Z. Y. & Wang, Q. Experimental study on pulse self–heating of lithium–ion battery at low temperature. *Int. J. Heat. Mass Transf.* **135**, 696–705 (2019).
43. Li, L. et al. Self-heating–induced healing of lithium dendrites. *Science* **359**, 1513–1516 (2018).
44. Lu, Y. et al. Critical current density in solid-state lithium metal batteries: mechanism, influences, and strategies. *Adv. Funct. Mater.* **31**, 2009925 (2021).
45. Flatscher, F. et al. The natural critical current density limit for $Li_7La_3Zr_2O_{12}$ garnets. *J. Mater. Chem. A* **8**, 15782–15788 (2020).
46. Porz, L. et al. Mechanism of lithium metal penetration through inorganic solid electrolytes. *Adv. Energy Mater.* **7**, 1701003 (2017).
47. Swamy, T. et al. Lithium metal penetration induced by electrodeposition through solid electrolytes: example in single-crystal $Li_6La_3ZrTaO_{12}$ garnet. *J. Electrochem. Soc.* **165**, A3648 (2018).
48. Cheng, L. et al. Effect of surface microstructure on electrochemical performance of garnet solid electrolytes. *ACS Appl. Mater. Interfaces* **7**, 2073–2081 (2015).
49. Wachter-Welzl, A. et al. Microelectrodes for local conductivity and degradation measurements on Al stabilized $Li_7La_3Zr_2O_{12}$ garnets. *J. Electroceram.* **38**, 176–181 (2017).
50. Wachter-Welzl, A. et al. The origin of conductivity variations in Al-stabilized $Li_7La_3Zr_2O_{12}$ ceramics. *Solid State Ion.* **319**, 203–208 (2018).
51. Popov, K. et al. *Fundamental Aspects of Electrometallurgy The Current Distribution in Electrochemical Cells* 101–143 (Kluwer Academic, Boston, 2016).

52. Sharafi, A. et al. Surface chemistry mechanism of ultra-low interfacial resistance in the solid-state electrolyte $Li_7La_3Zr_2O_{12}$. *Chem. Mater.* **29**, 7961–7968 (2017).
53. Wang, C. et al. Universal soldering of lithium and sodium alloys on various substrates for batteries. *Adv. Energy Mater.* **8**, 1701963 (2018).
54. Wang, M. J., Choudhury, R. & Sakamoto, J. Characterizing the Li-solid-electrolyte interface dynamics as a function of stack pressure and current density. *Joule* **3**, 2165–2178 (2019).
55. Huang, X. et al. None-mother-powder method to prepare dense Li-garnet solid electrolytes with high critical current density. *ACS Appl. Energy Mater.* **1**, 5355–5365 (2018).
56. Zheng, C. et al. Grain boundary modification in garnet electrolyte to suppress lithium dendrite growth. *Chem. Eng. J.* **411**, 128508 (2021).
57. Guo, H. et al. Achieving high critical current density in Ta-doped $Li_7La_3Zr_2O_{12}$/MgO composite electrolytes. *J. Alloy. Compd.* **856**, 157222 (2021).
58. Cai, M. et al. Robust conversion-type Li/Garnet interphases from metal salt solutions. *Chem. Eng. J.* **417**, 129158 (2021).
59. Lu, G. et al. Universal lithiophilic interfacial layers towards dendrite-free lithium anodes for solid-state lithium-metal batteries. *Sci. Bull.* **66**, 1746–1753 (2021).
60. Ruan, Y. et al. A 3D cross-linking lithiophilic and electronically insulating interfacial engineering for garnet-type solid-state lithium batteries. *Adv. Funct. Mater.* **31**, 2007815 (2021).
61. Park, R. J.-Y. et al. Semi-solid alkali metal electrodes enabling high critical current densities in solid electrolyte batteries. *Nat. Energy* **6**, 314–322 (2021).
62. He, X. et al. Cu-doped alloy layer guiding uniform Li deposition on a Li–LLZO interface under high current density. *ACS Appl. Mater. Interfaces* **13**, 42212–42219 (2021).
63. Hitz, G. T. et al. High-rate lithium cycling in a scalable trilayer Li-garnet-electrolyte architecture. *Mater. Today* **22**, 50–57 (2019).
64. Kazyak, E. et al. Li penetration in ceramic solid electrolytes: operando microscopy analysis of morphology, propagation, and reversibility. *Matter* **2**, 1025–1048 (2020).
65. Krauskopf, T. et al. The fast charge transfer kinetics of the lithium metal anode on the garnet-type solid electrolyte $Li_{6.25}Al_{0.25}La_3Zr_2O_{12}$. *Adv. Energy Mater.* **10**, 2000945 (2020).
66. Porz, L. et al. Characterizing brittle fracture by modeling crack deflection angles from the microstructure. *J. Am. Ceram. Soc.* **98**, 3690–3698 (2015).
67. Han, F. et al. High electronic conductivity as the origin of lithium dendrite formation within solid electrolytes. *Nat. Energy* **4**, 187–196 (2019).
68. Cheng, E. J., Sharafi, A. & Sakamoto, J. Intergranular Li metal propagation through polycrystalline $Li_{6.25}Al_{0.25}La_3Zr_2O_{12}$ ceramic electrolyte. *Electrochim. Acta* **223**, 85–91 (2017).
69. Bekheet, M.F. et al. On the structural stability of crystalline ceria phases in undoped and acceptor-doped ceria materials under in situ reduction conditions. *CrystEngComm.* **21(1)**, 145–154 (2019).
70. Wang, H. et al. TEM study of electrochemical cycling-induced damage and disorder in $LiCoO_2$ cathodes for rechargeable lithium batteries. *J. Electrochem. Soc.* **146**, 473 (1999).
71. Limthongkul, P. et al. Electrochemically-driven solid-state amorphization in lithium–metal anodes. *J. Power Sources.* **119**, 604–609 (2003).
72. Yılmaz, I. Gypsum/anhydrite: some engineering problems. *Bull. Eng. Geol. Environ.* **60**, 227–230 (2001).
73. Usiskin, R. E. & Maier, J. Guidelines for optimizing the architecture of battery insertion electrodes based on the concept of wiring lengths. *Phys. Chem. Chem. Phys.* **20**, 16449–16462 (2018).
74. Bai, P. et al. Transition of lithium growth mechanisms in liquid electrolytes. *Energy Environ. Sci.* **9**, 3221–3229 (2016).
75. Pang, Q. et al. An in vivo formed solid electrolyte surface layer enables stable plating of Li metal. *Joule* **1**, 871–886 (2017).
76. Badami, P. et al. Highly conductive garnet-type electrolytes: access to $Li_{6.5}La_3Zr_{1.5}Ta_{0.5}O_{12}$ prepared by molten salt and solid-state methods. *ACS Appl. Mater. Interfaces* **12**, 48580–48590 (2020).
77. Flatscher, F., Todt, J., Gawlitza, P. & Niese, S. Scanning and in-situ MLL development for X-ray nanodiffraction on thin film, space and additively manufactured applications [Data set]. European Synchrotron Radiation Facility. https://doi.org/10.15151/ESRF-ES-778016223 (2025).
78. Ashiotis, G. et al. The fast azimuthal integration Python library: pyFAI. *J. Appl. Crystallogr.* **48**, 510–519 (2015).
79. Kieffer, J. et al. New tools for calibrating diffraction setups. *J. Synchrotron Radiat.* **27**, 558–566 (2020).
80. Keckes, J. et al. X-ray nanodiffraction reveals strain and microstructure evolution in nanocrystalline thin films. *Scr. Mater.* **67**, 748–751 (2012).
81. Keckes, J. et al. 30 nm X-ray focusing correlates oscillatory stress, texture and structural defect gradients across multilayered TiN-SiOx thin film. *Acta Mater.* **144**, 862–873 (2018).
82. Meddings, N. et al. Application of electrochemical impedance spectroscopy to commercial Li-ion cells: a review. *J. Power Sources* **480**, 228742 (2020).
83. Cannarella, J. & Craig, B. A. Stress evolution and capacity fade in constrained lithium-ion pouch cells. *J. Power Sources* **245**, 745–751 (2014).
84. Bonnick, P. & Dahn, J. R. A simple coin cell design for testing rechargeable zinc-air or alkaline battery systems. *J. Electrochem. Soc.* **159**, A981 (2012).
85. Fincher, C. D. et al. Mechanical properties of metallic lithium: from nano to bulk scales. *Acta Mater.* **186**, 215–222 (2020).

Acknowledgements

D.R. acknowledges financial support by the Austrian Federal Ministry for Digital and Economic Affairs, the National Foundation for Research, Technology and Development and the Christian Doppler Research Association (Christian Doppler Laboratory for Solid-State Batteries). Moreover, V.R. would like to thank the Austrian Marshall Plan Foundation for sponsoring parts of this project. P.F. and M.L.-M. acknowledge the European Research Council under the European Union’s Horizon 2020 Program (FP/2014–2020)/ERC Grant Agreement (771834—POPCRYSTAL). The CSnanoXRD experiments were performed on beamline ID13 at the European Synchrotron Radiation Facility (ESRF), Grenoble, France. We are grateful to Manfred Burghammer at the ESRF for providing assistance in using beamline ID13 and to Pavan Badami at Argonne National Laboratory for providing calcined LLZTO powder for preliminary test measurements.

Author contributions

D.R. designed the project. D.R., L.P., V.R. and F.F. performed the experimental work. S.G. synthesized the single crystals, Y.-M.C. and C.F. performed finite element calculations. S.W. performed the FIB SEM measurements. F.F. and J.T. performed the CS Nano XRD measurements with help from J.K. J.T. and J.K. analyzed the CS Nano XRD data M.L.-M. performed the AFM measurements with assistance from F.F. and the AFM data analysis with help from P.F. D.R. supervised the work. D.R., J.F., V.R. and F.F. wrote the first draft of the manuscript with discussion and feedback from I.H. and V.H. All authors contributed to the final draft.

Funding

Open access funding provided by Norwegian University of Science and Technology.

Competing interests

The authors declare no competing interests.

Additional information

Supplementary information The online version contains supplementary material available at https://doi.org/10.1038/s41467-023-37476-y.

Correspondence and requests for materials should be addressed to D. Rettenwander.

Peer review information *Nature Communications* thanks the other anonymous reviewer(s) for their contribution to the peer review of this work. Peer review reports are available.

Supplementary Information

Effect of pulse-current-based testing protocols on the lithium dendrite formation and evolution in all-solid-state batteries

V. Reisecker[a,b#], F. Flatscher[b,c#], L. Porz[c], C. Fincher[d], J. Todt[e], I. Hanghofer[f], V. Hennige[f], M. Linares-Moreau[g], P. Falcaro[g], S. Ganschow[h], S. Wenner[i], Y.M. Chiang[d], J. Keckes[e], J. Fleig[j], D. Rettenwander[a,b,c*]

[a] Institute of Chemistry and Technology of Materials, Graz University of Technology, Graz, Austria.
[b] Christian Doppler Laboratory for Solid-State Batteries, NTNU Norwegian University of Science and Technology, Trondheim, Norway.
[c] Department of Material Science and Engineering, NTNU Norwegian University of Science and Technology, Trondheim, Norway.
[d] Department of Materials Science & Engineering, Massachusetts Institute of Technology, Cambridge, MA, USA
[e] Department of Materials Physics, Montanuniversität Leoben and Erich Schmid Institute for Materials Science, Austrian Academy of Sciences, Leoben 8700, Austria
[f] AVL List GmbH, Graz, Austria
[g] Institute of Physical and Theoretical Chemistry, Graz University of Technology, Graz, Austria
[h] Leibniz-Institut für Kristallzüchtung, Berlin, Germany
[i] Sintef Industry, Department of Materials and Nanotechnology, Trondheim, Norway
[j] Institute of Chemical Technologies and Analytics, TU Wien, Vienna, Austria

[#]Authors, V. Reisecker and F. Flatscher, equally contributed to this work.
[*]Corresponding author: daniel.rettenwander@ntnu.no

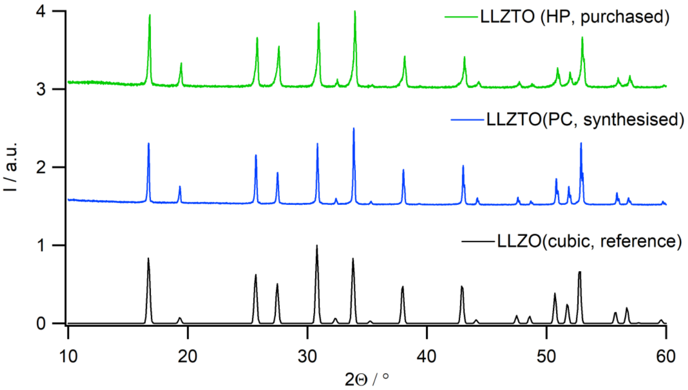

Supplementary Fig. 1: XRD data of polycrystalline samples. Obtained X-Ray Diffraction patterns of polycrystalline $Li_{6.5}La_3Zr_{1.5}Ta_{0.5}O_{12}$ synthesized via solid-state route (PC, blue) and polycrystalline hot-pressed (HP, green) $Li_{6.4}La_3Zr_{1.4}Ta_{0.6}O_{12}$ in comparison to cubic $Li_7La_3Zr_2O_{12}$ from ICSD (#422259, black).

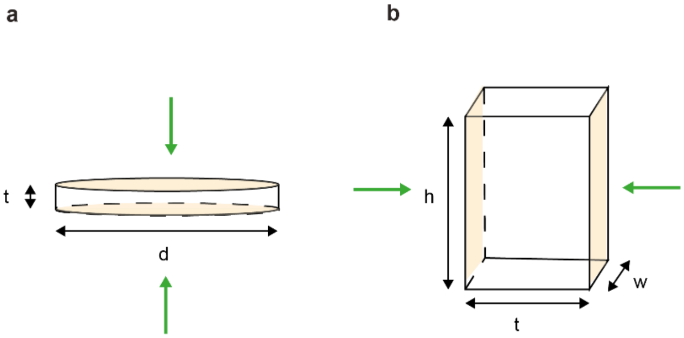

Supplementary Fig. 2: Geometries of samples. Schematics illustrating a typical cylindrical PC pellet (a) and a SC/HP cuboid (b). The polished and heat-treated surface areas are highlighted in orange, which in the end were coated with a molten Li:Sn alloy as indicated by the green arrows.

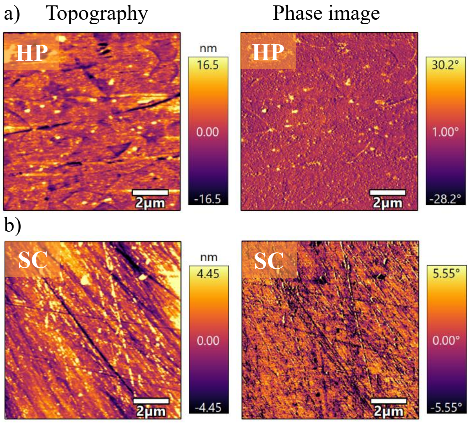

Supplementary Fig. 3: AFM results of samples. Atomic Force Microscopy analyses were conducted to assess the roughness and defect concentration of the SC (a) and HP (b) surfaces. Both topography images reveal scratches on the polished electrolyte surface. The depth of these scratches is, however, lower for the SC (a) than for the HP (b) pellet, denoting a lower surface roughness (see height profiles in Figure 1c). Average RMS surface roughness was calculated from these measurements and resulted in (3 ± 1) nm and (8 ± 3) nm, for SC and HP respectively.

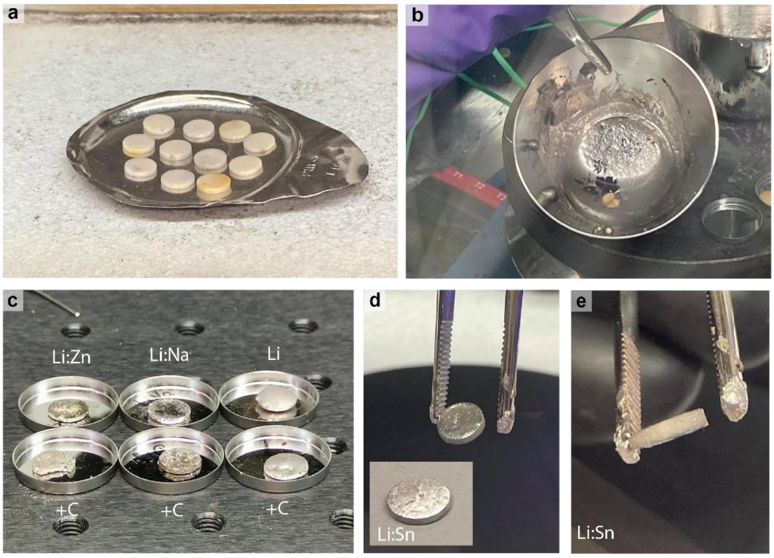

Supplementary Fig. 4: Coating approaches of pellets. (a) finished PC samples after the polishing and heat treatment. (b) PC pellet half immersed in the Li:Sn alloy when heated up to 250 °C in a Pt-crucible. (c) Comparison of the Li:alloy wetting capabilities of some different coating approaches tested. The Li/Zn alloy contained 5mol% Zn and the Li/Na alloy 21.4mol% Na, +C denotes the use of a carbon interlayer. (d,e) Images of a PC pellet completely coated with the Li:Sn alloy.

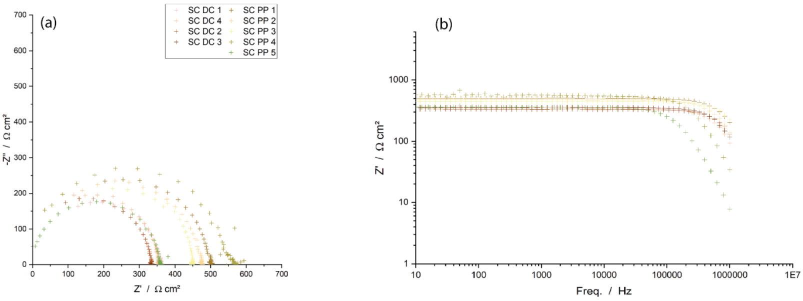

Supplementary Fig. 5: EIS data of SC samples. (a) Impedance data of the SC samples in a Li|SC|Li cell measured at 21±1°C measured prior to direct current (DC) or pulse plating (PP) experiments along with the respective (b) Bode plots.

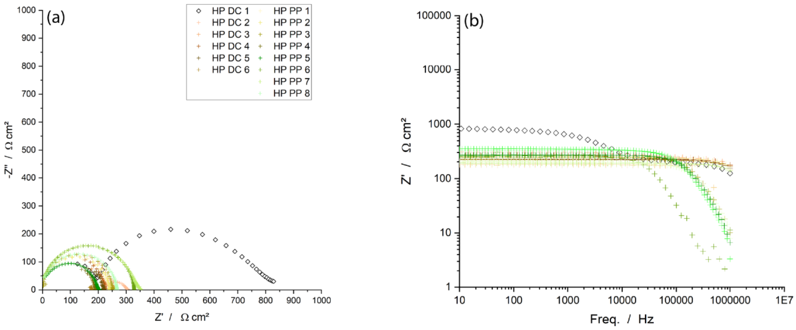

Supplementary Fig. 6: EIS data of HP samples. (a) Impedance data of the HP samples in a Li|HP|Li cell measured at 21±1°C prior to direct current (DC) or pulse plating (PP) experiments along with the respective (b) Bode plots. HP DC 1 (black marker) represents a non-heat-treated sample and HP DC 2 did not undergo a proper polishing sequence which demonstrates the importance of a proper sample treatment prior to coating.

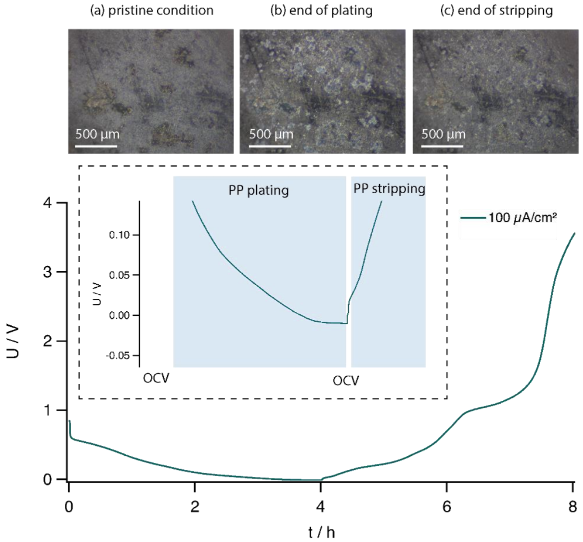

Supplementary Fig. 7: Plating experiments of polycrystalline samples. Plating profile of a PC sample coated with Au on one side and Li:Sn on the other, in a Li|PC|Au cell treated at 1:1 µs pulse pause (PP) ratio at 100 µA/cm^2 at 21±1°C.The close-up inspection window shows the switch from the plating to the stripping step and the open circuit voltage (OCV) in between. In situ Optical Microscopy images on top show the surface of the Au electrode in its pristine condition (a) and confirm Li is being plated at the opposing Au electrode (b) and stripped again in the subsequent half cycle (c).

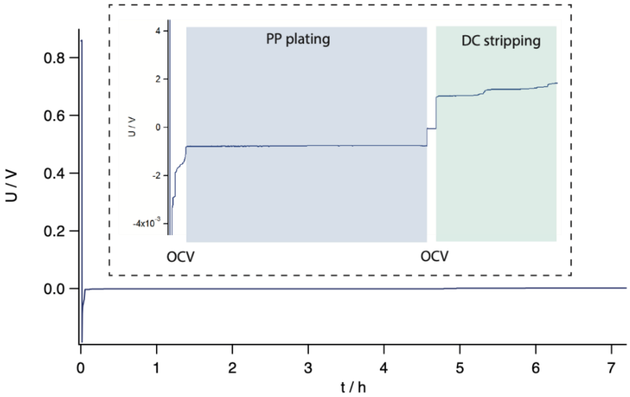

Supplementary Fig. 8: Efficiency experiments of polycrystalline samples. Voltage profile of a PC-sample in a Li|PC|Au cell undergoing an efficiency measurement where 200 µAh/cm^2 of lithium are plated at 50 µA/cm^2 pulsed current application (again 1:1 µs pulse pause ratio, PP) and subsequently stripped with direct current (DC) application at 21±1°C. A close-up inspection window shows the switch from the PP plating step to the direct current stripping step and the open circuit voltage (OCV) in between.

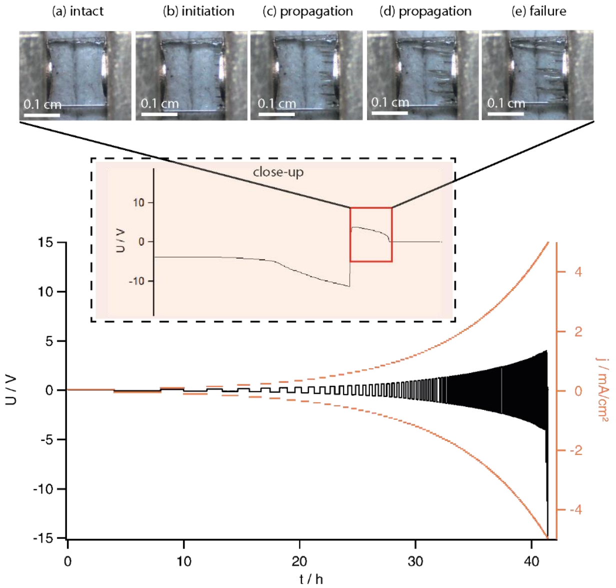

Supplementary Fig. 9: Cycling performance of SC sample. Cycling profile of the SC sample measured in a Li|SC|Li cell at 21±1°C (a, intact state) which achieved the highest effective CCD value during this study being (4.59 ± 0.05) mA/cm^2 after application of a direct current program. A close-up inspection window and simultaneously taken in situ Optical Microscopy images of the SC at the top show failure. First, the voltage increases drastically, presumably due to contact loss from void formation. In the subsequent plating step, the voltage response drops as the lithium filaments initiate (b) and propagate through the SC (c-d) until the cell fails (e).

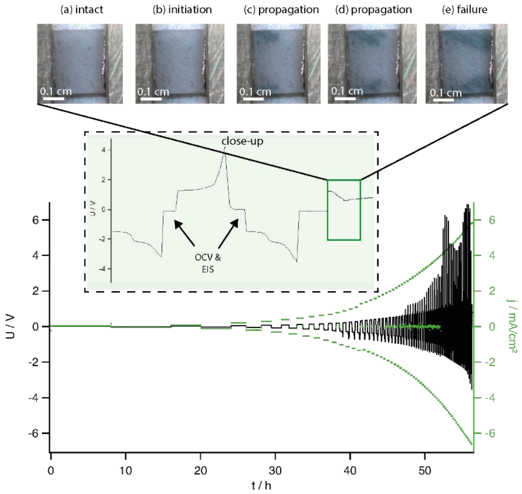

Supplementary Fig. 10: Cycling performance of HP sample. Cycling profile of the HP sample measured in a Li|HP|Li cell at 21±1°C (a, intact state) which achieved the highest CCD during this study being (6.6 ± 0.1) mA/cm^2 after application of a 1:1 (µs) pulsed current program. In contrast to the direct current program, here, 10 mV perturbation Potentiostatic Electrochemical Impedance measurements from 1 MHz to 10 Hz with 1 minute OCV were performed in between half-cycles . Again, a close-up inspection window along with simultaneously taken in situ Optical Microscopy images of the HP at the top show the dropping voltage response as the lithium filaments initiate (b) and propagate through the HP (c-d) until the cell fails (e).

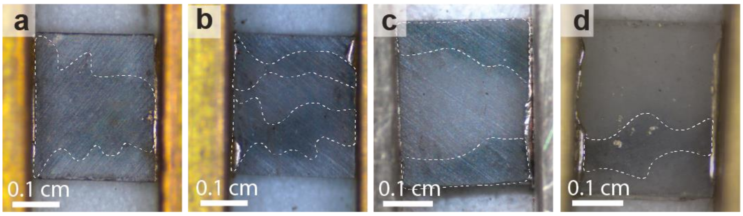

Supplementary Fig. 11: Typical dendrite growth in HP samples. In situ Optical Microscopy images of a selection of failed HP samples. Note that, in contrast to the SC samples, where mostly single dendrites were observed, the filaments in the HP samples rather showed an areal growth. An example of such a dendrite growth can be found in Supplementary Video 5 showing sample (c).

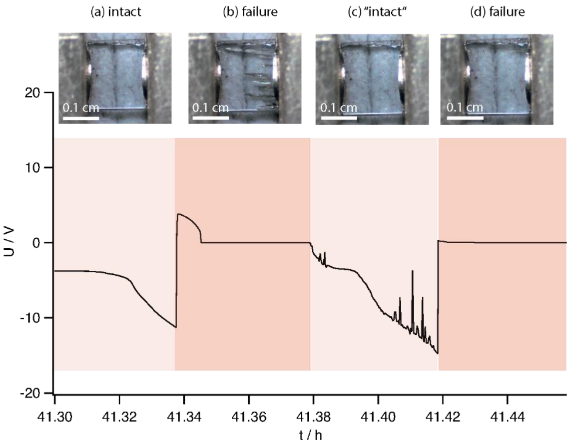

Supplementary Fig. 12: Reversibility of Li dendrites. Voltage profile of an SC sample, measured in a Li|SC|Li cell at 21±1°C, treated with a direct current cycling program combined with in situ Optical Microscopy images. It shows the rarely encountered peculiar behavior, that at high currents a dendrite can seemingly retract to an apparently intact sample. After short circuiting for the first time, which happens after the switch of current from (a) to (b), the lithium filaments apparently form back in the following half-cycle (c), and the sample appears to be optically and electrically intact again. In the subsequent half-cycle, a Li filament once more grows through the upper area of the SC and short-circuits the sample for good this time (d). This process can be seen in motion in Supplementary Video 4.

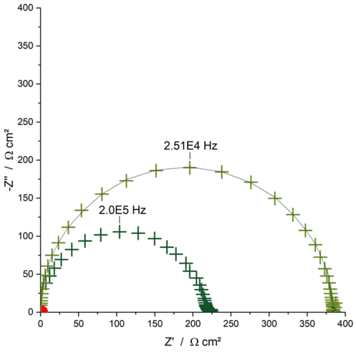

Supplementary Fig. 13: **Proof of Li filament reversibility.** Measured impedance responses of an SC sample in a Li|SC|Li cell at 21±1°C prior to failure (grey markers representing older cycles, green markers the last cycle prior to first failure), once short-circuited (light red) and after the Li filaments formed back completely (dark red). In the subsequent half-cycle, the sample then shorts again (light red).

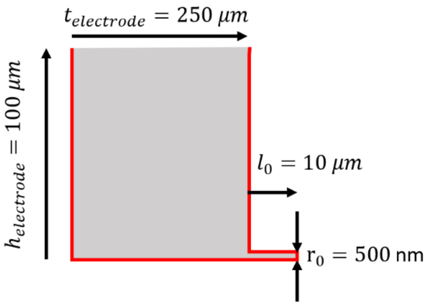

Supplementary Fig. 14: COMSOL modelling of Li penetration. Model used for the COMSOL Multiphysics finite element analysis to study the deformation of an expanding metal filament. The thickness $t_{electrode}$ and height $h_{electrode}$ of the metal electrode were set to 250 µm and 100 µm, respectively and the length of the formed metal filament l_o was assumed to have a length of 10 µm. The "roller" boundary conditions are marked in red.

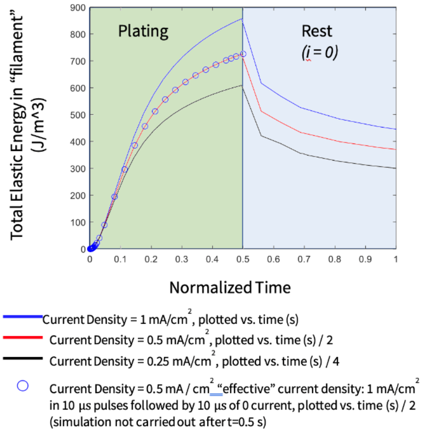

Supplementary Fig. 15: Analysis of total elastic energy evolution. The total elastic energy in the "filament" plotted as a function of normalized time when Li metal is being plated (green region) and when the current is switched off during a pausing time (blue region).

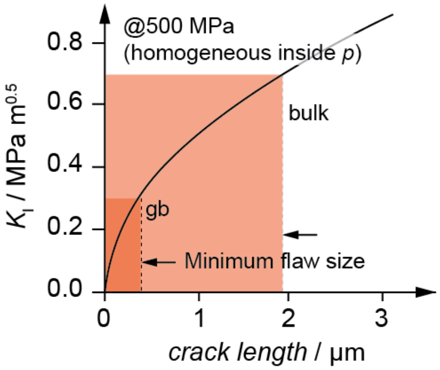

Supplementary Fig. 16: Fracture stress intensity factor K_I as a function of the defect length (crack). The minimum flaw size for a grain boundary (gb) and a grain are shown for a randomly chosen critical stress intensity factor of 500 MPa, assumed as a homogeneous pressure p inside (arbitrarily chosen as the real value is not known so far).

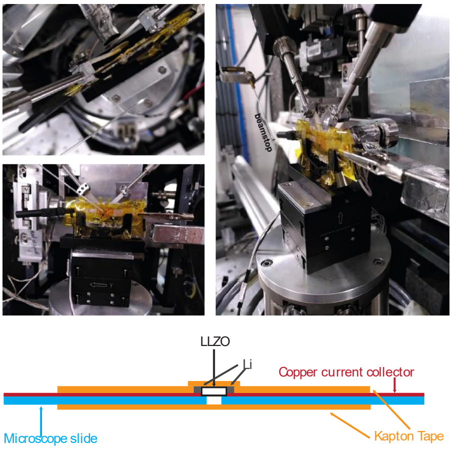

Supplementary Fig. 17: Setup used for nanoXRD studies. Images of the setup used for the nanoXRD study at the beamline ID13 at the ESRF. An HP sample is placed on a microscope slide coated with Li:Sn contacting a Cu current collector. A small opening below the sample helps to reduce interaction of the slide with the beam. The whole sample is encapsulated in Kapton tape to protect the Li from air and moisture. A schematic sideview of the setup is shown at the bottom. The X-ray optics are placed behind the sample in the beam path to focus the beam down to a spot size of 30 nm. The measurement was done at a temperature of 22°C.

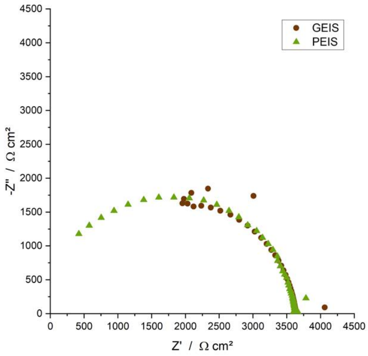

Supplementary Fig. 18: EIS data comparison of GEIS and PEIS mode. Nyquist plot comparing a 10 mV Potentiostatic Electrochemial Impedance Spectroscopy (PEIS) measurement (green) to a 1 µA Galvanostatic Electrochemical Impedance Spectroscopy (GEIS) measurement (orange) done on a Li:Sn-coated HP sample in a Li|HP|Li cell at 21±1°C. Frequencies were varied from 1 MHz to 1 Hz. Except for the inductive loop at high frequency parts for the GEIS measurement similar results are obtained.

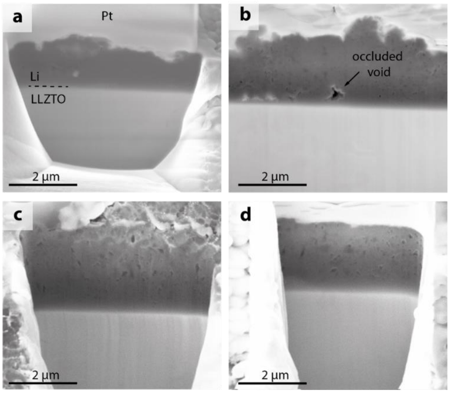

Supplementary Fig. 19: SEM images of FIB cuts performed at an HP|Li interface, at two different positions. In both cases, the Li electrode was coated afterwards with a protective Pt layer at the cut position for imaging purposes. Images were taken at 10 kV and 0.69 nA (a,b) or 0.17 nA (c,d) at a working distance of 4.1 mm. The HP sample treated with direct current is shown in subfigures a and b and was cycled until failure at 21±1°C (200 µA/cm²). Subfigures c and d show the interface of the HP sample cycled with pulsed currents until it reached the same current density as the sample treated with direct current. No significant difference becomes apparent as both interface regions show occluded voids and an intimate contact between LLZTO and Li. Therefore, it can be assumed that the deposition of Li, as expected, works smoothly with pulsed currents.

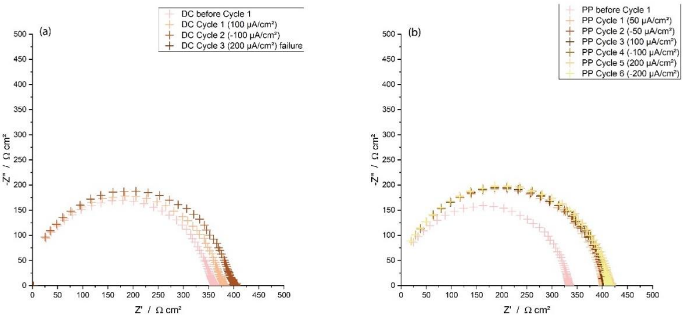

Supplementary Fig. 20: EIS data of HP samples. (a) Nyquist plot showing the impedance evolution of an HP sample cycled in a Li|HP|Li cell at 21±1°C with direct current (DC) until failure. (b Nyquist plot showing the impedance evolution of an HP sample cycled in a Li|HP|Li cell at 21±1°C with pulsed current application (PP) until the same current density as the sample in (a).

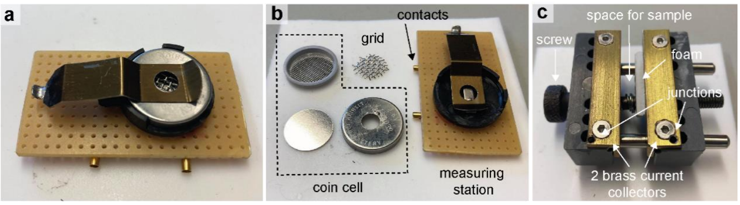

Supplementary Fig.21: Self-assembled setups used for electrochemical characterization.(a,b) Homemade setup for the plating experiments consisting of a measuring station and a coin cell that can hold a PC pellet and a top grid as current collector. (c) Measuring setup used for the cycling and efficiency experiments of the SC and HP samples consisting of two parallel aligned brass current collectors equipped with a junction and a white foam in the middle to help with filament tracking. A screw is used for adjusting the distance to the respective sample.

Supplementary Tab. 1: Listing of the different coating approaches pursued during this study along with the formulation used for preparation of the alloy, tested interlayers (carbon or gold) and a final qualitative rating ranging from – (worst case), over ~ (satisfactory) to + (best case). While the Li:M alloys were applied via dipping the specimen into a molten bath, interlayers were applied prior by abrading a pure graphite crucible onto the sample or sputtering (Au target). The Li:Sn alloy (marked in blue) was finally chosen as the go to coating strategy for all later measurements.

approach	recipe	tested interlayers	rating
Li	pure Li metal	C, Au	-
Li:Sn	Li metal + 30 wt% Sn powder	C	+
Li:Na	Li metal + 21.4 mol% Na metal	C	~
Li:Zn	Li metal + 5 mol% Zn powder	C	~

Supplementary Tab. 2: Listing of PC samples treated with either direct or pulsed current conditions (ms and µs range) in a symmetric Li||Li cell along with their measured ASR and CCD values at 21±1°C. The effective CCD (CCD_{eff}) represents the CCD after consideration of the capacity decrease and the step size taken in the cycling protocol is additionally given for uncertainty estimation.

sample	Conditions	ASR	CCD	CCD_{eff}	step
		Ω cm^2	µA/cm^2	µA/cm^2	µA/cm^2
PC DC 1	DC	*	250	250	50
PC DC 2	DC	*	20	20	5
PC DC 2	DC	*	325	325	5
PC PP 1	1:1 (ms)	4.4	400	200	200
PC PP 2	1:2 (ms)	1.5	600	200	200
PC PP 3	1:3 (ms)	34.1	600	150	200
PC PP 4	1:5 (ms)	60.8	600	100	200
PC PP 5	1:10 (ms)	19.1	1200	109	200
PC PP 6	1:1 (µs)	6.6	1200	600	200
PC PP 7	1:2 (µs)	8.8	2000	667	200
PC PP 8	1:2 (µs)	8.7	800	267	200
PC PP 9	1:3 (µs)	10.5	600	150	200
PC PP 10	1:3 (µs)	10.3	1800	450	200

* no data available

Supplementary Tab. 3: Listing of SC samples treated with either direct or pulsed current conditions (µs range) in a symmetric Li||Li cell along with their measured ASR and CCD values at 21±1°C. The effective CCD (CCD_{eff}) represents the CCD after consideration of the capacity decrease and the step size taken in the cycling protocol is additionally given for uncertainty estimation.

sample	conditions	ASR	CCD	CCD_{eff}	step
		Ω cm²	µA/cm²	µA/cm²	µA/cm²
SC DC1	DC	140.3	250	250	250
SC DC 2	DC	115.4	400	400	200
SC DC 3	DC	44.9	400	400	200
SC DC 4	DC	-	1250	1250	50
SC DC 5	DC	-	800	800	50
SC DC 6	DC	-	3900	3900	50
SC DC 7	DC	-	4950	4950	50
SC PP 1	1:1 (µs)	-	3530	1765	100
SC PP 2	1:1 (µs)	-	1600	800	100
SC PP 3	1:1 (µs)	-	2340	1170	100
SC PP 4	1:1 (µs)	-	900	450	100
SC PP 5	1:1 (µs)	-	1100	550	100
SC PP 6	1:1 (µs)	-	4800	2400	100

Supplementary Tab. 4: Listing of HP samples treated with either direct or pulsed current conditions (µs range) in a symmetric Li||Li cell along with their measured ASR and CCD values at 21±1°C. The effective CCD (CCD$_{eff}$) represents the CCD after consideration of the capacity decrease and the step size taken in the cycling protocol is additionally given for uncertainty estimation.

sample	conditions	ASR	CCD	CCD$_{eff}$	step
		Ω cm²	µA/cm²	µA/cm²	µA/cm²
HP DC 1	DC	704.1	200	200	100
HP DC 2	DC	86.0	500	500	50
HP DC 3	DC	51.4	650	650	50
HP DC 4	DC	-	1050	1050	50
HP DC 5	DC	-	400	400	50
HP DC 6	DC	-	450	450	50
HP PP 1	1:1 (µs)	*	2100	1050	100
HP PP 2	1:1 (µs)	-	6600	3300	100
HP PP 3	1:1 (µs)	-	1350	675	100
HP PP 4	1:1 (µs)	-	2750	1375	100
HP PP 5	1:1 (µs)	-	3200	1600	100
HP PP 6	1:1 (µs)	-	2100	1050	100
HP PP 7	1:1 (µs)	-	4800	2400	100

* no data available

Supplementary Tab. 5: List of all CCD values found in literature for LLZO being above 1 mA/cm². Besides the stoichiometric composition, also the category of improvement (alloy, additive, interface engineering) as well as the cycling conditions (T, p) and pellet quality (density, ASR) are given if mentioned in literature. Rows marked in red are measurements carried out at an elevated temperature and/or pressure and are therefore unfit for direct comparison to the rest of the CCD values.

CCD	composition	additive	alloy	interface	T	p	density	ASR	Ref
mA/cm²					°C		%	Ω cm^2	
1.1	$Li_{6.5}La_3Zr_{1.5}Ta_{0.5}O_{12}$	-	-	PbO/ZnO/ Co_3O_4	RT	-	-	10	1
1.1	$Li_{6.4}La_3Zr_{1.4}Ta_{0.6}O_{12}$	-	-	CoO/Li_2O	25	?	95	12.3	2
1.15	$Li_{6.4}La_3Zr_{1.4}Ta_{0.6}O_{12}$	15 wt% excess $LiOH{\cdot}H_2O$	-	Li_xSn:Li_2O	RT	10 N cm^{-2}	-	25	3
1.15	$Li_{6.4}La_3Zr_{1.4}Ta_{0.6}O_{12}$	excess lithium	-	Au	25	-	~96%	3	4
1.2	$Li_{6.5}La_3Zr_{1.5}Ta_{0.5}O_{12}$	-	-	SnS_2	100	Swagelok	-	17	5
1.2	$Li_{6.5}La_3Zr_{1.5}Nb_{0.5}O_{12}$	Li_3PO_4 + 10 wt% excess $LiOH.H_2O$	-	-	RT	-	90.9	-	6
1.3	$Li_{6.5}La_3Zr_{1.5}Ta_{0.5}O_{12}$	-	-	Sr:Li	RT	-	-	-	7
1.4	Ta-doped LLZO	excess $LiOH{\cdot}H_2O$	-	O_V-ZnO and Au?	RT	-	-	55	8
1.4	$Li_{6.75}La_3Zr_{1.75}Ta_{0.25}O_{12}$	-	-	Pt	RT	coin cell	-	9	9
1.4	$Li_{6.5}La_3Zr_{1.5}Ta_{0.5}O_{12}$	$Li_6Zr_2O_7$	-	Au	25	coin cell	97.21	1.65	10
1.7	$Li_{6.4}La_3Zr_{1.4}Ta_{0.6}O_{12}$	-	Li:Mo (α-MoO_3 nanobelts)	-	RT	-	-	1	11
1.7	$Li_{6.4}La_3Zr_{1.4}Ta_{0.6}O_{12}$ (nm-sized)	Al_2O_3	-	Au	60	Micro-clamp	98.5	129.4	12
1.8	$Li_{6.5}La_3Zr_{1.5}Ta_{0.5}O_{12}$	-	-	LiF:LiCl	25	-	>96	110	13
1.95	$Li_{6.5}La_3Zr_{1.5}Ta_{0.5}O_{12}$	4 wt% MgO	-	Au	25	-	97.9	18	14
2	$Li_{6.4}La_3Zr_{1.4}Ta_{0.6}O_{12}$	-	-	PZL	RT	30 MPa	-	1.9	15
2.2	$Li_{6.5}La_3Zr_{1.5}Ta_{0.5}O_{12}$	-	-	MoS_2	100	-	-	14	16
2.8	$Li_{6.5}La_3Zr_{1.5}Ta_{0.5}O_{12}$	-	-	Cu doped Li_3Zn	28	coin cell	98	30	17
3.8	$Li_{6.25}Al_{0.25}La_3Zr_2O_{12}$ $Li_{6.5}Al_{0.15}La_3Zr_{1.5}Ta_{0.5}O_{12}$	-	-	Au	40	3.3 MPa	>99	9–15	18
6					60	3.3 MPa	>99	9–15	18
4	$Li_{6.4}La_3Zr_{1.4}Ta_{0.6}O_{12}$	-	-	ZNR	RT	-	-	-	19
6.5	$Li_{6.4}La_3Zr_{1.4}Ta_{0.6}O_{12}$	-	Li:Sn	-	21 ± 1	<(1.8 ± 0.8) kPa	>99	-	This study
10	$Li_{6.75}La_{2.75}Ca_{0.25}Zr_{1.5}Nb_{0.5}O_{12}$	-	-		RT	button cell	>99	7	20

Supplementary Note 1: Ion conductivity and area specific resistance

Supplementary Fig. 5 and Supplementary Fig. 6 show the Electrochemical Impedance Spectroscopy (EIS) data of all the Single Crystalline (SC) and Hot-Pressed (HP) LLZO samples tested herein, once in form of a Nyquist (a) and once in form of a Bode (b) plot. For the SC samples, only one semicircle in the Nyquist plot is visible, with one corresponding plateau in the Bode plot. Due to the lack of grain boundaries in a single crystal this contribution can be assigned to the bulk. Except for the first ones, HP DC1 and 2, the HP samples show a similar behavior and only reveal one contribution in either plot. HP DC1 was not heat-treated and HP DC2 did not undergo a polishing step directly prior to coating. In both cases, an additional contribution connected to the electrode|electrolyte interface is present in the plots and results in a much higher Area Specific Resistance (ASR, see **Supplementary Tab. 4**) as opposed to the treated samples.

Supplementary Note 2: Applied pressure determination

In our homemade setup a spring holds the vice jaw in place counteracting the force exerted from the screw. The spring constant of this spring (2,5 ± 0,5 N/m) was determined by measuring the compression at two different force levels (15 and 30 N) at 25°C. The force exerted by turning the screw one turn was determined to be $(3.3 \pm 0.5) \times 10^{-4}$ N. Since the sample was fixed by turning the screw for one turn after the jaws contact it, the pressure can be calculated from the sample geometry (1.84×10^{-6} m^2). This leads to a possible pressure on the sample of (1.8 ± 0.8) kPa.

Supplementary Note 3: Preliminary cycling experiments and identification of favorable protocol

Overall, a typical pulsing sequence in this study is composed of an A:B period, with A representing the current application duration in relation to the pausing time B. In case of a 1:1 sequence, this would mean, that the pausing time matches the current application time, whereas in a 1:2 sequence the pausing time is double the current application time. In the ms-range, A was set to 2 ms (due to instrumental limitations) whereas in the µs-regime, all experiments were conducted with a 1 µs current application time. Overall, first pulsing tests with the PC-samples in the ms-regime revealed no improvement of the electrochemical operation in contrast to direct current application. Reducing the time scale to the µs-range, however, lead to overall significantly higher CCD values (see Supplementary Tab. 2). As evident from the reached CCD values, a low ASR value does not necessarily guarantee high electrochemical performance. This becomes especially evident for sample PC PP 7 and 8 which were both equally treated with a 1:2 pulsing sequence and showed similar ASR values of the pristine pellets (8.8 Ωcm^2 vs. 8.7 Ωcm^2). Whereas PC PP 7 reached an effective CCD of 667 µA/cm^2, PC PP 8 already shorted at 267 µA/cm^2. While the ASR value is highly useful in predicting the quality of the SSE wetting, it does not necessarily reflect the occurrence of surface scratches, which, at high current densities, can become the nucleation sites for Li filaments. Overall, the cycling experiments showed that shorter pausing times appear to be most favorable, which is why all further PP experiments with the SC and HP samples were conducted with a 1:1 µs sequence.

Supplementary Note 4: Failure identification

Examples of a typical symmetric Li||Li cell with SC and HP electrolytes sample are shown in Supplementary Fig. 9 and Supplementary Fig. 10, respectively. Due to simultaneous optical tracking during electrochemical operation, failure identification was simplified, and it could be observed that any significant potential drop was related to Li filament formation. The whole cycling profile in general is composed of the overall cycling curve along with a close-up window showing the voltage drop associated with failure and the corresponding optical evaluation ranging from the intact sample and initiation of the Li filament down to the propagation route and final short circuit. In both cases, the voltage profile shows a significant drop in potential once Li starts to deposit at the right interface and decreases as the dendrite makes its way through the SSE. Once it reaches the opposing side the potential drops to zero. In some cases, filaments would not grow through the entire SSE or cause the voltage to fall to zero.

Supplementary Note 5: CCD studies of SC and HP samples

Supplementary Tab. 3 and Supplementary Tab. 4 contain a list of the SC and HP samples along with their cycling program, interfacial resistances prior to cycling as well as the CCD and effective CCD_{eff} values. The CCD value was chosen to be the current density value where a characteristic potential drop was starting. Additionally, the step size of the program is listed to allow for an uncertainty approximation of the achieved electrochemical performances. The CCD value was therefore specified in the main text as “maximum value – current step size of cycling program”, as the actual CCD lies within this current density range. In case of the SC samples, the first direct current study (SC DC 1-3) was carried out with samples of lower quality, which were cut with a diamond saw and simply sanded and polished with SiC paper like the PC samples. In comparison to the shaped and polished specimens a much higher interfacial resistance could be determined, and the CCD values were lower. In case of the HP samples, the impact of a missing heat treatment and final polishing step is demonstrated in the case of sample HP DC 1. Compared to the SC samples however, the difference does not appear to be as prominent.

Supplementary Note 6: Proof of concept

To check on the effectiveness of pulsed currents in the µs-regime, efficiency and plating experiments were conducted with the PC samples. In case of the plating experiments an asymmetric cell employing a Li and Au electrode was employed and Li metal was plated for a total time of 4 hours with a 1:1 (µs) pulsing sequence. The deposition process was then qualitatively examined in-situ via Optical Microscopy by focusing through the grid of the Au electrode current collector. Supplementary Fig. 7 shows the complete cycling profile along with a close-up of the voltage sequence and an image of the pristine PC surface (1), as well as one picture after finishing the plating (2) and subsequent stripping step (3). Image 2 clearly shows that pulse plating in the µs-range is able to transfer Li across the SSE to the opposing electrode. It should be noted that the surface morphology in this case does not transfer to the situation in the typical symmetric cells used for the regular cycling experiments.

The efficiency of this plating process was then checked by depositing Li metal via 1:1 µs pulsed currents for 4 hours and subsequently stripping it again with direct current application for half the time, being 2 hours in this case. The assumption is that if pulsed currents were less effective than direct current at Li transfer, then the time to remove the same amount of Li would deviate significantly. Despite minor voltage plateaus, no sharp voltage increase was detected during this 2 hour time frame, which is why it can be assumed that the efficiency of pulsed currents at this time scale is close to 100 %.

Supplementary Note 7: Reversibility of lithium filaments

Throughout the whole cycling study of the SC samples, one phenomenon that was encountered several times was the reversibility of lithium filaments after the cell was shorted. As shown in Supplementary Fig. 12 shortly after the beginning of the second half-cycle, the SSE is completely penetrated by Li filaments and the voltage drops to around 0 V. In the subsequent half-cycle, however, this process is reversed as the filaments form back and the sample appears to be optically and electrochemically intact again. Typically, the samples would then short-circuit in the subsequent half-cycle once again and remain in this state for good. Supplementary Fig. 13 shows the evolution of the Electrochemical Impedance Spectroscopy response during such a short-circuiting event where measurements were taken in between half-cycles. Prior to Li filament formation a constant impedance response was obtained (grey markers) up to the last measurement prior to failure (green markers). Once the Li filaments connect both electrodes, a typical short-circuit behavior is recorded (light red) until in the subsequent half-cycle the filaments reverse, and an impedance response is measured again (dark red).

Supplementary Note 8: Modeling stress buildup under pulsed conditions

In assessing whether pulse plating could mitigate stress buildup in lithium filaments, the authors used COMSOL Multiphysics finite element analysis to model the deformation of an expanding metal filament (as discussed in the Methods). Because fracture represents the release of stored elastic energy, the value of the elastic energy stored under a given set of boundary conditions should track with the propensity for fracture. Furthermore, due to force balance at the metal electrolyte interface, the elastic energy stored within the electrolyte should track with the elastic energy stored in the metal filament. Thus, the stored elastic energy in a metal filament can serve as a proxy for the propensity of the electrolyte surrounding the filament to fracture.

Pulse plating was simulated under four conditions: (1) application of 1 mA/cm^2 direct current for 0.5 seconds followed by 0.5 seconds pause (no current application), (2) 0.5 mA/cm^2 direct current for 1 second followed by 1 second pause, (3) 0.25 mA/cm^2 direct current for 2 seconds followed by 2 seconds pause, and (4) 0.5 mA /cm^2 "effectively" pulsed direct current (repeated segments of 1 µs of 1 mA/cm^2 current followed by 1 µs of no current) over a total time of 1 second. Supplementary Fig. 15 displays the resulting elastic energy stored in the filament versus normalized time (that is, time / 2 for conditions (2) and (4), and time / 4 for condition (3)).

Because the time displayed on the x-axis is normalized by the total plating time for simulations of equal plated capacities, the x-axis represents a measure of plated capacity during the simulation. At a given value on the x-axis, all four plating simulations possess an identical volume of metal "plated." As seen in this figure, the elastic energy stored in the filament during plating increases with increased direct current density during the plating segment. However, the 0.5 mA/cm^2 "effective" current density from the pulse plating simulation possesses a similar elastic energy stored to the 0.5 mA/cm^2 conducted under direct current plating. Thus, mechanical relaxation of stresses within the filament that may occur during the "off" segment of pulse plating does not appear to substantially mitigate the electrolyte fracture as compared to the direct current plating case.

Supplementary Note 9: The role of the defect shape

Consider a LLZTO surface that is composed of different sized defects, such as grain boundaries, flaws or pores in contact with Li metal. Once such a defect is filled up with Li and a high enough current is applied such that the Li-ion flux towards the tip exceeds the Li-ion flux from the tip, a significant stress builds up and eventually fractures the ceramics. Our previous study found filaments to become critical after they exceed an aspect ratio of ≈ 3:1.[21] For a simple analysis the stress distribution is assumed constant so that textbook fracture mechanics apply. When the applied stress intensity factor K_I is larger than the critical stress intensity factor K_{Ic} (i.e., the fracture toughness), a crack nucleates and propagates. K_{Ic} can be calculated by considering the applied stress σ, a geometry factor Y (which is reasonably close to 1) and the crack length c using Eq. 5.

$$K_{Ic} = \sigma Y * \sqrt{c} \tag{5}$$

Supplementary Fig. 16 shows the dependence of the generated stress intensity factor on the crack length at an assumed homogeneous internal stress of 500 MPa, based on Eq 5, (note: arbitrary number since this value is not known for LLZO so far) is shown. The K_{Ic} of a grain and grain boundary can be assumed as 0.7 MPa $m^{0.5}$ and 0.3 MPa $m^{0.5}$, respectively.[22] In this simplified model, the grain boundary and bulk defect must be larger than about 300 nm and 2 µm, respectively, to generate a stress intensity factor sufficiently high to advance a crack on a pre-existing flaw. In consequence, there is a certain minimum flaw size for each current density, under which no filament generation occurs. However, before a flaw can become critical, it must be filled with Li which will require a certain amount of time depending on the applied current density, as plotted in Fig 6**d**. Therefore, smaller flaws can be filled and, hence, become critical faster than larger ones. After becoming critical the propagation speed of the flaw is much higher than the filling speed making it the main failure cause. While the possible minimum flaw size in a single crystal is only determined by the surface preparation, grains and grain boundaries mark the smallest possible non removable flaws in a polycrystal. Hence it seems logical for the HP sample to fail earlier.

Supplementary Note 10: Active surface area comparison

Two HP samples were prepared and coated with Li. One was cycled until failure with direct current application, failing at 200 µA/cm², whereas the other one was cycled with pulsed currents and stopped at 200 µA/cm² without failure. The interfaces of both samples, where lithium was plated, were then investigated via Focused Ion Beam-Scanning Electron Microscopy, as shown in Supplementary Fig. 19. For both samples an intimate contact between the LLZTO and the Li electrode is seen. There is also no discernible difference in the apparent contact area, as a few occluded voids are close to the interface region in both cases. The evolution of the impedance for both samples is shown in Supplementary Fig. 20.

REFERENCES

1. Cai, M. et al. Robust Conversion-Type Li/Garnet interphases from metal salt solutions. *Chem. Eng. J.* **417** (2021): 129158.
2. Lu, G. et al. Universal lithiophilic interfacial layers towards dendrite-free lithium anodes for solid-state lithium-metal batteries. *Sci. Bull.* **66.17** (2021): 1746-1753.
3. Chen, Y. et al. Nanocomposite intermediate layers formed by conversion reaction of SnO_2 for Li/garnet/Li cycle stability *J. Power Sources* **420** (2019): 15-21.
4. Huang, X. et al. None-mother-powder method to prepare dense Li-garnet solid electrolytes with high critical current density. *ACS Appl. Energy Mater.* **1.10** (2018): 5355-5365.
5. Zhou, D. et al. Garnet electrolytes with ultralow interfacial resistance by SnS2 coating for dendrite-free all-solid-state batteries. *ACS Appl. Energy Mater.* **4.3** (2021): 2873-2880.
6. Yang, L., et al. Rapid preparation and performances of garnet electrolyte with sintering aids for solid-state Li–S battery. *Ceram* **47.13** (2021): 18196-18204.
7. He, X. et al. Tuning Interface Lithiophobicity for Lithium Metal Solid-State Batteries. *ACS Energy Letters* **7.1** (2021): 131-139.
8. Wei, Y. et al. An oxygen vacancy-rich ZnO layer on garnet electrolyte enables dendrite-free solid state lithium metal batteries. *Chem. Eng. J.***433** (2022): 133665.
9. Liao, Y.-K., et al. Extensively Reducing Interfacial Resistance by the Ultrathin Pt Layer between the Garnet-Type Solid-State Electrolyte and Li–Metal Anode. *ACS Appl. Mater. Interfaces* **13.47** (2021): 56181-56190.
10. Zheng, C. et al. Grain boundary modification in garnet electrolyte to suppress lithium dendrite growth. *Chem. Eng. J.* **411** (2021): 128508.
11. Liu, B. et al. A simple strategy that may effectively tackle the anode-electrolyte interface issues in solid-state lithium metal batteries. *Chem. Eng. J.* **427** (2022): 131001.
12. Huang, Z. et al. Enhanced performance of $Li_{6.4}La_3Zr_{1.4}Ta_{0.6}O_{12}$ solid electrolyte by the regulation of grain and grain boundary phases. *ACS Appl. Mater. Interfaces* **12.50** (2020): 56118-56125.
13. Ruan, Y. et al. A 3D cross-linking lithiophilic and electronically insulating interfacial engineering for garnet-type solid-state lithium batteries. *Adv. Funct. Mater.* **31.5** (2021): 2007815.
14. Guo, H. et al. Achieving high critical current density in Ta-doped $Li_7La_3Zr_2O_{12}$/MgO composite electrolytes. *J. Alloys Compd.* **856** (2021): 157222.
15. Wan, Z. et al. Three-dimensional alloy interface between $Li_{6.4}La_3Zr_{1.4}Ta_{0.6}O_{12}$ and Li metal to achieve excellent cycling stability of all-solid-state battery. *J. Power Sources* **505** (2021): 230062.
16. Fu, J. et al. In situ formation of a bifunctional interlayer enabled by a conversion reaction to initiatively prevent lithium dendrites in a garnet solid electrolyte. *Energy Environ. Sci.* **12.4** (2019): 1404-1412.
17. He, X, et al. Cu-Doped Alloy Layer Guiding Uniform Li Deposition on a Li–LLZO Interface under High Current Density. *ACS Appl. Mater. Interfaces* **13.35** (2021): 42212-42219.
18. Taylor, N. J. et al. Demonstration of high current densities and extended cycling in the garnet $Li_7La_3Zr_2O_{12}$ solid electrolyte. *J. Power Sources* **396** (2018): 314-318.
19. Zhong, Y. et al. A Highly Efficient All-Solid-State Lithium/Electrolyte Interface Induced by an Energetic Reaction. *Angew. Chem. Int. Ed* **59.33** (2020): 14003-14008.
20. Hitz, G. T. et al. High-rate lithium cycling in a scalable trilayer Li-garnet-electrolyte architecture. *Mater. Today* **22** (2019): 50-57.
21. Porz, L. et al. Mechanism of lithium metal penetration through inorganic solid electrolytes. *Adv. Energy Mater.* **7.20** (2017): 1701003.
22. Porz, L. et al. Characterizing brittle fracture by modeling crack deflection angles from the microstructure. *J. Am. Ceram. Soc.* **98.12** (2015): 3690-3698.

Paper II

Deflecting dendrites by introducing compressive stress in Li7La3Zr2O12 using ion implantation

F. Flatscher, J. Todt, M. Burghammer, H.S. Soreide, L. Porz, Y. Li, S. Wenner, V. Bobal, S. Ganschow, B. Sartory, R. Brunner, C. Hatzoglou, J. Keckes, D. Rettenwander *submitted Manuscript*

Deflecting dendrites by introducing compressive stress in Li7La3Zr2O12 using ion implantation

Florian Flatscher[a,b], **Juraj Todt**[c], **Manfred Burghammer**[d], **Hanne-Sofie Soreide**[a], **Lukas Porz**[a], **Yanjun Li**[a], **Sigurd Wenner**[e], **Viktor Bobal**[f], **Steffen Ganschow**[g], **Bernhard Sartory**[h], **Roland Brunner**[h], **Constantinos Hatzoglou**[a], **Jozef Keckes**[c], **and Daniel Rettenwander**[a,b,*]

[a]Department of Materials Science and Engineering, NTNU Norwegian University of Science and Technology, Trondheim, Norway
[b]Christian Doppler Laboratory for Solid-State Batteries, NTNU Norwegian University of Science and Technology, Trondheim, Norway
[c]Chair of Materials Physics, Montanuniversität Leoben and Erich Schmid Institute for Materials Science, Austrian Academy of Sciences, Leoben 8700, Austria
[d]European Synchrotron Radiation Facility, 6 rue Jules Horowitz, BP220, 38043 Grenoble, cedex 9, France
[e]SINTEF Industry, Department of Materials and Nanotechnology, Trondheim Norway
[f]University of Oslo, Oslo Norway
[g]Leibniz-Institut für Kristallzüchtung, Berlin, Germany
[h]Materials Center Leoben, Leoben 8700, Austria
[*]daniel.rettenwander@ntnu.no

ABSTRACT

Lithium dendrites belong to the key challenges of solid-state battery research. They are unavoidable due to the imperfect nature of surfaces containing defects of a critical size that can be filled by lithium until fracturing the solid electrolyte. The penetration of Li metal occurs along the propagating crack until a short circuit takes place. We hypothesise that ion implantation can be used to introduce stress states into $\mathrm{Li_{6.4}La_3Zr_{1.4}Ta_{0.6}O_{12}}$ which enable an effective deflection and arrest of dendrites. The compositional and microstructural changes are studied via atom probe tomography, FIB-SEM with correlative TOF-SIMS, STEM and nano XRD indicating that Ag-ions can be implanted up to 1 μm deep and amorphization takes place down to 650-700 nm, in good agreement with kinetic Monte Carlo simulations. Based on nano XRD results pronounced stress states up to -700 MPa are generated in the near-surface region. Such a stress zone and the associated microstructural alterations exhibit the ability to not only deflect mechanically introduced cracks but also dendrites, as demonstrated by nano-indentation and galvanostatic cycling experiments with subsequent FIB-SEM observations. These results demonstrate ion implantation as a viable technique to design “dendrite-free” solid-state electrolytes for high-power and energy-dense solid-state batteries.

Introduction

Lithium metal has been the holy grail of anode materials for Li batteries, since the first usage in the 1960s, boasting the highest theoretical capacity at 3860 mAh g^{-1}, the lowest possible electrochemical potential, -3.04 V vs. standard hydrogen electrode, and a low mass density.[1–4] Despite its desirable parameters, safety issues stemming from dendritic growth of lithium, short circuiting and subsequent ignition of the liquid electrolyte, have led to its replacement by the graphite anode in commercial lithium ion batteries.[1–4] Through the usage of non-flammable solid electrolytes which are compatible with lithium metal, such as the oxide garnet $Li_7La_3Zr_2O_{12}$ (LLZO), safety concerns can be remedied and a resurgence of the lithium metal anode is possible.[5,6]
The problem of dendritic growth remains though, still present in solid electrolytes, which are prone to being cracked by lithium dendrites, even when the material is mechanically stronger than lithium metal. This can happen at current densities as low as 0.1 mA/cm^2 at room temperature.[7–9] The precise mechanism of dendrite formation in solid electrolytes is far from fully explored but one explanation is that inhomogeneous current distribution, sometimes named current focusing, leads to preferential lithium plating, accelerating the build-up of mechanical stress in the ceramic until it is released in fracture of the material.[10–13]

Recently it was found that directed stresses in the material allow for guiding the growing crack in a certain direction. With increasing in plane compressive stress, the path of the growing crack aligns more and more with the stress direction, depending on the initial crack angle, as the path of least resistance from the mechanical perspective diverges from the electrochemical one. It was shown that if the stress is high enough, at least in the 200 MPa range for LLZO, cracks can be diverted to a 90 ° angle from the surface regardless of the initial crack direction. This can stop the dendrite from reaching the opposite electrode and short circuiting the cell.[14] In the work described, the stress was applied through mechanical bending of the solid electrolyte via a cantilever. Since bending a whole battery pack is rather impractical, the introduction of residual stress is necessary.
There are a few methods to introduce residual stresses, which is also known to increase the fracture resistance, depending on the type of stress introduced into a material. In metallurgy residual stresses are introduced during plastic deformation of the material, which is known as work hardening, if it occurs heterogeneously throughout the material. Work hardening can be used to significantly increase the hardness of the substrate by increasing the defect density in the material.[15] It can in principle be applied to any crystalline material, though it depends on the ductility. While metals can be deformed to introduce stresses, the same approach would shatter brittle ceramics, which LLZO counts as. This disallows the use of large scale plastic deformation like cold rolling and special care has to be taken when introducing residual stresses using methods, such as shot peening, Laser shock peening or sand blasting in order to keep the material intact.[16–20] Other possible methods include strengthening via grain boundaries, transformation hardening, second phase hardening and solid solution strengthening.[21] To achieve a solid solution in a ceramic, a proven method from the semiconductor industry can be used to introduce foreign ions into the matrix, ion implantation.[22–24]Previous research on different ceramics, such as MgO, Al2O3, and SiC has shown that an ion-implanted material can exhibit a higher fracture toughness.[24,25]

The implantation of ions has a multitude of effects on the material properties, depending on the used parameters. With a high enough dose of the implanted ions or beam power, the collisions of the ions with the lattice can destabilize it, leaving behind an amorphous layer in its wake.[23,24] Both of those parameters also determine the penetration depth than can be reached. This amorphized layer can even be mechanically weaker than the starting material.[24] The conductive properties of the material can also be influenced due to the implantation. Implanted ions can create additional states in the band structure changing the electronic conductivity, which made semiconductor applications possible and is the main reason for its use.[26] If the material is amorphized, pathways for ionic conduction can be diminished,

which for battery applications is rather detrimental. Nevertheless, amorphous LLZO in thin film batteries has already been reported to reach reasonably high current densities (3.2 mA cm^{-2}) without dendrite growth. There the thinness of the layer (70 nm) overcomes the diminished ionic conductivity of 4 orders of magnitude compared to bulk crystalline LLZO.[27] In the semiconductor industry annealing processes are typically used to regain the crystallinity and to benefit only from the increased electronic conduction without having to worry about an inhomogeneous distribution in the amorphous structure.[22] Parameters to achieve a similar reconstruction of the lattice, known as recrystallization, while keeping ion migration low, are not known yet in literature for solid electrolytes in general and LLZO specifically. Contrary to the semiconductor industry, with thin finely polished single crystalline wafers, processing of polycrystalline material would be preferred for battery purposes to keep costs low and production volume high. This means grain boundaries and natural defects need to be kept in mind. A shallow implantation depth can run into orientation effects, leading to an inhomogeneous implantation profile similar to the implantation into nonplanar semiconductors.[28] A defect which extends past the implanted zone can also be filled with lithium and bypass the deflective properties from the stress field generated by the implanted ions.
In a recent publication[29] it was shown that ion implantation is possible for solid electrolytes and given a tentative stress value of -3-20 GPa in LLZO, depending on the dosage of implanted Xenon ions, retrieved from the examination of grazing incidence XRD data and molecular dynamics simulations. It has to be noted that the implantation depth in Yao et al is rather shallow, calculated at up to 60 nm and is below the common defect size in the sub µm size, as also mentioned by Yao et al. Furthermore, in situ plating of lithium in a TEM measurement showed fracture of “defect free” single crystalline LLZO from the local stresses generated by lithium ions, reaching up to GPa levels.[30]

This study reveals that stress states in the near surface region up to 1 μm depth and up to -700 MPa can be introduced into $Li_{6.4}La_3Zr_{1.4}Ta_{0.6}O_{12}$ (LLZTO) by ion implantation. Such a high stress is introduced by an Ag-ion concentration lower than 0.003 at% in the LLZTO matrix and accompanied by the amorphization of the top 650-700 nm of LLZTO. Since the stressed zone is significantly deeper than the typical defect size mechanically introduced cracks have been shown to be deflected perpendicular to the indentation direction. Finally, we demonstrated that the same is true for dendrites with respect to the penetration direction, which opens a new avenue to designing “dendrite-free” solid-state electrolytes for high power and energy dense solid-state batteries.

Results and discussion

SRIM simulation and structural profile

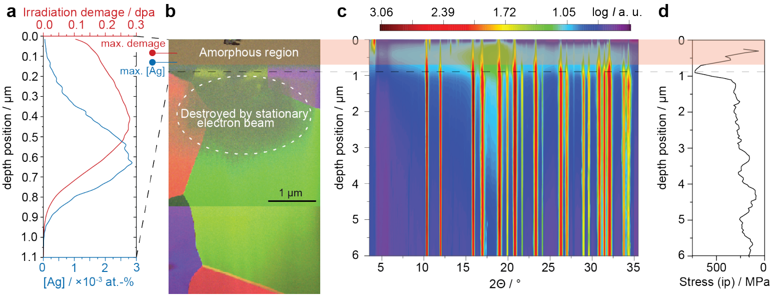

Figure 1. SRIM simulation of the damage and Ag ion distribution in $Li_{6.4}La_3Zr_{1.4}Ta_{0.6}O_{12}$ crystal irradiated with 1.93 MeV Ag ions. b) SPED composite dark field image of a hot pressed $Li_{6.4}La_3Zr_{1.4}Ta_{0.6}O_{12}$ polycrystal with Ag implanted into the top layer. An amorphous layer 650 nm deep is clearly visible. The material has also been shown to be particularly electron beam sensitive, being easily amorphized by the stationary electron beam between measurements. c) Compilation of cross-sectional nano X-ray diffraction patterns of the implanted polycrystalline LLZTO sample. The implanted region is shaded in orange. An amorphous region can be seen, starting from the surface down to a depth of 700 nm. Compressive in plane stress is shown in d) reaching a peak value of -700 MPa at 850 nm.

To identify the implantation conditions that allow the introduction of residual stresses in a depth up to 1 µm in LLZTO we calculated the Ag implantation and damage profiles by kinetic Monte Carlo simulations with SRIM software (Figure 1a). It is shown that for implantation within 1 μm a beam energy of 1.93 MeV has to be used. Both, the distribution of incorporated Ag ions as well as the associated damage caused by the irradiation can be estimated with a peak at 630 ± 30 nm and at 430 ± 25 nm for the amount of incorporated Ag ions and damage, respectively. With a dose of $1x10^{14}$ Ag-ions cm^{-2} an implanted concentration of 0.003 at% can be expected at the peak. There is the question of how accurate the simulation is when dealing with a polycrystalline ceramic, with possible chemical inhomogeneities. When predicting the ranges for single-crystalline silicon, it is rather precise with a slight overestimation of the range by 2-6 nm increasing with implantation energy.[31] For polycrystalline samples, in general and for LLZTO specifically such studies are, to the best of our knowledge, not available.

In order to visualize potential changes in crystallinity Virtual Dark Field imaging was applied to a Scanning Precession Electron Diffraction (SPED) measurement of an implanted polycrystalline LLZTO sample as shown in Figure 1b. It reveals grain size in the range of 3-6 μm and amorphization of LLZTO down to a depth of around 650±10 nm. The region below shows indications of a mixed crystallinity, with amorphous regions dotting crystalline parts, though it is difficult to distinguish between amorphization caused by electron beam damage and the one stemming from ion implantation. This is in accordance with the Monte Carlo simulation and allows the assumption that a significant amount of the incorporated Ag could be detectable in a range from 550 to 750 nm for further measurements. Since structural degradation of LLZTO takes place even when using low beam current during SPED (see Supplementary Figure. 1), atomic resolution imaging and locating the implanted Ag as well as the chemical analysis via EDS or EELS has been hindered (attempted EDS and EELS results are shown in Supplementary Figure 2a-e).

Therefore, atom probe tomography (APT) analyses were performed at the peak implantation depth, around 700 nm, as well as after the peak damage, depth of 1300 nm. The noise level of the mass spectra under the chosen analysis conditions does, however, not allow to detect the low Ag content (around 0.003 at% at the peak of implantation based on SRIM simulation). In Figure 2a the 3D reconstruction of one of the three datasets obtained from a depth of 700 nm is shown which is representative for all of them. The atoms are homogeneously distributed throughout the needle and no grain boundaries are visible, meaning only a single grain was investigated. The chemical composition, shown in Supplementary Table 1 is close to the nominal composition of $Li_{6.4}La_3Zr_{1.4}Ta_{0.6}O_{12}$. Although, LLZTO is intended to be single phase (see XRD, SEM, and TEM analysis) the 3D reconstruction from a depth of 1300 nm on the other hand shows a clearly visible grain boundary, a grain with the same composition as in the previous dataset and a lithium deficient grain on top of it (Figure 2b). The lithium content in the upper grain is around 10.4 ± 2.0 at.%, see Supplementary Table 1, while still having a homogeneous distribution of atoms. A proxigram from the grain boundary, Supplementary Figure 3 shows the transition in lithium content. There is also a dataset only containing a lower lithium content. The Li-poor extra phase could be related to minor extra phases which have already been present in the sample or to a lithium loss in the high vacuum conditions during the APT analysis, which has been recently demonstrated.[32,33]

Finally, we used FIB-SEM with correlative TOF-SIMS to find evidence for the presence of Ag ions in the implanted zone. Figure 2c depicts the spots where the TOF SIMS measurements were taken and a slight peak, at 106.8 mass to charge ratio is visible in the first 0.9 μm diameter spot, which can be attributed to the ^{107}Ag implanted into this region. This peak vanishes in the other two spots in Figure 2d confirming that the Ag is implanted into the desired depth. Attempts to, at least qualitatively, confirm the implantation profile using larger spots, shown in Supplementary Figure 4 dropped the signal below the threshold where it is distinguishable from noise.

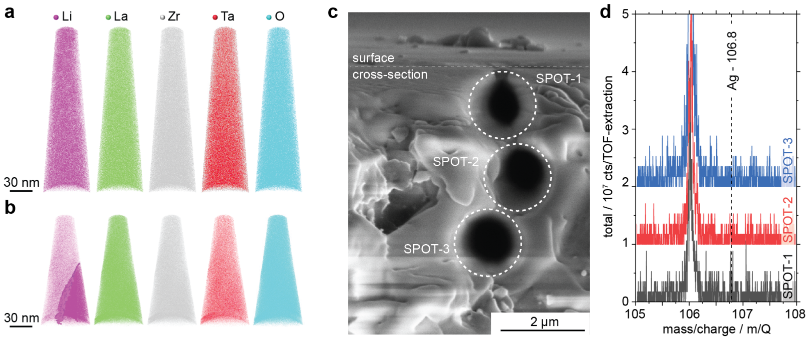

Figure 2. Atom probe tomography reconstruction of a needle prepared from a depth of 700 nm. The atoms are distributed homogeneously throughout the needle b) Reconstruction of a needle from a depth of 1300 nm. While there is still a homogeneous atom distribution within grains the lithium content in the upper part is lower. c) SEM image of the cross section of the implanted LLZTO sample. The 900 nm diameter spots are where TOF SIMS measurements were taken. d) TOF sims data from the three spots in b. There is a barely visible peak for ^{107}Ag at 106.8 mass to charge ratio for the first spot. This peak vanishes for the other spots which are below the implanted region.

Stress profile

To determine the localized strain of the LLZTO after implantation, scanning precession electron diffraction has been performed (Supplementary Figure 5). The diffraction patterns and the simulated patterns of LLZTO are generally in good agreement (see Supplementary Figure 5b-c), though some parts of the sample are only partially crystalline resulting in slightly divergent diffraction spots. Hence, the resolution of the electron diffraction spots has not been high enough to get reliable strain values.

Therefore, cross-sectional scanning nano XRD was used on a mechanically thinned sample to quantify the residual stress depth-profile created by the implanted ions. The 80 nm X-ray spot size allows the measurement of residual stresses and crystallinity with a high spatial resolution. The depth-dependent XRD patterns (Figure 1c) confirm a partial amorphization of the top 700 nm as indicated by the broad diffuse scattering peak centered around 18 degrees 2Θ and the inversely proportional decrease of reflections related to the LLZTO phase, as opposed to the underlying region below. From the orientation-dependent peak position a depth-resolved residual stress profile can be calculated. At a depth of 850 nm below the surface, just below the amorphized layer, a compressive stress peak up to approx. -700 MPa was evaluated, whereas throughout the rest of the layer the stress level does not exceed approx. -250 MPa. The slight waviness of the residual stress depth profile is stemming from the fact that the recorded XRD patterns lie somewhere between those corresponding to a single-crystal and fully powder-like poly-crystal, resulting in residual stresses corresponding to the transition range between 1st and 2nd order stress, i.e., including some degree of grain-to-grain stress variation.

Based on this stress value and the methodology established in Fincher et al, it is possible to determine the flaw size of a dendrite that can be deflected with the present stress.[14] Equation 1 is adapted from Fincher et al to determine the flaw size a and assumes a K_{IC}= 1 MPa m$^{1/2}$ for LLZO, same as in the reference, that our determined compressive stress at -700 MPa is 10 % higher than the critical stress σ_{crit} to deflect all growing cracks to 90° giving a σ_{crit} =636 MPa.

$$a = \frac{(K_{IC})^2}{(1.12 * \sigma_{crit})^2 * \pi} = 627nm \tag{1}$$

From this a flaw size of 627 nm is determined, which means that with the present stress of -700 MPa in a depth of 850 nm growing cracks should be deflected.

Proof of concept: deflection of cracks

To test if crack deflection occurs with the implantation of Ag ions, Nanoindentation was used to probe the implanted region on a larger single crystalline LLZTO sample. The resulting crack propagation was observed in a FIB SEM cut (see Figure 3a). Below the indentation imprint a crack runs parallel to the surface at a depth of 850 nm. This is as expected at the depth of the compressive stress zone, determined in the previous section. Notably absent are cracks connecting the indentation imprint and the fracture, which should be present if it is a radial fracture. Above the crack the amorphous region is again visible due to its differing contrast, additionally confirming the previous TEM and XRD results. To prove the hypothesis that the implementation of stressed zones by ion implantation can also deflect dendrites we applied electrical current well above reported critical current densities to a thinned sample with Li metal on both sites until the voltage reached device limitations, as a result of reduced contact area from lithium stripping. The corresponding current-voltage curve is shown in Figure 3b. Figure 3c shows the setup used during this kind of short circuit testing, where the sample is contacted with lithium in two places, carefully applied only on the side, to avoid circumventing the implanted layer and the zone of compressive stress. It is evident from Figure 3d,e that dendrites deflect after the implanted region, similar to mechanically induced cracks. The deflection zone is somewhat past the stress maximum, determined at 850 nm, and the crack begins to kink at around 700 nm and is fully deflected at 1.5 μm. Where the indented sample fractures at the zone of compressive stress, the growing dendrite has to snake its way through an increasing stress field, which can differ locally from the averaged values determined via XRD. Similarly, the bulk K_{IC}

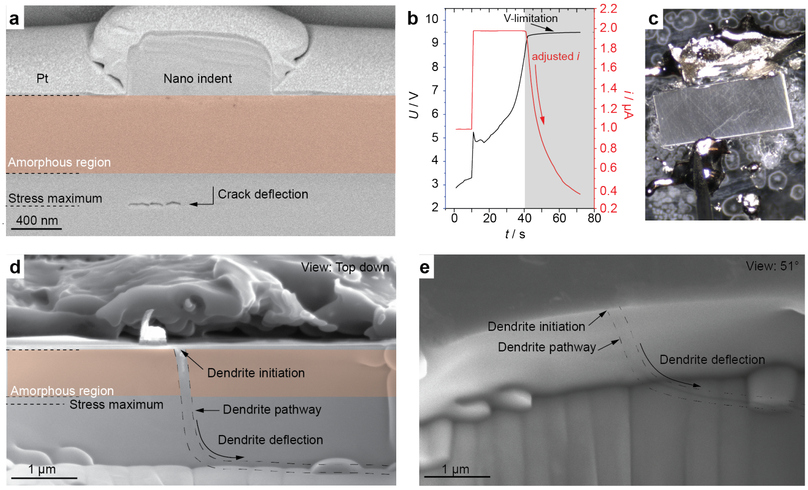

Figure 3. a) SEM image (Backscattered electrons) of a mechanically induced crack by nano indentation in Ag implanted LLZTO. The crack grows preferably parallel to the surface. (b) Voltage profiles during the short circuiting measurement, spliced together. Current was doubled after 10s and held until the voltage limit was reached, likely due to void formation decreasing the contact area. (c) Optical microsope image of the thinned hot pressed LLZTO during the short-circuit measurement. (d,e) SEM image of an electrochemically induced crack in Ag implanted LLZTO. Top view (d) and 51 ° angled view (e). The implanted region is shaded in orange, and the crack highlighted with a dashed line. After the implantation zone the crack diverts parallel to the surface.

value can differ from K_{IC} value at lower length scales. With this it is entirely plausible for the crack to be fully deflected after the stress maximum, which is in agreement with Fincher et al, where it was shown that once the crack starts to kink and constant stress remains, it will eventually be turned by 90°.[14]

Impact on electrical properties

Since the damage caused by the ion beam and the change in the lattice from the differently sized ions implanted can have significant impact on the interfacial transport properties, electrochemical impedance spectroscopy (EIS) has been performed. In Figure 4 a Nyquist plot of a non-implanted LLZTO reference sample and an Ag-implanted sample can be seen. EIS of the Ag implanted LLZTO samples with non-blocking electrodes show the occurrence of a second semicircle as a result of the implantation procedure. This can be attributed to the now amorphized layer on both sides. The pristine hot-pressed sample was fitted with an equivalent circuit consisting of a resistor and a constant phase element (CPE) in parallel. A constant phase element was chosen instead of the capacitance as the semicircle is slightly depressed. The calculated ionic conductivity is $4.9\text{x}10^{-4}$ S cm^{-1}. Under the assumption that the bulk conductivity does not change and that the amorphous layer is symmetric on both sides the implanted sample was fitted with an equivalent circuit of two parallel R-CPE elements in series. The resulting ionic conductivity for the amorphous layer, calculated with the known thickness of 650 nm, is $8.1\text{x}10^{-8}$ S cm^{-1}. This is in good agreement with already reported values for the ionic conductivity of amorphous LLZTO, which are in a similar order of magnitude.[27] The change in lattice structure hindering the lithium-ion transport.

The original crystal structure could be regained by an annealing step, as it is typically used for doped semiconductors. The necessary parameters, how much it will broaden the implantation profile and the impact on the residual stress is not known yet for LLZTO and beyond the scope of this study.

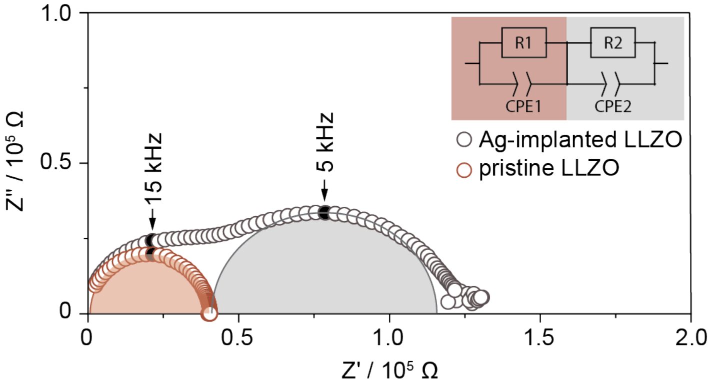

Figure 4. Nyquist plot of an Ag implanted (grey) and a non-implanted (orange) reference hot pressed polycrystal. The equivalent circuits used to fit the arcs are shown in the top right corner. The second semicircle is attributed to the 650 nm amorphous layer which is detrimental to ionic transport as shown in previous literature.[27]

Conclusion

In this study we investigated how Ag ions implanted into LLZTO affect crack growth, specifically induced by growing dendrites. First Ag ions were implanted in LLZTO using conditions determined by kinetic Monte Carlo simulations to introduce ions into a depth of up to 1 µm, with a concentration peak at 750 nm. Determination of the actual concentration distribution and concentration maximum of the implanted ions was then attempted via APT and EELS. We found that the chosen dose of $1x10^{14}$ Ag ions cm^{-2} resulted in an Ag concentration too low to quantify by these methods, so that a qualitative detection had to be achieved via TOF SIMS. Both spatially resolved cross-sectional nano XRD and SPED measurements revealed an amorphization of the region from the surface to a depth of 650 nm deep, partially also due to electron beam damage, which has been shown to be detrimental for the Li-ion conductivity. Moreover, from the corresponding X-ray diffractograms a compressive stress of up to 700 MPa with its peak at a depth of 850 nm has been determined. Thereafter, the impact of the introduced stressed zone on the crack propagation has been evaluated. Cracks were induced in the material, mechanically via nanoindentation, and they indeed formed preferentially at the zone of compressive stress at 850 nm and parallel to the surface. Finally, it has been shown that electrochemically induced cracks (dendrites) can also be deflected, with the crack beginning to kink at around 700 nm depth and fully deflecting slightly after the stress maximum at 1.5 μm.

In summary, our results suggest that introduction of compressively pre-stressed zones in a depth exceeding the critical crack size, in addition with subsequent annealing steps for re-crystallization of amorphous zones, could be a viable strategy to enable “dendrite-free” solid-state electrolytes to improve the rate-performance of solid-state batteries.

Methods

Samples

The $Li_{6.5}La_3Zr_{1.5}Ta_{0.5}O_{12}$ single crystal was pulled from a melt using the Czochralski technique. The thoroughly sintered initial material containing an excess of 20 Mol% Li_2O was melted in an inductively heated iridium crucible in pure Ar atmosphere and the crystal was pulled at a rate of 0.4 mm/h on a rotating seed oriented along [100]. The obtained crystal ingot was 15 mm in diameter and approximately 30 mm long, mainly transparent of slightly yellow color. The upper, first-grown part was covered by a thick film of opaque white material resulting from Li2O depletion caused by evaporation. The hot pressed polycrystals with the composition $Li_{6.4}La_3Zr_{1.4}Ta_{0.6}O_{12}$ were acquired from commercial sources (Toshima). The single and polycrystals were cut into 3x3x0.7 mm cuboids. Two 0.7 mm sides parallel to each other were polished starting with SIC grinding paper with P1200, P2400 and P4000 grit size and final polishing using diamond paste of 3, 1 and 0.25 μm particle size.

Phase purity characterization

For the commercial sample the phase purity was checked via X-ray diffraction. The measurement was carried out on a Bruker Da-Vinci X-ray diffractometer using a Cu Kα source with a scanning window of 10-60 ° and a step size of 0.013 $°\text{min}^{-1}$, see Supplementary Figure 6.

SRIM simulation

The damage in the $Li_{6.4}La_3Zr_{1.4}Ta_{0.6}O_{12}$, irradiated with 1.93 MeV Ag ions, was calculated using the SRIM-2013 software[34,35], in full-cascade mode as recommended in Ref[36]. The density of $Li_{6.4}La_3Zr_{1.4}Ta_{0.6}O_{12}$ was set to 5.46 g cm^{-3}. The threshold energies of displacement were set to 25 eV for Li, La, Zr, Ta and 28 eV for O, according to literature.[37,38]

Ion implantation procedure

The samples were stacked in a stainless-steel sample holder placed into a Pelletron implantation system type 3 SDH-2 NEC. ^{107}Ag ions were implanted into both polished sides, flipping over after implantation of one side, with an energy of 1.930 MeV, a peak concentration of $1x10^{14}$ ^{107}Ag ions cm^{-2} ($1x10^{18}$ ^{107}Ag ions cm^{-3}) and a current density of 85 nA cm^{-2}. The implanted samples were then put in 0.1M HCl for around 20s followed by a rinse with Isopropanol and transferred to an Ar filled glovebox (O_2 and H_2O < 0.1 ppm) for storage and further experiments. Before any experiment, this HCl treatment was repeated to remove any Li_2CO_3 layer formed during storage.

Electrochemical experiments

The implanted sides of the cleaned samples were then coated with a molten LiSn alloy, containing 30 wt% of Sn. The impedance of the coated samples was measured with a Solartron Modulab XM at 25±1 °C with a perturbation voltage of 10 mV from 1 MHz to 10 Hz, 19 datapoints per decade of frequency after a 1 min OCV period. For the creation of dendrites, a current of up to 1 mA cm^{-2} was applied for 1 minute at 25±1 °C. All measurements were performed in an Ar filled glovebox with O_2 and H_2O levels below 0.1 ppm.

TEM/SPED experiments

The $Li_{6.4}La_3Zr_{1.4}Ta_{0.6}O_{12}$ sample was extracted from an Ar glovebox (10 min air exposure) and a 0.5 μm layer of Ti was deposited on the Ag-implanted surface using an AJA electron beam evaporator. This protects against moisture from the air and carbon-containing deposition layers. A lamella was produced and thinned using the standard focused ion beam (FIB) liftout method, with a FEI Helios G4 UX dual-beam instrument. The final thinning was done using 2 kV Ga ions. The lamella was moved to a JEOL 2100F transmission electron microscope (TEM) within 15 min air exposure. Scanning precession electron diffraction (SPED) was conducted using a precession angle of 0.8 degrees and a frequency of 100

Hz. 20 ms diffraction patterns were acquired with a MerlinEM direct electron detector. Virtual dark-field imaging was used to separate grains and crystalline/amorphous areas.

Atom Probe Tomography experiments

The tips for APT analysis were prepared from a lamella that was lifted out from the Ti coated Specimen, flipped upside-down and welded to flat Si posts inside the FIB. In this way, the Ti surface coating acts as a buffer between the specimen and the carbon-containing welding material, and the apex of each tip could be formed at a controlled distance from the original surface. The tips were formed using annular Ga ion milling, finishing with 2 kV for the final sharpening. The APT measurements were carried out on a LEAP 5000 XS from CAMECA equipped with a UV laser. The specimen temperature was set t to 60 K. Laser pulses with an energy of 20 to 30 pJ were used at a frequency of 200 kHz to trigger field evaporation. The standing voltage was automatically adjusted by the software to maintain a detection rate of 0 0.3% ions per pulse. The commercial software IVAS from CAMECA was used for the reconstruction and analysis of the APT data. The reconstructed volumes were built using tip-profile reconstruction using secondary electron images obtained during specimen preparation by FIB.

ESRF experiment

For the Synchrotron measurements two implanted $Li_{6.4}La_3Zr_{1.4}Ta_{0.6}O_{12}$ polycrystalline sample cross-sections were thinned down to a final thickness of around 80 μm by conventional mechanical polishing as mentioned above. The cross-sectional scanning X-ray nanodiffraction (CSnanoXRD) experiment was carried out at the nanofocus end station of the Microfocus beamline ID13 at the European Synchrotron Radiation Facility (ESRF) in Grenoble, France.[39] The sample was scanned by a monochromatic X-ray beam of 13 keV photon energy focused to approx. 80 nm spot size by multi-layer Laue lenses, applying a scanning step of 50 nm in the direction perpendicular to the implanted surface.[40] 40 depth-profile scans spaced 1 μm apart were averaged in order to counteract the poor diffraction statistics that result from the combination of small X-ray beam, thin sample slice and comparatively large grain size of the probed material. Diffraction patterns were acquired in transmission on a Dectris Eiger X 4M two-dimensional (2D) X-ray detector placed 10.98 cm downstream of the sample with an exposure time of 50 ms. The exact detector position was calibrated by measuring a standard corundum reference powder, using the routines provided by the pyFAI software package.[41] 2D diffraction patterns in the form of Debye-Scherrer rings were integrated azimuthally using the pyFAI software package and subsequently processed using custom python scripts for peak fitting with Pseudo-Voigt functions and strain/stress calculation. The evaluation of stress was based on the plausible assumption that there is no force acting perpendicularly on the free surface of the sample,which make the application of a $sin^2\psi$-based method possible. In such a case, the only necessary input parameters are the elastic properties of the probed material, i.e. in this case the X-ray elastic constant $\frac{1}{2}S_2$, which was calculated for the relevant X-ray reflection $\{3\bar{1}2\}$ from literature single-crystal elastic values using in a Hill grain interaction model,as $\frac{1}{2}S^{3\bar{1}2}_{2,LLZO} = 7.83110^{-6}MPa^{-1}$. In summary, the CSnanoXRD experiment and the applied evaluation technique corresponds to earlier studies of thin films samples at the same beamline, for more details see Ref.[42].

Nanoindentation

An implanted single crystalline $Li_{6.4}La_3Zr_{1.4}Ta_{0.6}O_{12}$ sample was placed in a FT-NMT03 nanomechanical testing system utilized within a Cross Beam 340 ZEISS SEM. Indents are controlled by displacement and were made using a Berkovich indenter tip with an indentation depth of 0.1 μm. After attaching a few µm of Pt protection layer a 20x12x10 μm cross section was cut with FIB using a 20 nA beam current, reduced to 4 nA and 600 pA for final polishing on a cross-beam SEM from Zeiss (AURIGA® - CrossBeam workstation). The Image in Fig. 3a was taken with an acceleration voltage of 2kV and performed in backscattered electron mode.

Data Availability

The data that support the findings of this study are available from the corresponding author on reasonable request.

Acknowledgements

D.R. acknowledges financial support by the Austrian Federal Ministry for Digital and Economic Affairs, the National Foundation for Research, Technology and Development and the Christian Doppler Research Association (Christian Doppler Laboratory for Solid State Batteries). We would like to thank Markus Stypa for assistance in crystal growth We acknowledge the European Synchrotron Radiation Facility (ESRF) for provision of synchrotron radiation facilities and we would like to thank Manfred Burghammer for assistance and support in using beamline ID13. The Research Council of Norway (RCN) is acknowledged for the support to the Norwegian Micro- and Nano-Fabrication Facility, NorFab, project number 295864, the Norwegian Laboratory for Mineral and Materials Characterization, MiMaC, project number 269842/F50, and the Norwegian Center for Transmission Electron Microscopy, NORTEM (197405/F50). The authors D.R. R.B and B.S gratefully acknowledge the financial support under the scope of the COMET program within the K2 Center "Integrated Computational Material, Process and Product Engineering (IC-MPPE)" (Project No 886385) within the project ASSESS P1.10. This program is supported by the Austrian Federal Ministries for Climate Action, Environment, Energy, Mobility, Innovation and Technology (BMK) and for Labour and Economy (BMAW), represented by the Austrian Research Promotion Agency (FFG), and the federal states of Styria, Upper Austria and Tyrol.

Author contributions statement

F.F. and L.P performed the experimental work, S.G. synthesized the single crystals. V.B. performed the ion implantation. S.W. performed the FIB cuts, SPED measurements, and APT needle preparation. H.S.S performed the APT analysis under supervision of Y.L. with the help of C.H.. C.H performed the SRIM simulation and APT data treatment and interpretation. B.S. and R.B. performed the nanoindentation. J.T. performed the CS nano XRD measurement with help from M.B., J.K, L.P. and D.R.. D.R. supervised the work. F.F, L.P, and D.R. wrote the first draft of the manuscript. All authors contributed to the final draft.

Competing Interests

The authors declare no competing interests

References

1. Reddy, M. V., Mauger, A., Julien, C. M., Paolella, A. & Zaghib, K. Brief history of early lithium-battery development. *Materials* **13**, 1884 (2020).

2. Xu, W. *et al.* Lithium metal anodes for rechargeable batteries. *Energy & Environ. Sci.* **7**, 513–537 (2014).

3. Tarascon, J.-M. & Armand, M. Issues and challenges facing rechargeable lithium batteries. *nature* **414**, 359–367 (2001).

4. Lin, D., Liu, Y. & Cui, Y. Reviving the lithium metal anode for high-energy batteries. *Nat. nanotechnology* **12**, 194–206 (2017).

5. Yu, S. *et al.* Elastic properties of the solid electrolyte li7la3zr2o12 (llzo). *Chem. Mater.* **28**, 197–206 (2016).

6. Han, F., Zhu, Y., He, X., Mo, Y. & Wang, C. Electrochemical stability of li10gep2s12 and li7la3zr2o12 solid electrolytes. *Adv. Energy Mater.* **6**, 1501590 (2016).

7. Cheng, E. J., Sharafi, A. & Sakamoto, J. Intergranular li metal propagation through polycrystalline li6. 25al0. 25la3zr2o12 ceramic electrolyte. *Electrochimica Acta* **223**, 85–91 (2017).

8. Ren, Y., Shen, Y., Lin, Y. & Nan, C.-W. Direct observation of lithium dendrites inside garnet-type lithium-ion solid electrolyte. *Electrochem. Commun.* **57**, 27–30 (2015).

9. Flatscher, F., Philipp, M., Ganschow, S., Wilkening, H. M. R. & Rettenwander, D. The natural critical current density limit for li7la3zr2o12 garnets. *J. Mater. Chem. A* **8**, 15782–15788 (2020).

10. Tsai, C.-L. *et al.* Li7la3zr2o12 interface modification for li dendrite prevention. *ACS applied materials & interfaces* **8**, 10617–10626 (2016).

11. Porz, L. *et al.* Mechanism of lithium metal penetration through inorganic solid electrolytes. *Adv. Energy Mater.* **7**, 1701003 (2017).

12. Kasemchainan, J. *et al.* Critical stripping current leads to dendrite formation on plating in lithium anode solid electrolyte cells. *Nat. materials* **18**, 1105–1111 (2019).

13. Krauskopf, T., Hartmann, H., Zeier, W. G. & Janek, J. Toward a fundamental understanding of the lithium metal anode in solid-state batteries—an electrochemo-mechanical study on the garnet-type solid electrolyte li6. 25al0. 25la3zr2o12. *ACS applied materials & interfaces* **11**, 14463–14477 (2019).

14. Fincher, C. D. *et al.* Controlling dendrite propagation in solid-state batteries with engineered stress. *Joule* **6**, 2794–2809 (2022).

15. Rollett, A. D. & Kocks, U. A review of the stages of work hardening. *Solid state phenomena* **35**, 1–18 (1993).

16. Kobayashi, M., Matsui, T. & Murakami, Y. Mechanism of creation of compressive residual stress by shot peening. *Int. J. Fatigue* **20**, 351–357 (1998).

17. Gujba, A. K. & Medraj, M. Laser peening process and its impact on materials properties in comparison with shot peening and ultrasonic impact peening. *Materials* **7**, 7925–7974 (2014).

18. Chintapalli, R. K., Rodriguez, A. M., Marro, F. G. & Anglada, M. Effect of sandblasting and residual stress on strength of zirconia for restorative dentistry applications. *J. mechanical behavior biomedical materials* **29**, 126–137 (2014).

19. Altenberger, I. Deep rolling–the past, the present and the future. In *Conf Proc: ICSP*, vol. 9, 144–155 (2005).

20. Shukla, P. P., Swanson, P. T. & Page, C. J. Laser shock peening and mechanical shot peening processes applicable for the surface treatment of technical grade ceramics: a review. *Proc. Inst. Mech. Eng. Part B: J. Eng. Manuf.* **228**, 639–652 (2014).

21. Pelleg, J. *Mechanical properties of ceramics*, vol. 213 (Springer Science & Business, 2014).

22. Williams, J. Ion implantation of semiconductors. *Mater. Sci. Eng. A* **253**, 8–15 (1998).

23. Burnett, P. & Page, T. Criteria for mechanical property modifications of ceramic surfaces by ion implantation. *Radiat. effects* **97**, 283–296 (1986).

24. McHargue, C. J. The mechanical properties of ion implanted ceramics-a review. In *Defect and Diffusion Forum*, vol. 57, 359–380 (Trans Tech Publ, 1988).

25. Gurarie, V., Otsuka, P., Jamieson, D. & Prawer, S. Crack-arresting compression layers produced by ion implantation. *Nucl. Instruments Methods Phys. Res. Sect. B: Beam Interactions with Mater. Atoms* **242**, 421–423 (2006).

26. Pearton, S. Ion implantation in iii–v semiconductor technology. *Int. J. Mod. Phys. B* **7**, 4687–4761 (1993).

27. Sastre, J. *et al.* Blocking lithium dendrite growth in solid-state batteries with an ultrathin amorphous li-la-zr-o solid electrolyte. *Commun. Mater.* **2**, 76 (2021).

28. Tarnavsky, G. A., Vorozhtsov, E. V. *et al.* Dopant implantation into the silicon substrate with non-planar surface. *Energy Power Eng.* **2**, 73–77 (2010).

29. Yao, X. *et al.* Xenon ion implantation induced surface compressive stress for preventing dendrite penetration in solid-state electrolytes. *Small* **18**, 2108124 (2022).

30. Gao, H. *et al.* Visualizing the failure of solid electrolyte under gpa-level interface stress induced by lithium eruption. *Nat. Commun.* **13**, 5050 (2022).

31. Titze, M. *et al.* Evaluation of the accuracy of stopping and range of ions in matter simulations through secondary ion mass spectrometry and rutherford backscattering spectrometry for low energy heavy ion implantation. *J. Vac. Sci. & Technol. A* **39** (2021).

32. Cojocaru-Mirédin, O. *et al.* Quantifying lithium enrichment at grain boundaries in li7la3zr2o12 solid electrolyte by correlative microscopy. *J. Power Sources* **539**, 231417 (2022).

33. Kim, S.-H. *et al.* Atom probe analysis of electrode materials for li-ion batteries: challenges and ways forward. *J. Mater. Chem. A* **10**, 4926–4935 (2022).

34. Ziegler, J. F., Ziegler, M. D. & Biersack, J. P. Srim–the stopping and range of ions in matter (2010). *Nucl. Instruments Methods Phys. Res. Sect. B: Beam Interactions with Mater. Atoms* **268**, 1818–1823 (2010).

35. Ziegler, J. F. & Biersack, J. computer code srim-2003. *The Stopping Range Ions Matter, Version* **2003** (2003).

36. Weber, W. J., Duffy, D. M., Thomé, L. & Zhang, Y. The role of electronic energy loss in ion beam modification of materials. *Curr. Opin. Solid State Mater. Sci.* **19**, 1–11 (2015).

37. Zhang, F. *et al.* Ion irradiation induced strain and structural changes in litao3 perovskite. *J. Physics: Condens. Matter* **33**, 185402 (2021).

38. Pang, L. *et al.* Effect of heavy ions irradiation on litao3 crystal. *Results Phys.* **22**, 103861 (2021).

39. Rettenwander, D. *et al.* Scanning and in-situ mll development for x-ray nanodiffraction on thin film, space and additively manufactured applications. [Data set]. European Synchrotron Radiation Facility. doi.org/10.15151/ESRF-ES-644167190.

40. Kubec, A. *et al.* Point focusing with flat and wedged crossed multilayer laue lenses. *J. Synchrotron Radiat.* **24**, 413–421 (2017).

41. Ashiotis, G. *et al.* The fast azimuthal integration python library: pyfai. *J. applied crystallography* **48**, 510–519 (2015).

42. Keckes, J. *et al.* 30 nm x-ray focusing correlates oscillatory stress, texture and structural defect gradients across multilayered tin-siox thin film. *Acta materialia* **144**, 862–873 (2018).

Supplementary Information

Deflecting dendrites by introducing compressive stress in $Li_7La_3Zr_2O_{12}$ using ion implantation

Florian Flatscher[a,b], Juraj Todt[c], Manfred Burghammer[d], Hanne-Sofie Soreide[a], Lukas Porz[a], Yanjun Li[a], Sigurd Wenner[e], Viktor Bobal[f], Steffen Ganschow[g], Bernhard Sartory[h], Roland Brunner[h], Constantinos Hatzoglou[a], Jozef Keckes[c], Daniel Rettenwander[a,b]

[a] Department of Materials Science and Engineering, NTNU Norwegian University of Science and Technology, Trondheim, Norway
[b] Christian Doppler Laboratory for Solid-State Batteries, NTNU Norwegian University of Science and Technology, Trondheim, Norway
[c] Chair of Materials Physics, Montanuniversität Leoben and Erich Schmid Institute for Materials Science, Austrian Academy of Sciences, Leoben 8700, Austria
[d] European Synchrotron Radiation Facility, 6 rue Jules Horowitz, BP220, 38043 Grenoble, cedex 9, France
[e]SINTEF Industry, Department of Materials and Nanotechnology, Trondheim Norway
[f] University of Oslo, Oslo Norway
[g] Leibniz-Institut für Kristallzüchtung, Berlin, Germany
[h] Materials Center Leoben, Leoben 8700, Austria

Supplementary Figures

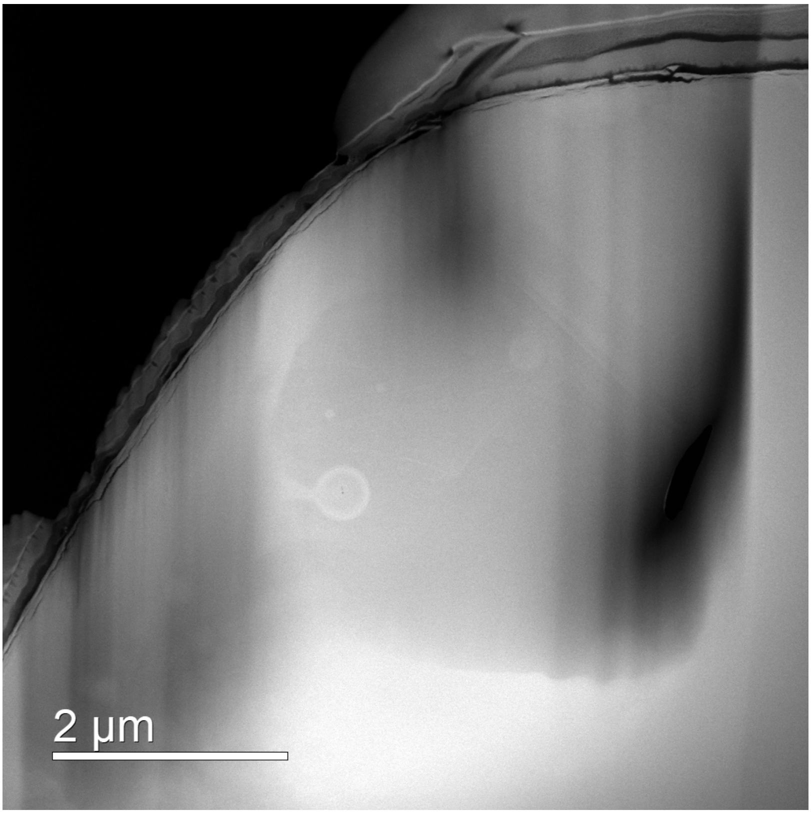

Supplementary Figure 1. Beam damage on an Ag implanted $Li_{6.4}La_3Zr_{1.4}Ta_{0.6}O_{12}$ lamella caused by STEM-EDS measurement visible in the slightly darkened section.

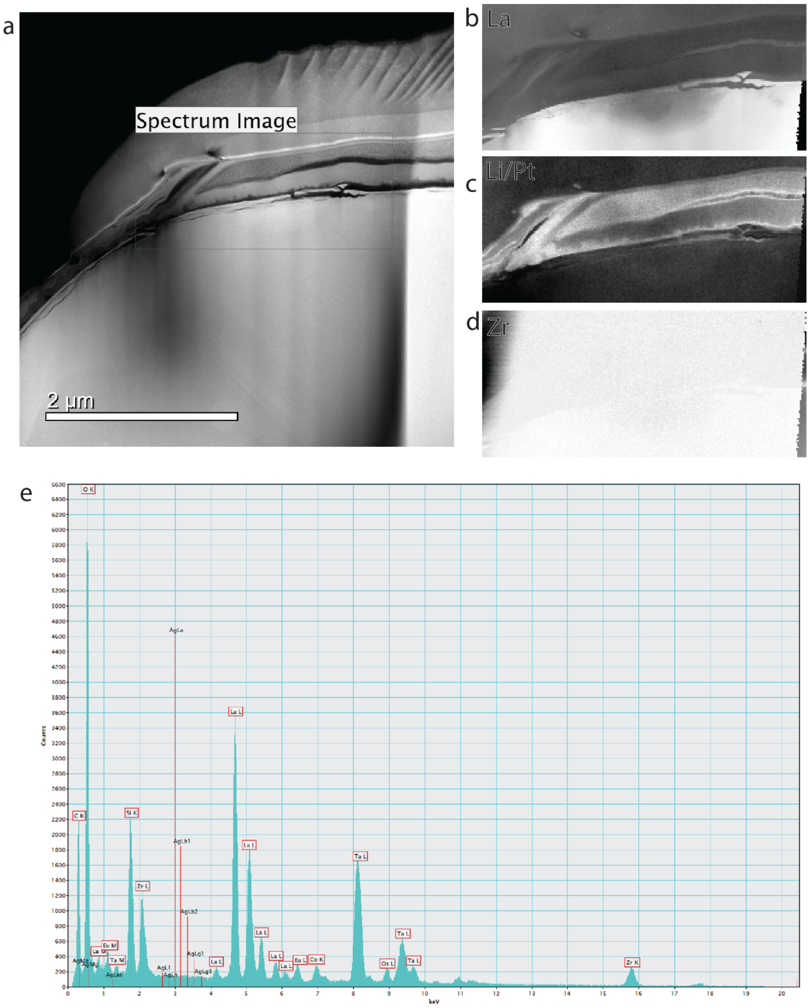

Supplementary Figure 2. EELS map of the Ag-implanted $Li_{6.4}La_3Zr_{1.4}Ta_{0.6}O_{12}$ sample. An overview of the sample and the probed area is shown in a). The bright area in b) is the La. c) shows either Li or Pt. The overly bright area in d) is from the Zr scan where the beam damage made it impossible to get good data. e). EDS data of the sample. La, Zr, O and the dopant Ta could be resolved. The Ag content was too low to be determined.

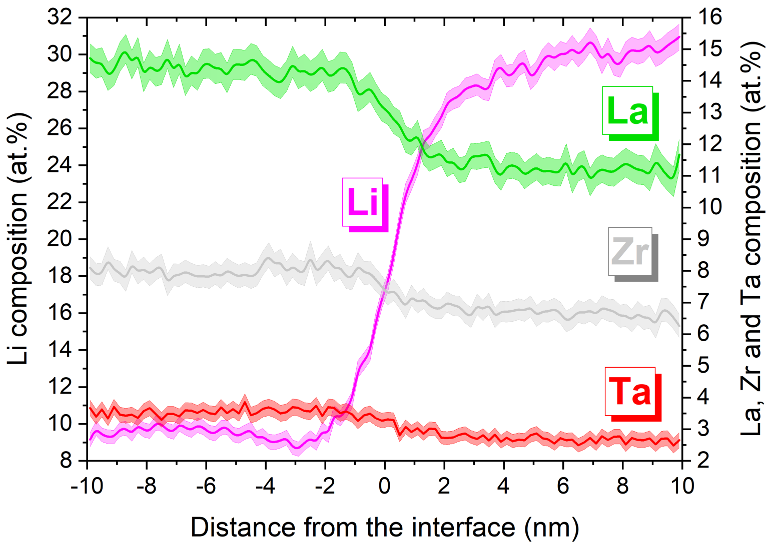

Supplementary Figure 3 Proxigram showing the transition between the low lithium content region to the high lithium content region within the atom probe needle from a depth of 1300 nm of the sample as shown in Figure 2b.

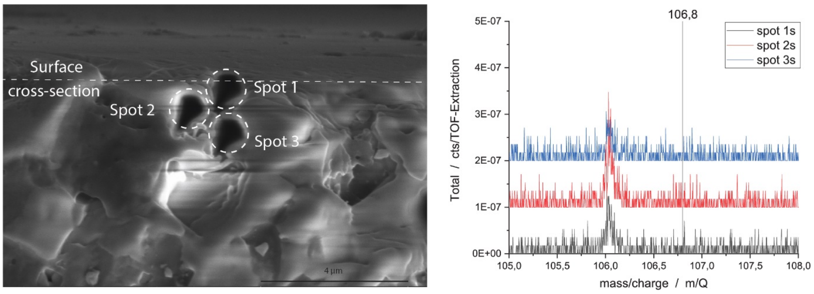

Supplementary Figure 4. Smaller TOF SIMS spots. The number of extracted Ag ions was below the detection limit for the small spots.

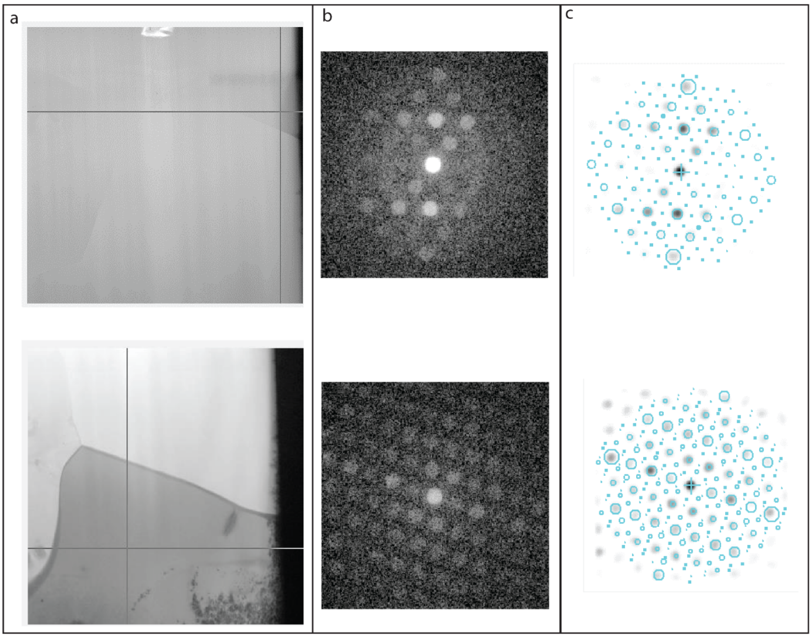

Supplementary figure 5. SPED measurement of the implanted sample. The measurement spots are shown in a). The diffraction patterns from the two spots can be seen in b). The simulated patterns are shown in c) and are in good agreement with the measured data.

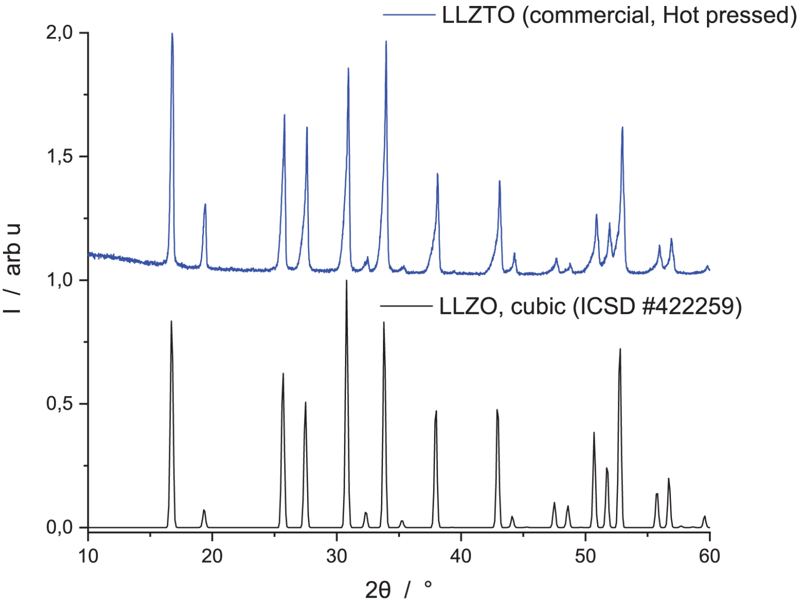

Supplementary figure 6 XRD data of the hot-pressed sample. XRD pattern of the commercial polycrystalline hot-pressed sample with the composition of $Li_{6.4}La_3Zr_{1.4}Ta_{0.6}O_{12}$ from Toshima compared to cubic $Li_7La_3Zr_2O_{12}$ ICSD #422259

Supplementary Tables

Supplementary Table 1. Composition of the APT needles, depth 700 nm (column 2) and depth of 1300 nm (column 2 and 3) from the implanted edge, also shown in Figure 2a-b. The first region is close to the nominal composition of LLZO, shown in the rightmost column with a slightly increased lithium content. The needle from 700 nm depth also shows this composition. The second region shows a significantly lower lithium composition, which could be from a minor extra phase or from lithium loss in the high vacuum of the instrument's measurement chamber.

Element	700 nm needle/ 1300 nm needle Region 1 (at%)	1300 nm needle Region 2 (at%)	$Li_{6.4}La_3Zr_{1.4}Ta_{0.6}O_{12}$ (at%)
Li	31,6±3,6	10,4±2,0	27,4
O	51,3±1,4	64,8±1,9	51,2
Ta	2,2±0,55	2,6±0,1	2,6
La	10,8±0,5	16,6±0,3	12,8
Zr	4,1±0,2	5,6±0,4	6,0

Paper III

Origin of dendrite branching in solid-state batteries

C. Yldirim, F. Flatscher, S. Ganschow, L. Porz, J. Todt, J. Keckes and D. Rettenwander.
Paper manuscript, to be submitted.

Origin of dendrite branching in solid-state batteries

Can Yildirim[1,+], **Florian Flatscher**[2,3,+], **Steffen Ganschow**[4], **Lukas Porz**[2], **Juraj Todt**[5], **Jozef Keckes**[5], **and Daniel Rettenwander**[2,3,*]

[1]European Synchrotron Radiation Facility, 71 Avenue des Martyrs, CS40220, 38043 Grenoble Cedex 9, France.
[2]Department of Material Science and Engineering, NTNU Norwegian University of Science and Technology, Trondheim, Norway
[3]Christian Doppler Laboratory for Solid-State Batteries, NTNU Norwegian University of Science and Technology, Trondheim, Norway.
[4]Leibniz-Institut für Kristallzüchtung, Berlin, Germany
[*]daniel.rettenwander@ntnu.no
[+]these authors contributed equally to this work

ABSTRACT

Lithium dendrite growth within solid electrolytes has been recognized to induce fractures, yet the underlying mechanisms remain elusive. The challenge lies in pinpointing the exact mechanisms within the material's bulk and capturing elusive stress variations at a local scale. Here we employ Dark Field X-ray microscopy to investigate dendrite growth within a single crystalline $\mathrm{Li}6.5\mathrm{La}3\mathrm{Zr}1.5\mathrm{Ta}0.5\mathrm{O}_{12}$ electrolyte, characterizing strain and lattice orientation at high resolution. Our results have revealed, for the first time, the presence of dislocations in close proximity to the dendrite tip, with one dislocation even acting as a pinning point for the tip itself. Given the rarity of dislocations in single crystalline ceramics, this finding prompts the hypothesis that dendrite growth and dislocation generation are interlinked. We propose that the stress induced by dendrite growth initiates the formation of dislocations. These dislocations, in turn, appear to guide the fracture process, providing a plausible explanation for the directional growth and branching patterns observed in dendrites. Our study illuminates dynamics underlying dendrite growth, advancing battery performance understanding.

This paper will be submitted for publication and is therefore not included.

ISBN 978-82-326-7464-0 (printed ver.)
ISBN 978-82-326-7463-3 (electronic ver.)
ISSN 1503-8181 (printed ver.)
ISSN 2703-8084 (online ver.)

NTNU
Norwegian University of
Science and Technology